Optoelectronic excitations of hybrid inorganic organic systems including electron-phonon interaction

Dissertation

zur
Erlangung des Doktorgrades
doctor rerum naturalium (Dr. rer. nat.)

im Fach: Physik
Spezialisierung: Theoretische Festkörperphysik

eingereicht an der
Mathematisch-Naturwissenschaftlichen Fakultät
der Humboldt-Universität zu Berlin

vorgelegt von

Herrn Ignacio Alfonso Gonzalez Oliva
geb. am 29.05.1992 in El Salvador

Präsidentin der Humboldt-Universität zu Berlin
Prof. Dr. Julia von Blumenthal

Dekan der Mathematisch-Naturwissenschaftlichen Fakultät
Prof. Dr. Emil List-Kratochvil

GutachterInnen:	Prof. Dr. Dr. h.c. Claudia Draxl Prof. Dr. Peter Puschnig Dr. Mariana Rossi
Tag der mündlichen Prüfung:	DD MM YYYY

Ich erkläre, dass ich die Dissertation selbständig und nur unter Verwendung der von mir gemäß §7 Abs. 3 der Promotionsordnung der Mathematisch-Naturwissenschaftlichen Fakultät, veröffentlicht im Amtlichen Mitteilungsblatt der Humboldt-Universität zu Berlin Nr. 42/2018 am 11.07.2018 angegebenen Hilfsmittel angefertigt habe.

Weiterhin erkläre ich, dass ich mich nicht bereits anderwärts um einen Doktorgrad im Promotionsfach Physik beworben habe beziehungsweise einen entsprechenden Doktorgrad besitze.

Ich habe Kenntnis der dem Promotionsverfahren zugrunde liegenden Promotionsordnung der Mathematisch-Naturwissenschaftlichen Fakultät, veröffentlicht im Amtlichen Mitteilungsblatt der Humboldt-Universität zu Berlin Nr. 42/2018 am 11.07.2018.

Berlin, den DD. MMMM YYYY

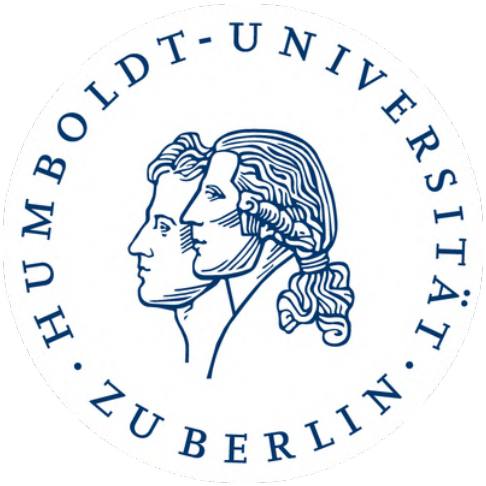

Mathematisch-Naturwissenschaftliche Fakultät
Institut für Physik

Optoelectronic excitations of hybrid inorganic organic systems including electron-phonon interaction

Doctoral Thesis

by Herrn Ignacio Alfonso Gonzalez Oliva

Supervisor: Prof. Dr. Dr. h.c. Claudia Draxl

Dedicated to Alexandra, Xenia, Griseida and Alfonso

Summary

Hybrid inorganic organic systems (HIOS), combining inorganic semiconductors and conjugated organic materials, have attracted significant attention in solid state physics and materials science. They represent an up-and-coming basis for future applications, such as lighting devices, field-effect transistors, solar cells, and photoswitches. The appeal of these hybrid materials stems from their capacity to combine the best of both worlds. Specifically, they exhibit strong light-matter interaction and the chemical tunability of organic materials, coupled with the high carrier mobilities and nearly free charge carriers in the inorganic materials.

The experimental characterization of HIOS has advanced significantly, however the accurate theoretical description of their electronic and optical properties remains challenging. This is largely due to the complex interplay among electronic correlations, electron-phonon coupling, and excitonic effects. To address these challenges, many-body perturbation theory (MBPT) provides the state-of-the-art framework. Techniques such as the G_0W_0 approximation allow for the computation of quasiparticle (QP) energies. Solving the Bethe-Salpeter equation (BSE) gives access to excitonic properties and absorption spectra. Despite the existence of many studies on electron-phonon interaction (EPI) from first principles, practical calculations including all these effects on equal footing have only recently become accessible for hybrid systems.

In this PhD project, we investigate many-body effects in three prototypical HIOS, *i.e.*, pyrene@MoS_2, pyridine@MoS_2 and PTCDA@WSe_2. Applying the G_0W_0 approximation, we compute the QP band structure and analyze the influence of dynamical screening on the energy-level alignment. The absorption spectra are calculated by solving the BSE, and the low-energy excitations are classified based on the analysis of the exciton wavefunctions and their projections onto the constituent materials. To incorporate electron-phonon coupling, we evaluate the Fan-Migdal (FM) self-energy, thus allowing us to assess the impact of EPI on the QP energies and thus the renormalization of band edges.

Beyond the accurate theoretical description of the optoelectronic properties, modeling hybrid interfaces represents a significant computational challenge due to their large unit cells. A particularly efficient approach for weakly bonded interfaces consists in an additive ansatz, where the polarizability of the heterostructure is obtained by summing the contributions of the individual components. In the final chapter of this thesis, we introduce the *expansion & addition screening* (EAS) method to efficiently calculate the polarizability of physisorbed systems in both G_0W_0 and BSE calculations. This approach is implemented in the **`exciting`** code, a full-potential all electron code based on the (linearized) augmented plane wave ((L)APW) method.

Zusammenfassung

Hybride anorganisch-organische Systeme, die anorganische Halbleiter und konjugierte organische Materialien kombinieren, haben in der Festkörperphysik und den Materialwissenschaften große Aufmerksamkeit erregt. Sie bilden eine aufstrebende Grundlage für künftige Anwendungen wie Beleuchtungsvorrichtungen, feldelektrische Transistoren, Solarzellen und Fotoschalter. Die Attraktivität dieser Hybridmaterialien beruht auf ihrer Fähigkeit, das Beste aus beiden Welten zu vereinen. Insbesondere weisen sie eine starke Licht-Materie-Wechselwirkung und die chemische Abstimmbarkeit organischer Materialien auf, gekoppelt mit der hohen Ladungsträgermobilität und den nahezu freien Ladungsträgern der anorganischen Materialien.

Die experimentelle Charakterisierung von HIOS ist weit fortgeschritten, doch die genaue theoretische Beschreibung ihrer elektronischen und optischen Eigenschaften bleibt eine Herausforderung. Dies ist weitgehend auf das komplexe Zusammenspiel von elektronischen Korrelationen, Elektron-Phonon-Kopplung und exzitonischen Effekten zurückzuführen. Um diese Herausforderungen zu bewältigen, bietet MBPT den modernsten Rahmen. Techniken wie die G_0W_0-Approximation ermöglichen die Berechnung von QP-Energien. Die Lösung der BSE gibt Zugang zu exzitonischen Eigenschaften und Absorptionsspektren. Trotz zahlreicher Studien über EPI aus ersten Prinzipien sind praktische Berechnungen, die alle diese Effekte gleichberechtigt berücksichtigen, erst seit kurzem für hybride Systeme zugänglich.

In diesem Dissertationsprojekt untersuchen wir Vielteilcheneffekte in drei prototypischen HIOS, *i.e.*, Pyrene@MoS_2, Pyridine@MoS_2 und PTCDA@WSe_2. Unter Anwendung der G_0W_0-Approximation berechnen wir die QP-Bandstruktur und analysieren den Einfluss der dynamischen Abschirmung auf die Ausrichtung der Energieniveaus. Die Absorptionsspektren werden durch Lösen der BSE berechnet, und die niederenergetischen Anregungen werden anhand der Analyse der Exzitonen-Wellenfunktionen und ihrer Projektionen auf die konstituierenden Materialien klassifiziert. Um die Elektron-Phonon-Kopplung einzubeziehen, bewerten wir die FM-Eigenenergie und können so die Auswirkungen von EPI auf die QP-Energien und somit die Renormierung der Bandkanten beurteilen.

Neben der genauen theoretischen Beschreibung der optoelektronischen Eigenschaften stellt die Modellierung von hybriden Grenzflächen aufgrund ihrer großen Einheitszellen eine große rechnerische Herausforderung dar. Ein besonders effizienter Ansatz für schwach gebundene Grenzflächen besteht in einem additiven Ansatz, bei dem die Polarisierbarkeit der Heterostruktur durch Summierung der Beiträge der einzelnen Komponenten ermittelt wird. Im letzten Kapitel dieser Arbeit wird die EAS-Methode zur effizienten Berechnung der Polarisierbarkeit von physisorbierten Systemen sowohl in G_0W_0- als auch in BSE-Rechnungen vorgestellt. Dieser Ansatz ist im **`exciting`** code implementiert.

Contents

List of Figures

List of Tables

List of acronyms and abbreviations

ARPES angle-resolved photoemission spectroscopy

BSE Bethe-Salpeter equation

CBM conduction band minimum

DFPT density-functional perturbation theory

DFT density-functional theory

DOS density of states

DW Debye-Waller

EAS *expansion & addition screening*

EPI electron-phonon interaction

FM Fan-Migdal

GGA generalized gradient approximation

GS ground-state

HIOS Hybrid inorganic organic systems

HOMO highest occupied molecular orbital

HSE Heyd, Scuseria, and Ernzerhof

IQPA independent quasi-particle approximation

KS Kohn-Sham

(L)APW (linearized) augmented plane wave

LDA local-density approximation

LUMO lowest unoccupied molecular orbital

MBPT many-body perturbation theory

PBE Perdew, Burke, and Ernzerhof

PTCDA perylenetetracarboxylic dianhydride

QP quasiparticle

RPA random-phase approximation

SOC spin-orbit coupling

TMDCs transition metal dychalcogenides

TS Tkatchenko-Scheffler

VBM valence band maximum

vdW van der Waals

ZPR zero-point renormalization

Introduction

Hybrid inorganic organic systems (HIOS) composed of organic molecules and two dimensional (2D) inorganic semiconductors are gaining significant attention due to their potential in advanced opto-electronic applications [1–9]. Indeed, HIOS exploit the complementary properties of their constituents to tune their electronic and optical properties [10–16]. A particularly promising class of HIOS is formed by the integration of 2D transition metal dychalcogenides (TMDCs) and conjugated organic molecules [17]. The adsorption of organic molecules on TMDCs surfaces, mediated by dipole and van der Waals (vdW) interactions, has been shown to induce interfacial effects and emergent phenomena that are absent in conventional bulk semiconductors [18–23]. Among 2D TMDCs, monolayers of MoS_2 and WSe_2 stand out due to their direct band gaps in the visible region, strong Coulomb interaction, and exceptional charge carrier mobilities [10, 24–36]. These characteristics render them ideal platforms for constructing hybrid materials with tunable many-body interactions and for advancing fundamental understanding and technological exploitation of interfacial phenomena [37–42].

In order to effectively explore the potential combinations of materials, a full understanding of their properties requires both experimental and theoretical investigations. For instance, experimental research has been conducted on the alignment of energy levels and the formation of interfacial excitons using photoemission spectroscopy and photoluminescence [39, 43, 44]. Theoretical approaches have also been instrumental in providing essential insight into charge transfer and optical excitations [45–49]. In particular, the accurate description of band structures and energy-level alignments as well as optical excitations, polaronic effects, and associated dynamical processes, becomes of utmost importance as it determines the suitability of a system for a given application [19, 47–55]. To fully understand hybrid materials and reach predictive power on a quantitative level, novel methodology on various levels is needed [45]. This requirement comes with two challenges [46]. First, the level of sophistication must be sufficient to adequately describe the relevant physics of such interfaces. Second, a computational challenge emerges from the extremely demanding nature of the calculations due to the large unit cells.

To address the first challenge, first-principles calculations based solely on density-

functional theory (density-functional theory (DFT)) [56, 57] is not sufficient, for example, in predicting the wrong energy-level alignment of HIOS, due to its insufficient treatment of electron correlation [37, 53, 54]. Furthermore, at least semi-local DFT does not capture electron-hole interactions, which are crucial for describing optical spectra. For these reasons, many-body perturbation theory (MBPT) in terms of the GW approximation [58] and the Bethe-Salpeter equation (BSE) [59–61] are the state-of-the-art to study the properties of hybrid interfaces [47, 50–54, 62–69]. Successful applications of MBPT include the prediction of level alignment in HIOS [53, 54] as well as the description of optical absorption spectra and excitonic features in good agreement with experimental data [44]. Importantly, the interaction between electrons and phonons has only recently been explored in hybrid systems[70, 71]. Understanding the impact of the electron-phonon interaction (EPI) is crucial for investigating the temperature dependence of band gaps, carrier mobilities, and spectral signatures[72, 73]. Recent methodological developments have paved the way for incorporating EPI by means of MBPT, thereby facilitating the transition from the theoretical framework to practical calculations [74–77].

Unfortunately, the computational demands of MBPT calculations for hybrid materials with large unit cells are substantial. One of the major bottlenecks in G_0W_0 and BSE calculations is the calculation of the polarizability, which scales as $O(N^4)$ with the number of electrons N [58, 78]. Moreover, the solution of the BSE requires $O(N^5)$ operations [79]. Therefore, recent efforts have actively explored methods to reduce the high computational cost. For example, an interpolative separable density fitting (ISDF) approach [80, 81] has been suggested for setting up the BSE hamiltonian together with using a Lanczos algorithm for its diagonalization. Another efficient approach consists of an additive ansatz of the polarizability, where the polarizability of the heterostructure is obtained by summing the contributions of the individual components [48, 49]. This allows the calculation of the polarizability for the supercell of each constituent by a folding (expansion) procedure from the respective unit cell. The combination of these two approaches, called *expansion & addition screening* (EAS) here, has been successfully applied to the calculation of the energy-level alignment at molecule-metal interfaces [48, 49]. However, EAS has only been applied within a planewave representation of the polarizability, and thus it is not directly applicable to other basis sets, in particular those used in all-electron codes [82–84].

In this thesis, we study three prototypical HIOS, namely, monolayers of pyrene and pyridine on MoS_2 as well as PTCDA@WSe_2. Pyrene molecules [85] have been used as coating to protect TMDCs from photooxidation and environmental aging [21]. Pyridine, a member of the azabenzenes [86], has been used as a docking group at the interfaces with ZnO [68, 69, 87] and between MoS_2 and Hofmann-type coordination polymers (HTCP)

[88]. Heterostructures containing perylenetetracarboxylic dianhydride (PTCDA), *e.g.*, PTCDA@MoS_2 and PTCDA@WSe_2, have shown to promote energy transfer [39, 43, 89] and luminescence enhancement [39, 90, 91]. These results have sparked significant interest and motivation to determine their electronic and optical properties, both theoretically and experimentally, to enhance our understanding and optimization of hybrid materials. In order to address the computational challenge, the EAS approach is extended, for both the polarizability in *GW* and BSE calculations, to the mixed-product basis based of the (linearized) augmented planewave ((L)APW) method.

This thesis is organized as follows: a theoretical background is provided in Chapter 1, in which we summarize the methodology used in this work to obtain, *i.e.*, electron and phonon band structures and eigenfunctions, self-energies, and exciton energies. Chapter 2 focuses on the structural, electronic, and optical properties of monolayer MoS_2 and WSe_2. It describes the geometry optimization applying different exchange-correlation functionals. Then, the electronic properties are studied focusing on the dimensionality and the inclusion of spin-orbit coupling (SOC). The role of many-body effects is explored by computing the QP band structure within the G_0W_0 approximation, the optical spectra by solving the BSE, and the spectral signatures due to EPI. In Chapter 3, we discuss the many-body effects in pyrene@MoS_2. The energy-level alignment is rationalized from the results of G_0W_0 calculations (Section 3.2). The optical properties are obtained by the solution of the BSE (Section 3.3). Finally, the temperature-dependent band structures are shown in Section 3.4. In Chapter 4, we use the same framework to investigate electron-electron (Section 4.2), electron-hole (Section 4.3), and electron-phonon (Section 4.4) interactions in pyridine@MoS_2. Chapter 5 shows the electronic (Section 5.2) and optical (Section 5.3) properties of PTCDA@WSe_2. Finally, in Chapter 6, we show the development and implementation of the EAS method for G_0W_0 and BSE. We describe the main equations for the expansion and addition steps in the mixed-product basis based of (L)APW, and we show results for selected materials, comparing the quasi-particle band structure and the dielectric function with results from G_0W_0 and BSE without using this approximation. Chapter 7 contains the conclusions and outlook of this work.

It doesn't matter how beautiful your theory is, it doesn't matter how smart you are. If it doesn't agree with experiment, it's wrong.

Richard P. Feynman

1 Theoretical background

The quantum-mechanical description of a condensed-matter system requires the solution of the Schrödinger equation, describing all nuclei, electrons, and their mutual interactions. The direct analytical or even numerical solution of this problem is far too complex, if not impossible. Therefore, appropriate approximations are needed [73]. In this chapter, we summarize the methodologies, which allow for a first-principle description of the electronic, vibrational, and optical properties of materials [57, 61, 92]. The last section of this chapter provides an overview of the **exciting** code [93], an all-electron full-potential package that has been used throughout this thesis.

1.1 The quantum-mechanical many-body problem

The full Hamiltonian, which describes a system composed by electrons and nuclei can be written as

$$\hat{H} = \hat{T}_{\mathrm{n}} + \hat{V}_{\mathrm{nn}} + \hat{H}_{\mathrm{e}} \,. \tag{1.1}$$

The first two terms correspond to the kinetic energy and Coulomb interaction of the nuclei, respectively. The third term is the so-called electronic Hamiltonian, given as

$$\hat{H}_{\mathrm{e}} = \hat{T}_{\mathrm{e}} + \hat{V}_{\mathrm{ee}} + \hat{V}_{\mathrm{en}} \,, \tag{1.2}$$

where the first term is the kinetic-energy operator of the electrons, and the next terms correspond to the Coulomb interactions between electrons as well as electrons and nuclei, respectively. The term $\hat{V}_{\text{en}}$, which couples electrons and nuclei, inhibits in principle a simplification of the full wavefunction in a factorized form [57, 75, 94]. However, since the nuclei are much heavier than the electrons, their motion is much slower, meaning that the electrons can respond to the nuclei's motion almost instantaneously. This leads to the Born-Oppenheimer (BO) approximation [95], where the full wavefunction of the system can indeed be factorized in a product of a "nuclear" and an "electronic" part. Thus, one can solve the Schrödinger equation for the electronic Hamiltonian at a fixed nuclear configuration. Nevertheless, an explicit solution of this simplified problem is still not trivial due to enormous number of electrons in a condensed-matter system. A simplification can be done by using the ground-state electronic density $\rho_{\text{GS}}(\mathbf{r})$, which depends on only 3 variables, as the main quantity instead of the many-electron wavefunction, as will be shown in the next section.

1.2 Density-functional theory

In density-functional theory (DFT), the ground-state (GS) electron density $\rho_{\text{GS}}(\mathbf{r})$, is used as the central object instead of the many-electron wavefunction. The mathematical foundation of DFT is given by the Hohenberg-Kohn (HK) theorems [96]. The first HK theorem states that the GS expectation value of any physical observable in a system of N electrons is a unique functional of $\rho_{\text{GS}}(\mathbf{r})$. This is due to the fact that the "external" potential of the electron system, which for a solid can be written as

$$\hat{V}_{\text{en}} = \sum_{i=1}^{N} v_{\text{ext}}(\mathbf{r}_i) \,, \tag{1.3}$$

is uniquely associated to the ground-state electron density, $\rho_{\text{GS}}(\mathbf{r})$, or in other words, there is a one-to-one correspondence between the single-particle external potential $v_{\text{ext}}(\mathbf{r})$ and $\rho_{\text{GS}}(\mathbf{r})$. The second theorem states that the GS energy functional $E_{\text{GS}}[\rho]$ is minimized if (and only if) the input density is the true GS density, thus

$$E_{\text{GS}}[\rho_{\text{GS}}] \leq E_{\text{GS}}[\rho] \,. \tag{1.4}$$

Using Eq. (1.4), the GS electron density can be determined by constrained minimization of the functional $E_{\mathrm{GS}}[\rho]$. This ends up in the equation

$$\left.\frac{\delta E_{\mathrm{GS}}[\rho]}{\delta \rho(\mathbf{r})}\right|_{\rho=\rho_{\mathrm{GS}}} = \mu \,, \tag{1.5}$$

with μ as the chemical potential of the electronic system.

1.2.1 Kohn-Sham (KS) approach

The solution of Eq. (1.5) can be obtained by introducing an auxiliary system of fictitious non-interacting electrons [56]. A possible way to express the GS energy functional is then

$$E_{\mathrm{GS}}[\rho] = T_0[\rho] + E_{\mathrm{H}}[\rho] + \int \mathrm{d}\mathbf{r}\, v_{\mathrm{ext}}(\mathbf{r})\, \rho(\mathbf{r}) + E_{\mathrm{xc}}[\rho] \,, \tag{1.6}$$

where $T_0[\rho]$ is the kinetic-energy functional of the system of non-interacting electrons, $E_{\mathrm{H}}[\rho]$ the classical Hartree energy, and $E_{\mathrm{xc}}[\rho]$ the exchange-correlation energy functional, which contains energy contributions from the kinetic-energy difference between the interacting and the non-interacting system, as well as the electron-electron interactions that are not represented by the Hartree energy. The Kohn-Sham (KS) approach is built upon assuming that the GS density of the interacting system is equal to that of the non-interacting system

$$\rho_{\mathrm{GS}}(\mathbf{r}) = \sum_{i}^{N} |\phi_i(\mathbf{r})|^2 \,, \tag{1.7}$$

where the single-particle KS orbitals, $\phi_i(\mathbf{r})$, are obtained by solving the single-particle Schrödinger equations for the fictitious system

$$\hat{h}_{\mathrm{KS}}\, \phi_i(\mathbf{r}) = \varepsilon_i\, \phi_i(\mathbf{r}) \,. \tag{1.8}$$

Here, ε_i are the corresponding energies to ϕ_i and the KS hamiltonian is defined as[1]

$$\hat{h}_{\mathrm{KS}} = -\frac{1}{2}\nabla^2 + v_{\mathrm{KS}}(\mathbf{r}, [\rho]) \,, \tag{1.9}$$

[1]Through out this thesis we use atomic units with $\hbar = m_e = e^2 = (4\pi\epsilon_0)^{-1} = 1$

with the KS potential

$$v_{\mathrm{KS}}(\mathbf{r},[\rho]) = v_{\mathrm{ext}}(\mathbf{r},[\rho]) + v_{\mathrm{H}}(\mathbf{r},[\rho]) + v_{\mathrm{xc}}(\mathbf{r},[\rho])\,, \tag{1.10}$$

where the first term represents the external potential, the second term the Hartree interaction among the electrons, and the third term the exchange-correlation potential, $v_{\mathrm{xc}}(\mathbf{r},[\rho]) \equiv \delta E_{\mathrm{xc}}[\rho]/\delta\rho(\mathbf{r})$. Equations (1.8) to (1.10) are called KS equations and are solved self-consistently. The self-consistent cycle stops once a chosen convergence criterion is fulfilled, then the converged density is used to calculate the GS properties. The KS approach gives the exact GS energy and electronic density if the exact $v_{\mathrm{xc}}(\mathbf{r},[\rho])$ is known. However, its exact form is not known, and we need to make use of approximations. The next section focuses on the approximations for $E_{\mathrm{xc}}[\rho]$ used in this thesis.

1.2.2 Exchange-correlation functionals

Despite the small contribution of $E_{\mathrm{xc}}[\rho]$ to the total energy in comparison with the other terms, the quality of the GS properties is largely determined by its precise evaluation. There are several approximations for $E_{\mathrm{xc}}[\rho]$ [97, 98] as sketched in Fig. 1.1. We mainly use the exchange-correlation functional parametrization proposed by Perdew, Burke, and Ernzerhof (PBE) [99]. This parametrization is part of the generalized gradient approximation (GGA) family of functionals, which corresponds to the second rung on Jacob's ladder (see Fig. 1.1). The GGA exchange-correlation energy is given by

$$E_{\mathrm{xc}}^{\mathrm{GGA}}[\rho] \equiv \int \mathrm{d}\mathbf{r}\, \rho(\mathbf{r})\, \epsilon_{\mathrm{x}}^{\mathrm{unif}}(\rho) F_{\mathrm{xc}}(r_s,\xi,s)\,, \tag{1.11}$$

where $\epsilon_{\mathrm{x}}^{\mathrm{unif}}(\rho) = -3k_{\mathrm{F}}/4\pi$ is the Slater exchange energy of an uniform gas, $k_{\mathrm{F}} = (3\pi^2\rho)^{1/3}$ is the Fermi-wave vector, and $F_{\mathrm{xc}}(r_s,\xi,s)$ is the so-called exchange-correlation enhancement factor which depends on the dimensionless density gradient, $s = |\nabla\rho|/2k_{\mathrm{F}}\rho$. The variable ξ refers to the spin polarization, which is zero for non-magnetic systems.

There are limitations for GGA when non-local correlations are important, in these cases, higher-level exchange-correlation functional are needed. Hybrid functionals that include a certain amount of Hartree-Fock (HF) exchange have improved over the limitations of semilocal approximations [100, 101]. Heyd, Scuseria, and Ernzerhof (HSE) presented a screened hybrid functional [102, 103], in which only the short-range part of the HF exchange is considered,

$$E_{\mathrm{xc}}^{\mathrm{HSE}} = E_{\mathrm{xc}}^{\mathrm{PBE}} + \alpha\left[E_{\mathrm{x}}^{\mathrm{HF}}(\omega) - E_{\mathrm{x}}^{\mathrm{PBE}}(\omega)\right]\,, \tag{1.12}$$

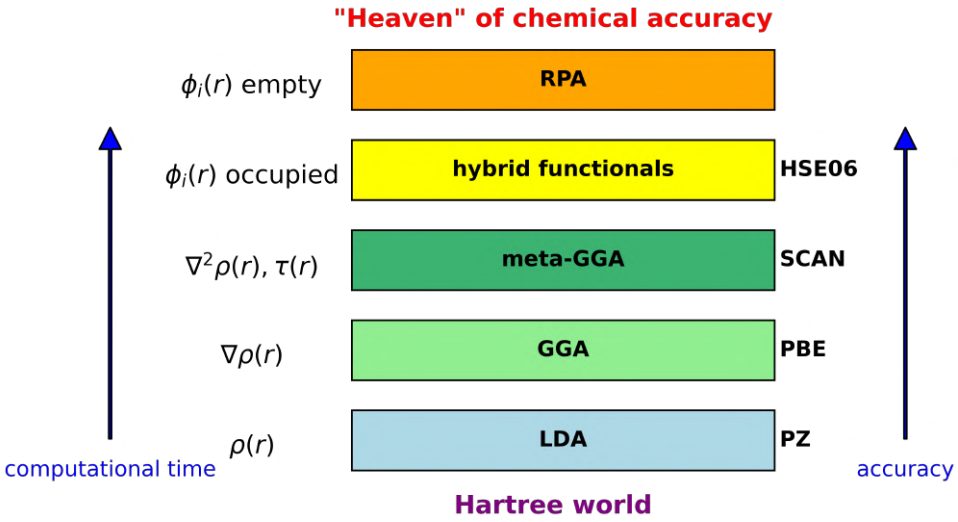

Figure 1.1: The diagram depicts the hierarchical improvement in approximations for the exchange-correlation functional, with increasing accuracy and computational cost as one ascends the ladder. Starting from the local-density approximation (LDA), and culminating in the random-phase approximation (RPA) for correlations. At the top lies the "heaven of chemical accuracy", signifying the idealized goal of achieving chemical accuracy, with errors in the energy calculated below 1 kcal/mol.

where $\omega = 0.11\ a_0^{-1}$, and $\alpha = 0.25$. We calculate the electronic properties of our prototypical HIOS, pyrene@MoS_2, using HSE to evaluate the impact of non-local correlations. However, using solely HSE turns out to be insufficient to accurately describe the electronic properties of such systems as discussed in Chapter 3. In this case, going beyond DFT, the Green's function approach denoted G_0W_0 [61, 104] is the method of choice, and will be described in the following section.

1.3 Many-body perturbation theory

DFT, as described in the previous section, provides an efficient framework for obtaining the GS energy and related properties of the system. However, the description of excited-states is a challenge for DFT-based approaches [60, 61, 94]. To overcome this situation, many-body perturbation theory (MBPT) provides a powerful way to compute excited states and can be expressed at the different levels by using Green's functions [58, 78].

1.3.1 One- and two-particle Green's function

The single-particle Green's function at zero temperature is defined as

$$G(1,2) = -\mathrm{i}\langle 0|\,\hat{T}\Big[\hat{\psi}(1)\,\hat{\psi}^{\dagger}(2)\Big]|0\rangle\,, \tag{1.13}$$

where $\hat{T}$ is the time-ordering operator and $\hat{\psi}$ is a fermionic field operator. In Eq. (1.13), we have used the notation $(1,2)$, a compact notation of positional and temporal variables, *i.e.*, $(\mathbf{r}_1, t_1, \mathbf{r}_2, t_2)$. The expectation value in the definition is taken with respect to the many-body groundstate $|0\rangle$. The single-particle Green's function gives access to the expectation values of single-particle operators, GS total energies and excitation spectra.

The time-ordered two-particle Green's function $G_2(1,2;1',2')$ is defined as

$$G_2(1,2;1',2') = (-\mathrm{i})^2\langle 0|\,\hat{T}\Big[\hat{\psi}(1)\,\hat{\psi}(2)\,\hat{\psi}^{\dagger}(2')\,\hat{\psi}^{\dagger}(1')\Big]|0\rangle\,, \tag{1.14}$$

and describes the correlated propagation of two particles. More generally, the N-particle Green's function is defined analogous

$$G_N(1,\cdots,N;1',\cdots,N') = (-\mathrm{i})^N\langle 0|\,\hat{T}\Big[\hat{\psi}(1)\,\cdots\hat{\psi}(N)\,\hat{\psi}^{\dagger}(N')\cdots\hat{\psi}^{\dagger}(1')\Big]|0\rangle\,. \tag{1.15}$$

Using the definitions of the one- and two-particle Green's functions given in Eqs. (1.13) and (1.14), we can link the two of them through the so-called Bogoliubov-Born-Green-Kirkwood-Yvon (BBGKY) hierarchy of integro-differential equations [59]

$$\left[\mathrm{i}\frac{\partial}{\partial t_1} - h_0(1)\right] G(1,2) + \mathrm{i}\int \mathrm{d}3\, v(1,3)\, G_2(1,3^{+};2,3^{++}) = \delta(1,2)\,, \tag{1.16}$$

with $h_0(1) \equiv h_0(\mathbf{r}_1)\,\delta(t_1)$ as the single-particle term of the electronic Hamiltonian, $v(1,2) \equiv v(\mathbf{r}_1,\mathbf{r}_2)\,\delta(t_1-t_2) = \delta(t_1-t_2)/|\mathbf{r}_1-\mathbf{r}_2|$ the repulsive Coulomb interaction between electrons, and the notation $1^{+} \equiv \{\mathbf{r}_1, t_1+\eta\}$, where η is a positive infinitesimal. Equation (1.16) is not directly helpful for a practical calculation since it expresses the Green's function in terms of a more complex object, G_2. However, it can be simplified and rewritten by introducing an auxiliary quantity, the self-energy. The self-energy Σ is formally defined by the following identity

$$\int \mathrm{d}3\big[v_{\mathrm{H}}(3)\,\delta(3,1) + \Sigma(1,3)\big]\, G(3,2) = -\mathrm{i}\int \mathrm{d}3\, v(1,3)\, G_2(1,3^{+};2,3^{++})\,, \tag{1.17}$$

where $v_{\mathrm{H}}(1) \equiv v_{\mathrm{H}}(\mathbf{r}_1)\,\delta(t_1)$ is the Hartree potential from Eq. (1.10). The replacement of

Eq. (1.17) into Eq. (1.16) yields the Dyson equation in differential form, which is also referred as equation of motion of the interacting Green's function

$$\left[\mathrm{i}\frac{\partial}{\partial t_1} - h_0(1) - v_{\mathrm{H}}(1)\right] G(1,2) - \int \mathrm{d}3\, \Sigma(3,1)\, G(3,2) = \delta(1,2)\,. \tag{1.18}$$

The self-energy is in general a complex, non-local, and non-Hermitian operator. The real part of the self-energy can be related to the exchange and correlation contributions to the quasiparticle energies, whereas the imaginary part contains information about the excitation lifetime. For practical calculations, the objective is to compute the Green's function, $G(1,2)$ and the self-energy, Σ in a self-consistent approach. In Appendix D, Hedin's equations are presented and the GW approximation is introduced. Therefore, we directly continue with the G_0W_0 approximation in the next section.

1.3.2 The G_0W_0 approximation

In this section, we briefly summarize the G_0W_0 approximation, as sketched in the right panel of Fig. D.1 in Appendix D. The proposed strategy is to start by setting $\Sigma = 0$, and computing the noninteracting single-particle Green function G_0. Different initial guesses for G_0 can be considered, such as, KS or Hartree-Fock Green's functions. Here, we obtain G_0 from the KS states

$$G_0(\mathbf{r},\mathbf{r}';\omega) = \sum_{n\mathbf{k}} \frac{\phi_{n\mathbf{k}}(\mathbf{r})\, \phi^*_{n\mathbf{k}}(\mathbf{r}')}{\omega - \tilde{\varepsilon}_{n\mathbf{k}}}\,, \tag{1.19}$$

where $\tilde{\varepsilon}_{n\mathbf{k}} \equiv \varepsilon_{n\mathbf{k}} + \mathrm{i}\,\eta\,\mathrm{sgn}(\varepsilon_{\mathrm{F}} - \varepsilon_{n\mathbf{k}})$ with ε_{F} as the Fermi energy. The polarizability P_0 is then computed as

$$P_0(\mathbf{r},\mathbf{r}';\omega) = \sum_{nm}\sum_{\mathbf{k},\mathbf{q}} F_{nm}(\mathbf{k},\mathbf{q};\omega)\, \phi_{n\mathbf{k}}(\mathbf{r})\, \phi^*_{m\mathbf{k}-\mathbf{q}}(\mathbf{r})\, \phi^*_{n\mathbf{k}}(\mathbf{r}')\, \phi_{m\mathbf{k}-\mathbf{q}}(\mathbf{r}')\,, \tag{1.20}$$

where $\mathbf{q} = \mathbf{k} - \mathbf{k}'$, and the factor $F_{nm}(\mathbf{k},\mathbf{q};\omega)$ is

$$F_{nm}(\mathbf{k},\mathbf{q};\omega) \equiv 2 f_{n\mathbf{k}}(1 - f_{m\mathbf{k}-\mathbf{q}}) \left\{ \frac{1}{\omega - \varepsilon_{m\mathbf{k}-\mathbf{q}} + \varepsilon_{n\mathbf{k}} + \mathrm{i}\eta} - \frac{1}{\omega + \varepsilon_{m\mathbf{k}-\mathbf{q}} - \varepsilon_{n\mathbf{k}} - \mathrm{i}\eta} \right\}\,,$$

with $f_{n\mathbf{k}}$ being the occupation number of state $n\mathbf{k}$, and η an infinitesimal positive number. The polarizability of Eq. (1.20) correspond to the irreducible polarizability evaluated in the random-phase approximation (RPA). The next step is to compute the dynamically

screened Coulomb potential W_0, which is given by

$$W_0(\mathbf{r},\mathbf{r}';\omega) = \int \mathrm{d}\mathbf{r}_1\, \epsilon^{-1}(\mathbf{r},\mathbf{r}_1;\omega)\, v(\mathbf{r}_1,\mathbf{r}')\,, \tag{1.21}$$

where $v(\mathbf{r}_1,\mathbf{r}')$ is the bare Coulomb potential and $\epsilon(\mathbf{r},\mathbf{r}';\omega)$ is the dielectric function calculated as

$$\epsilon(\mathbf{r},\mathbf{r}';\omega) = \delta(\mathbf{r},\mathbf{r}') - \int \mathrm{d}\mathbf{r}_1\, v(\mathbf{r},\mathbf{r}_1)\, P_0(\mathbf{r}_1,\mathbf{r}';\omega)\,. \tag{1.22}$$

The final step is to introduce W_0 and G_0 in the expression of the self-energy, Eq. (D.1). Once Σ has been calculated, we can solve the QP Schrödinger-like equation

$$\left[-\frac{1}{2}\nabla^2 + v_{\mathrm{ext}}(\mathbf{r}) + v_{\mathrm{H}}(\mathbf{r})\right]\psi_{n\mathbf{k}}(\mathbf{r}) + \int \mathrm{d}\mathbf{r}'\, \Sigma(\mathbf{r},\mathbf{r}',\varepsilon^{\mathrm{QP}}_{n\mathbf{k}})\, \psi_{n\mathbf{k}}(\mathbf{r}) = \varepsilon^{\mathrm{QP}}_{n\mathbf{k}}\, \psi_{n\mathbf{k}}(\mathbf{r})\,, \tag{1.23}$$

where $\psi_{n\mathbf{k}}$ is the QP wavefunction and $\varepsilon^{\mathrm{QP}}$ is the energy of an electron in band n, carrying crystal momentum $\mathbf{k}$. The QP energies in the G_0W_0 approximation are given by

$$\varepsilon^{\mathrm{QP}}_{n\mathbf{k}} = \varepsilon_{n\mathbf{k}} + Z_{n\mathbf{k}}\left[\mathrm{Re}\Sigma_{n\mathbf{k}}(\varepsilon_{n\mathbf{k}}) - V^{\mathrm{xc}}_{n\mathbf{k}}\right]\,, \tag{1.24}$$

where $V^{\mathrm{xc}}_{n\mathbf{k}}$ are the diagonal matrix elements of the exchange-correlation potential, and $Z_{n\mathbf{k}}$ is the so-called QP renormalization factor

$$Z_{n\mathbf{k}} = \left\{1 - \left[\frac{\partial}{\partial\omega}\,\mathrm{Re}\Big(\Sigma_{n\mathbf{k}}(\omega)\Big)\right]_{\varepsilon_{n\mathbf{k}}}\right\}^{-1}\,. \tag{1.25}$$

We conclude this section by highlighting that the polarizability P_0, Eq. (1.20), is the main quantity in the expansion addition screening (eas) method presented in Chapter 6.

1.3.3 Effective BSE-Hamiltonian

We introduce in this section the Bethe-Salpeter equation (BSE) as an eigenvalue equation by defining the electron-hole Hamiltonian H^{eh} as

$$H^{\mathrm{eh}}_{(j_1j_2)(j_3j_4)} = \Big(\varepsilon^{\mathrm{QP}}_{j_2} - \varepsilon^{\mathrm{QP}}_{j_1}\Big)\,\delta_{j_1j_3}\delta_{j_2j_4} - \mathrm{i}\,(f_{j_2} - f_{j_1})\,\Xi_{(j_1j_2)(j_3j_4)}\,, \tag{1.26}$$

where $\Xi_{(j_1j_2)(j_3j_4)}$ are the matrix elements of the Bethe-Salpeter interaction kernel from Eq. (D.11). For semiconductors and insulators, all transitions occur from fully occupied

valence states v to unoccuppied conduction states c, thus the occupation factors (given by the Fermi-Dirac distribution) are $f_v = 1$ and $f_c = 0$. We make use of the Tamm-Dancoff approximation [105], which allows us to neglect the coupling between resonant and anti-resonant transitions, *i.e.*, between excitations and de-excitations. The Tamm-Dancoff approximation is valid if the band gap is larger than the average electron-hole interaction, which in practical terms, makes the approximation very useful for molecules but limited for metals and semiconductors. Applying this, the eigenvalue equation takes the form

$$\sum_{v'c'\mathbf{k}'} H^{\mathrm{eh}}_{vc\mathbf{k},v'c'\mathbf{k}'} \, A^{\lambda}_{v'c'\mathbf{k}'} = E^{\lambda} A^{\lambda}_{vc\mathbf{k}} \,, \tag{1.27}$$

where E^{λ} is the energy eigenvalue belonging to the eigenvector $A^{\lambda}_{vc\mathbf{k}}$ of the excitation labeled λ. The Hamiltonian has three contributions,

$$\hat{H}^{\mathrm{eh}} = \hat{H}^{\mathrm{diag}} + \hat{H}^{\mathrm{dir}} + \hat{H}^{\mathrm{x}} \,. \tag{1.28}$$

The first term $\hat{H}^{\mathrm{diag}}$ stands for the independent quasiparticle transitions and is therefore diagonal. The direct term $\hat{H}^{\mathrm{dir}}$ accounts for the attractive interaction between electron and hole, while the exchange term $\hat{H}^{\mathrm{x}}$ is responsible for the repulsive exchange interaction between the electron and the hole. The corresponding excitonic wave function Φ^{λ} is given as an expansion into products of single-particle wave functions with the eigenvectors A^{λ} as expansion coefficients according to

$$\Phi^{\lambda}(\mathbf{r}_{\mathrm{e}}, \mathbf{r}_{\mathrm{h}}) = \sum_{vc\mathbf{k}} A^{\lambda}_{vc\mathbf{k}} \, \phi^{*}_{v\mathbf{k}}(\mathbf{r}_{\mathrm{h}}) \, \phi_{c\mathbf{k}}(\mathbf{r}_{\mathrm{e}}) \,. \tag{1.29}$$

In the latter, $\mathbf{r}_h$ and $\mathbf{r}_e$ are the coordinates of the hole and the electron, respectively. The transition coefficient t^{λ} of a given excitation λ is introduced, as a sum over the matrix elements of the momentum operator $\hat{\mathbf{p}}$ weighted by the BSE eigenvectors,

$$t^{\lambda} = \sum_{vc\mathbf{k}} A^{\lambda}_{vc\mathbf{k}} \frac{\langle v\mathbf{k}|\hat{\mathbf{p}}|c\mathbf{k}\rangle}{\varepsilon_{c\mathbf{k}} - \varepsilon_{v\mathbf{k}}} \,, \tag{1.30}$$

with $\varepsilon_{c\mathbf{k}}$ and $\varepsilon_{v\mathbf{k}}$ the single-particle energies of the conduction and valence states, respectively. The imaginary part of the macroscopic dielectric tensor can now be formulated as

$$\mathrm{Im}\big[\epsilon_M(\omega)\big] = \frac{8\pi^2}{V} \sum_{\lambda} \big[t^{\lambda}\big]^2 \, \delta(\omega - E^{\lambda}) \,. \tag{1.31}$$

1.4 Phonons and electron-phonon interaction

In the previous section, we have described a practical framework for the renormalization of the electronic eigenvalues due to electron-electron interaction. In this section, we summarize the most important ingredients to compute the self-energy due to electron-phonon interaction (EPI). We begin by presenting the central quantities in the calculation of phonons in the harmonic approximation. The squares of the phonon frequencies $\omega_\nu(\mathbf{q})$ of a mode ν and the corresponding eigendisplacements $\mathbf{e}_{\alpha\kappa\nu}(\mathbf{q})$ are obtained by diagonalizing the dynamical matrix according to

$$\sum_{\alpha'\kappa'} \tilde{D}^{\alpha'\kappa'}_{\alpha\kappa}(\mathbf{q})\, \mathbf{e}_{\alpha\kappa\nu}(\mathbf{q}) = \omega^2_\nu(\mathbf{q})\, \mathbf{e}_{\alpha\kappa\nu}(\mathbf{q})\,. \tag{1.32}$$

where the dynamical matrix $\tilde{D}$ is the Fourier transform of the interatomic force constants (IFCs), C

$$\tilde{D}^{\alpha'\kappa'}_{\alpha\kappa}(\mathbf{q}) = \frac{1}{\sqrt{M_\alpha M_{\alpha'}}} \sum_\ell C^{\alpha'\kappa'\ell}_{\alpha\kappa 0}\, \mathrm{e}^{\mathrm{i}\mathbf{q}\cdot\mathbf{R}_\ell}\,, \tag{1.33}$$

with M_α the mass of the nucleus α. The matrix of the interatomic force constants (IFCs) is defined as the second derivative of the total energy E with respect to the atomic displacements,

$$C^{\alpha'\kappa'\ell'}_{\alpha\kappa\ell} = \left.\frac{\partial^2 E}{\partial\tau_{\alpha\kappa\ell}\partial\tau_{\alpha'\kappa'\ell'}}\right|_0\,, \tag{1.34}$$

where $|_0$ means that the derivative is taken at the equilibrium configuration with vanishing forces. The displacement of atom α from its equilibrium position in direction κ in the cell ℓ with vector $\mathbf{R}_\ell$ is denoted by $\tau_{\alpha\kappa\ell}$.

1.4.1 Effective electron-phonon Hamiltonian

In the formalism of second quantization, physical observables are expressed in terms of field operators acting on Fock space, that is, in terms of creation and annihilation operators of both fermions and bosons. The Hamiltonian that describes the coupled

system of electrons and phonons is written in second quantization as

$$\hat{H}^{\text{eph}} = \sum_{n\mathbf{k}} \varepsilon_{n\mathbf{k}}\, \hat{c}^{\dagger}_{n\mathbf{k}}\, \hat{c}_{n\mathbf{k}} + \sum_{\mathbf{q}\nu} \omega_{\nu}(\mathbf{q}) \left(\hat{a}^{\dagger}_{\mathbf{q}\nu}\, \hat{a}_{\mathbf{q}\nu} + \frac{1}{2} \right) \\ + \frac{1}{\sqrt{N_p}} \sum_{\mathbf{k},\mathbf{q}} \sum_{mn\nu} g_{mn\nu}(\mathbf{k},\mathbf{q})\, \hat{c}^{\dagger}_{m\mathbf{k}+\mathbf{q}}\, \hat{c}_{n\mathbf{k}} \left(\hat{a}_{\mathbf{q}\nu} + \hat{a}^{\dagger}_{-\mathbf{q}\nu} \right) , \tag{1.35}$$

where $\hat{c}^{\dagger}_{n\mathbf{k}}$ and $\hat{c}_{n\mathbf{k}}$ are the fermionic creation and annihilation operators, respectively, $\hat{a}^{\dagger}_{\mathbf{q}\nu}$ and $\hat{a}_{\mathbf{q}\nu}$ denote the corresponding creation and annihilation operators for a bosonic field, and N_p is the number of unit cells in the Born-von-Kármán supercell. In Eq. (1.35), the first line corresponds to the separate electron and phonon subsystems, while the second line accounts for the coupling between electrons and phonons to the first-order in the atomic displacements. The electron-phonon matrix elements, $g_{mn\nu}(\mathbf{k},\mathbf{q})$, specify the coupling strength and will be defined in the following section.

1.4.2 Electron-phonon matrix elements

The electron-phonon coupling is obtained by expanding the KS effective potential in terms of the nuclear displacements [74, 106]. We recover the indeces used in the previous section and define the equilibrium position as $\boldsymbol{\tau}^{0}_{\alpha\ell} = \mathbf{R}_{\ell} + \boldsymbol{\tau}_{\alpha}$, while the displaced position is $\boldsymbol{\tau}_{\alpha\ell} = \boldsymbol{\tau}^{0}_{\alpha\ell} + \Delta\boldsymbol{\tau}_{\alpha\ell}$. Thus, the expansion of the potential is

$$v^{\text{KS}}\big(\{\boldsymbol{\tau}_{\alpha\ell}\} \big) = v^{\text{KS}}\big(\{\boldsymbol{\tau}^{0}_{\alpha\ell}\} \big) + \sum_{\alpha\kappa\ell} \frac{\partial v^{\text{KS}}}{\partial \tau_{\alpha\kappa\ell}}\, \Delta\tau_{\alpha\kappa\ell} \, . \tag{1.36}$$

The KS potential response to a phonon mode $(\mathbf{q},\nu)$ can be written in normal mode coordinates, using the phonon eigenvectors, $\mathbf{e}_{\alpha\kappa\nu}(\mathbf{q})$, and phonon eigenvalues, $\omega_{\nu}(\mathbf{q})$

$$\Delta_{\mathbf{q}\nu} v^{\text{KS}} = \sum_{\alpha\kappa} \left(\frac{1}{2M_{\alpha}\, \omega_{\nu}(\mathbf{q})} \right)^{1/2} \mathbf{e}_{\alpha\kappa\nu}(\mathbf{q}) \sum_{\ell} \mathrm{e}^{-\mathrm{i}\mathbf{q}\cdot(\mathbf{r}-\mathbf{R}_{\ell})}\, \frac{\partial v^{\text{KS}}}{\partial \tau_{\alpha\kappa 0}}\bigg|_{\mathbf{r}-\mathbf{R}_{\ell}} . \tag{1.37}$$

The electron-phonon matrix elements are the probability amplitudes for the scattering of an electron in state $\phi_{n\mathbf{k}}$ into the state $\phi_{m\mathbf{k}+\mathbf{q}}$ due to a perturbation of the KS potential caused by a phonon in the mode ν and crystal momentum $\mathbf{q}$ [77],

$$g_{mn\nu}(\mathbf{k},\mathbf{q}) = \langle \phi_{m\mathbf{k}+\mathbf{q}} | \Delta_{\mathbf{q}\nu} v^{\text{KS}} | \phi_{n\mathbf{k}} \rangle \, . \tag{1.38}$$

The coefficients $g_{mn\nu}(\mathbf{k},\mathbf{q})$ are obtained by evaluating Eq. (1.38) numerically [74]. In the case of polar materials, where atoms could carry non-zero Born effective charges, the analytical and non-analytical parts of the dynamical matrix are separated [107], and Eq. (1.38) is rewritten as the sum of short- and long-range contributions,

$$g_{mn\nu}(\mathbf{k},\mathbf{q}) = g^{\mathcal{S}}_{mn\nu}(\mathbf{k},\mathbf{q}) + g^{\mathcal{L}}_{mn\nu}(\mathbf{k},\mathbf{q}) \,, \tag{1.39}$$

where $g^{\mathcal{L}}_{mn\nu}(\mathbf{k},\mathbf{q})$ is expressed as

$$\begin{aligned} g^{\mathcal{L}}_{mn\nu}(\mathbf{k},\mathbf{q}) = \, & \mathrm{i}\frac{4\pi}{\Omega}\sum_{\alpha}\left(\frac{1}{2N_p\, M_\alpha\, \omega_\nu(\mathbf{q})}\right)^{1/2} \\ & \times \sum_{\mathbf{G}\neq\mathbf{q}} \frac{(\mathbf{q}+\mathbf{G})\cdot\mathbf{Z}^*_\alpha\cdot\mathbf{e}_{\alpha\kappa\nu}(\mathbf{q})}{(\mathbf{q}+\mathbf{G})\cdot\boldsymbol{\epsilon}_\infty\cdot(\mathbf{q}+\mathbf{G})} \times \langle\phi_{m\mathbf{k}+\mathbf{q}}|\mathrm{e}^{\mathrm{i}(\mathbf{G}+\mathbf{q})\cdot\mathbf{r}}|\phi_{n\mathbf{k}}\rangle \,, \end{aligned} \tag{1.40}$$

with $\mathbf{Z}^*_\alpha$ being the Born effective charges and $\boldsymbol{\epsilon}_\infty$ is the static macroscopic dielectric tensor, in the limit when only screening effects of the electrons are considered.

1.4.3 Electron-phonon self-energy

The self-energy Σ presented in Eq. (D.1) can take the form of an additive quantity as more and more interactions are considered, for example, by combining the electron-electron and electron-phonon interactions,

$$\Sigma(1,2) = \Sigma^{\mathrm{ee}}(1,2) + \Sigma^{\mathrm{eph}}(1,2) \,. \tag{1.41}$$

The electron-phonon term, Σ^{eph}, is broken down in three parts, the Fan-Migdal (FM) self-energy, Σ^{FM}, the Debye-Waller (DW) contribution Σ^{DW}, and a correction term Σ^{dGW} [77],

$$\Sigma^{\mathrm{eph}} = \Sigma^{\mathrm{FM}} + \Sigma^{\mathrm{DW}} + \Sigma^{\mathrm{dGW}} \,. \tag{1.42}$$

Σ^{FM} is a correction to the electronic excitation energies and describes the effect of the dynamic polarization of the lattice. Only this term depends on the screened Coulomb interaction. For this reason, it is the only contribution considered in this thesis. Applying the GW approximation, it is written as

$$\begin{aligned} \Sigma^{\mathrm{FM}}(1,2) &= \mathrm{i}\int \mathrm{d}(34)\, G(1,3)\, W^{\mathrm{ph}}(4,1^+)\, \Gamma(3,2,4) \\ \Sigma^{\mathrm{FM}}(1,2) &= \mathrm{i}\, G(1,2)\, W^{\mathrm{ph}}(1^+,2) \,. \end{aligned} \tag{1.43}$$

The calculation of Σ^{FM} is made feasible by considering the following approximations: First, the vertex Γ is set to a delta function, as in Eq. (D.6). Second, the electron Green's function is replaced by the KS Green's function evaluated at fixed positions of the nuclei. Additionally, we use an adiabatic propagator, meaning that we are in the regime of non-interacting phonons. Finally, we neglect the frequency dependence of the electron-phonon matrix elements. Using these approximations, Eq. (1.43) becomes

$$\Sigma^{\mathrm{FM}}_{n\mathbf{k}}(\omega) = \sum_{m\nu} \int_{\mathrm{BZ}} \frac{\mathrm{d}\mathbf{q}}{\Omega_{\mathrm{BZ}}} |g_{mn\nu}(\mathbf{k},\mathbf{q})|^2 \times \left[\frac{n_{\mathbf{q}\nu} + f_{m\mathbf{k}+\mathbf{q}}}{\omega - (\varepsilon_{m\mathbf{k}+\mathbf{q}} - \varepsilon_{\mathrm{F}}) + \omega_\nu(\mathbf{q}) + \mathrm{i}\eta} + \frac{n_{\mathbf{q}\nu} + 1 - f_{m\mathbf{k}+\mathbf{q}}}{\omega - (\varepsilon_{m\mathbf{k}+\mathbf{q}} - \varepsilon_{\mathrm{F}}) - \omega_\nu(\mathbf{q}) + \mathrm{i}\eta} \right], \quad (1.44)$$

where $f_{n\mathbf{k}}$ is the Fermi-Dirac occupation factor, as introduced in Eq. (1.20), and $n_{\mathbf{q}\nu}$ is the Bose-Einstein distribution. Once the self-energy is computed, we can obtain the QP energies using Eq. (1.24).

An important quantity in interacting many-body systems related to the self-energy is the spectral function:

$$A(\mathbf{k},\omega) = -\frac{1}{\pi} \sum_n \frac{\mathrm{Im}\Sigma_{n\mathbf{k}}(\omega)}{\left[\omega - \varepsilon_{n\mathbf{k}} - \mathrm{Re}\Sigma_{n\mathbf{k}}(\omega)\right]^2 + \left[\mathrm{Im}\Sigma_{n\mathbf{k}}(\omega)\right]^2}, \quad (1.45)$$

a quantity that is probed in angle-resolved photoemission spectroscopy (ARPES). Additionally, the carrier lifetime can be computed as

$$\frac{1}{\gamma_{n\mathbf{k}}} \approx 2\,\mathrm{Im}\left[\Sigma_{n\mathbf{k}}(\omega)\right], \quad (1.46)$$

corresponding to the width of the peaks in the spectral function.

1.5 The **exciting** code

All calculations presented in this thesis, except for geometry optimization, are performed using the **exciting** code [93], an all-electron full-potential package implementing the family of (linearized) augmented planewaves ((L)APW) plus local orbitals, *i.e.*, (L)APW+lo methods [108]. This method is known as the gold standard for solving the KS equations [109, 110]. Beyond the GS, **exciting** provides easy access to the excited-states properties by implementing the Green's functions formalism of MBPT, both in the G_0W_0 [83] and BSE [111] approach, as well as phonon-related properties.

1.5.1 Augmented planewave basis

In the (L)APW+lo method [93, 108], the unit cell is divided into the muffin-tin (MT) and interstitial (I) regions, as sketched in Fig. 1.2. The basis is defined as

$$\phi_{\mathbf{G}+\mathbf{k}}(\mathbf{r}) = \begin{cases} \sum_{\zeta lm} A_{\alpha\zeta lm}(\mathbf{k}+\mathbf{G})\, u_{\alpha\zeta l}(r^\alpha, \varepsilon_{\alpha l})\, Y_{lm}(\hat{\mathbf{r}}^\alpha) & r^\alpha < R^\alpha_{\mathrm{MT}}\,; \\ \frac{1}{\sqrt{\Omega}} \mathrm{e}^{\mathrm{i}(\mathbf{k}+\mathbf{G})\cdot\mathbf{r}} & \mathbf{r} \in I\,; \end{cases} \tag{1.47}$$

is the radius of the sphere of atom α, centered at position $\mathbf{R}_\alpha$, and the difference vector from this center is labeled as $\mathbf{r}^\alpha = \mathbf{r} - \mathbf{R}_\alpha$. Inside the MT spheres, $\phi_{\mathbf{G}+\mathbf{k}}(\mathbf{r})$ is expanded in terms of products of spherical harmonics $Y_{lm}(\hat{\mathbf{r}}^\alpha)$ and radial functions $u_{\alpha\zeta l}(r^\alpha, \varepsilon_{\alpha l})$. The latter are solutions of the scalar-relativistic radial Schrödinger equation for the spherically averaged Kohn-Sham potential in the respective sphere at fixed reference energies $\varepsilon_{\alpha l}$ (linearization energies). The index ζ has been introduced to account for different types of radial functions, which are given by

$$u_{\alpha\zeta l}(r^\alpha, \varepsilon_{\alpha l}) \equiv \left.\frac{\partial^\zeta u_{\alpha l}(r^\alpha, E)}{\partial E^\zeta}\right|_{\varepsilon_{\alpha l}} . \tag{1.48}$$

Usually only $\zeta = 0, 1$ are considered. The augmentation coefficients $A_{\alpha\zeta lm}(\mathbf{k}+\mathbf{G})$ are chosen to make the basis functions to be continuous and smooth at the sphere boundary. Another approach to perform the linearization is picking frozen energy parameters for the radial functions and combining them with local orbitals (lo) [112, 113]. They are defined as

$$\phi_\mu(\mathbf{r}) = \left[a_\mu\, u_{\alpha l}(r^\alpha, \varepsilon_{\alpha l}) + b_\mu\, \dot{u}_{\alpha l}(r^\alpha, \varepsilon_{\alpha l})\right]\, Y_{lm}(\hat{\mathbf{r}}^\alpha)\, \delta_{\alpha\alpha_\mu}\, \delta_{\ell\ell_\mu}\, \delta_{mm_\mu}\,, \tag{1.49}$$

in one specific muffin-tin and as 0 everywhere else. The coefficients a_μ and b_μ are determined by imposing that the local orbitals are normalized and continuous at the sphere boundary. This results in a smaller linearization error compared to the (L)APW method [113].

1.5.2 Coulomb truncation and treatment of the $q = 0$ singularity

The **exciting** code has been designed for calculations with periodic boundary conditions of 3D materials. When treating 2D systems, a sufficient amount of vacuum is needed to avoid interaction between the replicas along the out-of-plane direction. Unlike DFT

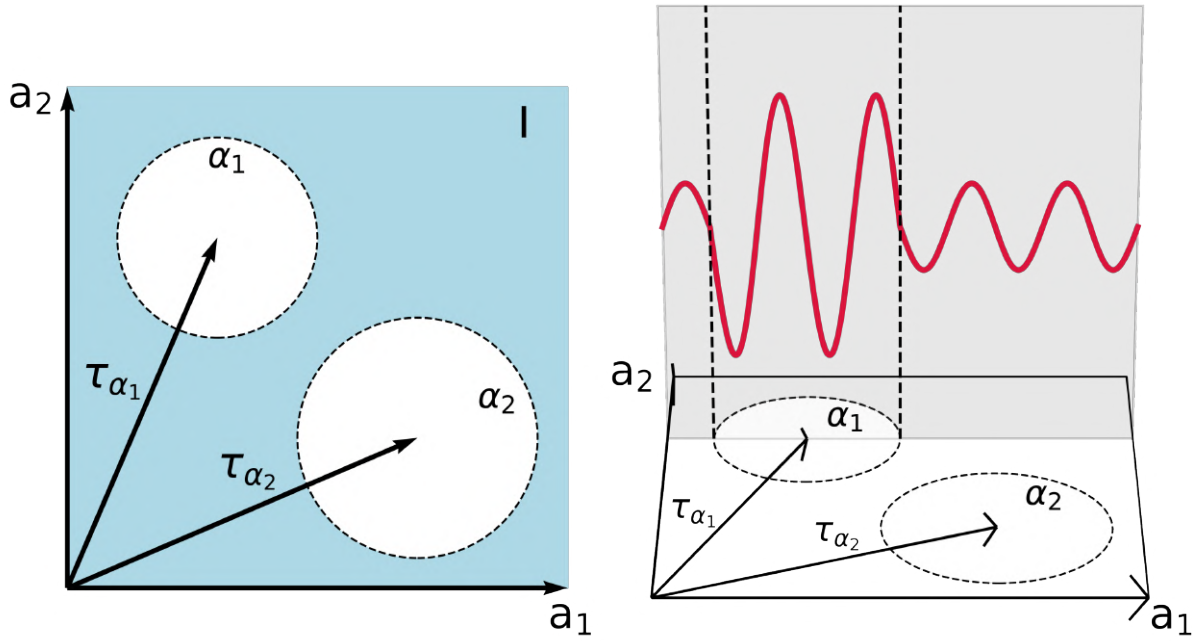

Figure 1.2: Scheme of a unit cell in the (L)APW representation.

calculations with (semi)local functionals, where the overlap between charge densities of neighboring periodic images decays rapidly with the vacuum-layer thickness, in the G_0W_0 approximation, the slow decay of the self-energy with the vacuum size complicates the task. In order to solve this issue, a truncation to the Coulomb potential is applied [114, 115], resulting in well-converged QP gaps with a considerable smaller vacuum size. In the 2D case, we truncate the Coulomb potential by a step function in the non-periodic direction (z axis)

$$V_{\mathrm{c}}^{\mathrm{trun}}(\mathbf{r}) = \frac{\theta(z_{\mathrm{c}} - |z|)}{|\mathbf{r}|}\,, \tag{1.50}$$

where z_{c} is the threshold for the Coulomb cutoff. In reciprocal space, and setting z_{c} to be half of the cell size along z, the potential is then written as

$$V_{\mathrm{c}}^{\mathrm{trun}}(\mathbf{k}) = \frac{4\pi}{|\mathbf{k}|^2}\left[1 - \mathrm{e}^{-k_{xy} z_{\mathrm{c}}} \cos(k_z z_{\mathrm{c}})\right]. \tag{1.51}$$

An inconvenient of the truncation of the Coulomb interaction is that the convergence with respect to the $\mathbf{k}$-grid slows down, due to the non-smooth behavior of the dielectric

function around the singularity at $\mathbf{q} = 0$ [116–118]. To solve this problem, the correlation part of W is treated analytically [117, 119]. The correlation part of the self-energy $\Sigma^c(\omega)$ without the treatment can be written as [82]

$$\langle \phi_{n\mathbf{k}} | \Sigma^c(\omega) | \phi_{n\mathbf{k}} \rangle = \frac{\mathrm{i}}{2\pi} \sum_{mij} \int_{-\infty}^{\infty} \mathrm{d}\omega' \frac{1}{N_{\mathbf{q}}} \sum_{\mathbf{q}} \frac{1}{\omega + \omega' - \tilde{\varepsilon}_{m\mathbf{k}-\mathbf{q}}} \times \left[M^i_{nm}(\mathbf{k}, \mathbf{q}) \right]^* M^j_{nm}(\mathbf{k}, \mathbf{q}) \, W^c_{ij}(\mathbf{k}, \mathbf{q}) \, , \tag{1.52}$$

where $M^i_{nm}(\mathbf{k}, \mathbf{q})$ are the expansion coefficients of the mixed product basis, an auxiliary basis to represent products of KS wavefunctions (more details in Chapter 6). To treat the $\mathbf{q} = 0$ contribution, separately, the corresponding term in Eq. (1.52) is replaced by

$$\frac{1}{\omega + \omega' - \tilde{\varepsilon}_{m\mathbf{k}}} \left[M^i_{nm}(\mathbf{k}, 0) \right]^* M^j_{nm}(\mathbf{k}, 0) \, \frac{1}{\Omega_0} \int_{\Omega_0} \mathrm{d}\mathbf{q} \, W^c_{ij}(\mathbf{q}, \omega'), \tag{1.53}$$

where Ω_0 is a small region around $\mathbf{q} = 0$. Analytical expressions in the limit $\mathbf{q} \to 0$ are then employed to calculate the integral in Eq. (1.53).

1.5.3 TS van der Waals correction

Van der Waals (vdW) interactions play an important role in weak interacting system, such as, the HIOS studied in this thesis. Unfortunately, conventional DFT calculations fail to describe the long-range vdW interactions because the exchange-correlation functional does not capture them. To address this problem, the total energy, including such a dispersion, can be expressed as

$$E_{\mathrm{tot}} = E_{\mathrm{DFT}} + E_{\mathrm{disp}} \tag{1.54}$$

where E_{disp} represents the long-range dispersion energy. In the Tkatchenko-Scheffler (TS) method [120, 121] the dispersion energy is given as

$$E_{\mathrm{disp}} = -\frac{1}{2} s_6 \sum_{ij} \frac{C_6^{ij}}{(r_{ij})^6} \, f_{\mathrm{d}}(r_{ij}) \, , \tag{1.55}$$

where s_6 represets a global scaling factor that depends on the exchange-correlation functional. Typically, $s_6 = 1$ for the PBE functional. r_{ij} is the interatomic distance between the i-th and j-th atoms. C_6^{ij} are the dispersion coefficients, and f_{d} is a damping function

that prevents singularities for small interatomic distances,

$$f_{\mathrm{d}}(r_{ij}) = \frac{1}{1+\exp\Big\{-d\big[r_{ij}/\left(s_{\mathrm{R}}R_{ij}\right)-1\big]\Big\}} \,. \tag{1.56}$$

For the PBE functional, the damping parameter d is equal to 20, while the scaling parameter s_{R} is set to 0.94. R_{ij} is the sum of the atomic vdW radii, *i.e.*, $R_{ij} = R_i + R_j$. In the TS method, the radii R_i are rescaled as

$$R_i = R_i^{\mathrm{free}} \left(\frac{V_i^{\mathrm{eff}}}{V_i^{\mathrm{free}}}\right)^{1/3} \,. \tag{1.57}$$

where V_i^{eff} and V_i^{free} are the effective volume of atom i in a solid and the volume of a free atom, respectively. To compute the ratio, the Hirshfeld partioning is used [122]

$$\frac{V_i^{\mathrm{eff}}}{V_i^{\mathrm{free}}} = \frac{\int \mathrm{d}\mathbf{r}\; r^3\, \rho(\mathbf{r})\, w_i(\mathbf{r})}{\int \mathrm{d}\mathbf{r}\; r^3\, \rho_i^{\mathrm{free}}(\mathbf{r})} \,, \tag{1.58}$$

where the weigh for atom i, $w_i(\mathbf{r})$, takes the form

$$w_i(\mathbf{r}) = \frac{\rho_i^{\mathrm{free}}(\mathbf{r})}{\sum_j \rho_j^{\mathrm{free}}(\mathbf{r})} \,. \tag{1.59}$$

The dispersion coefficients with $i = j$, C_6^{ii}, in a solid can be calculated as

$$C_6^{ii} = C_{6,\mathrm{free}}^{ii} \left(\frac{V_i^{\mathrm{eff}}}{V_i^{\mathrm{free}}}\right)^2 \,. \tag{1.60}$$

The off-diagonal C_6^{ij} coefficients are estimated by the Slater-Kirkwood formula [123, 124]

$$C_6^{ij} = \frac{2C_6^{ii}C_6^{jj}}{\frac{\upsilon_j}{\upsilon_i}C_6^{ii} + \frac{\upsilon_j}{\upsilon_i}C_6^{jj}} \,, \tag{1.61}$$

with υ_i defined as the static polarizability of atom i,

$$\upsilon_i = \upsilon_i^{\mathrm{free}} \frac{V_i^{\mathrm{eff}}}{V_i^{\mathrm{free}}} \,. \tag{1.62}$$

The methods of theoretical physics should be applicable to all those branches of thought in which the essential features are expressible with numbers.

Paul Dirac

2 Transition metal dichalcogenides

This chapter focuses on the inorganic components of our prototypical HIOS, namely, monolayers of molybdenum disulfide (MoS_2) and tungsten diselenide (WSe_2). In particular, we consider the hexagonal (2H) phase of these crystals, and we compute their structural, electronic, vibrational, and optical properties from first principles. These semiconducting few-layer transition metal dichalcogenides (TMDCs) exhibit remarkable properties, such as direct band gaps [125], strong light-matter interaction [126], and large exciton binding energies [50, 127].

2.1 Molybdenum disulfide

Molybdenum disulfide (MoS_2) monolayer is the second most studied 2D material after graphene, both theoretically [28, 32, 34–36, 116–118, 127–155] and experimentally [125, 126, 140, 156–163]. We begin by describing the crystal structure of bulk MoS_2, since this is the starting point to build our monolayer. The bulk structure can be described as closed-packed planes of Mo atoms, sandwiched between two atomic layers of S atoms. The S-Mo-S bonds are covalent and strong, while the monolayers are loosely stacked upon each other by vdW interactions. The Mo atoms are surrounded by 6 S atoms in a trigonal prismatic geometry as illustrated in Fig. 2.1 (right). The corresponding Bravais lattice is hexagonal and the non-symmorphic space group of the crystal is $P6_3/mmc$. The two Mo atoms are located at the 2c Wyckoff sites, the four S atoms at the 4f sites [127].

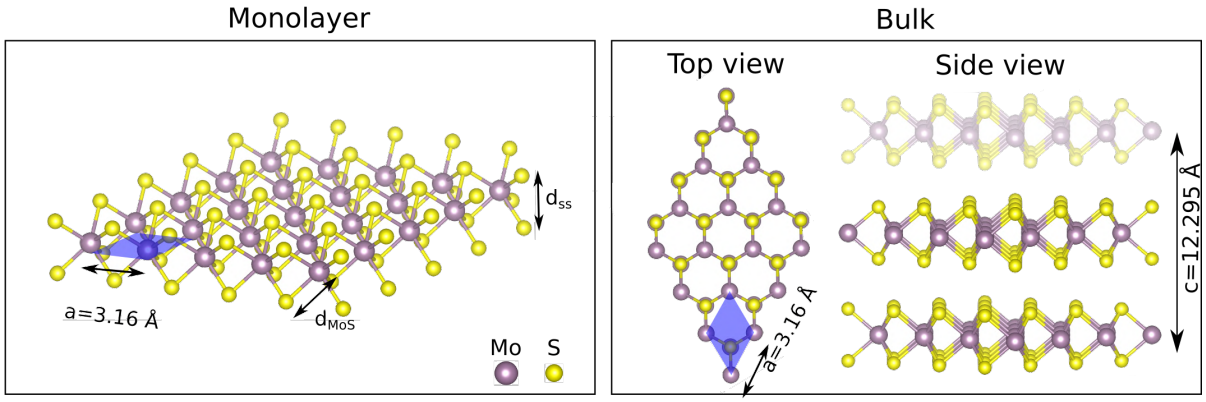

Figure 2.1: Left: 2D structure of a MoS_2 monolayer, where the unit cell contains two selenium atoms and one molybdenum. The in-plane lattice parameter is denoted by a. Right: Bulk structure of MoS_2, which contains four selenium and two molybdenum atoms. The individual slabs are stacked via vdW interactions. The out-of-plane lattice constant is denoted by c.

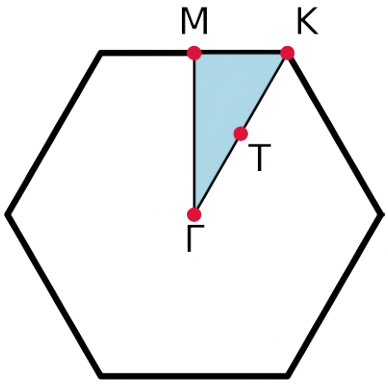

Figure 2.2: Brillouin zone (BZ) of the hexagonal crystal. The high-symmetry points (Γ, M and K) and the path, along which the bandstructure is calculated. The irreducible BZ is highlighted in blue.

To construct the MoS_2 monolayer, a single layer is extracted from the bulk structure. Its geometry, depicted in Fig. 2.1 (left), is determined by the in-plane lattice parameter a and the distance between the sulfur atoms, d_{SS}. Figure 2.2 shows the high-symmetry points for the 2D hexagonal Brillouin zone (BZ) and the path along which the electronic and phonon dispersions are calculated. The MoS_2 monolayer retains the intrinsic trigonal prismatic arrangement of the Mo and S atoms. However, the inversion symmetry is broken and the new space group is $P\bar{6}m2$ [127, 139].

2.1.1 Geometry optimization

The first step in any theoretical study is to obtain the optimized geometry. In this work, we have performed the geometry optimization using FHI-aims [164], an all-electron code implementing numerical atomic orbitals (NAO). It is done by minimizing the amplitudes of the interatomic forces, below a threshold value of 10^{-3} eV Å^{-1}. Although FHI-aims implements a different basis set than **exciting**, the two codes have been shown to be in very good agreement [110]. In Table 2.1, we list the structural parameters of MoS_2 monolayer optimized with LDA, PBE, and HSE. To include vdW corrections, we have performed calculations using the TS method [120, 121] based on PBE (HSE), labeled as PBE+TS (HSE+TS). As expected, LDA underestimates the lattice spacing, whereas PBE overestimates it, while HSE and PBE+TS show the best performance with respect to the experimental value. The calculated S-S bond length is underestimated regardless of the method used, with PBE+TS being the closest to the experimental counterpart.

Table 2.1: Optimized geometry parameters of MoS_2 monolayer obtained with different XC functionals, and compared with the experimental value reported in Ref.[163].

XC functional	a [Å]	d_{SS} [Å]	d_{MoS} [Å]	θ [°]
LDA	3.121	3.106	2.379	81.51
PBE	3.186	3.125	2.414	80.70
HSE	3.160	3.101	2.394	80.73
PBE+TS	3.162	3.136	2.407	81.34
HSE+TS	3.139	3.111	2.388	81.28
Experiment [163]	3.160	3.172		

For all XC functionals considered, the S-S bond length, d_{SS}, decreases with increasing a, as shown in Fig. 2.3 on the right. Both PBE and PBE+TS yield the same trend. However, the difference lies in the optimized lattice parameter, 3.186 Å and 3.162 Å respectively, which leads to larger d_{SS} in the case of PBE+TS. The longest value of the Mo-S bond length, d_{MoS}, is obtained with PBE, while the shortest value is obtained with LDA, identical to the case of the lattice parameter. The angle between the S-Mo-S atoms, θ, has its smallest value when calculated with PBE, while the largest value is obtained for LDA, completely opposite to the case of the lattice parameter. Overall, HSE and the PBE+TS method give the closest result to the experimental lattice parameter, approximately 3.16 Å.

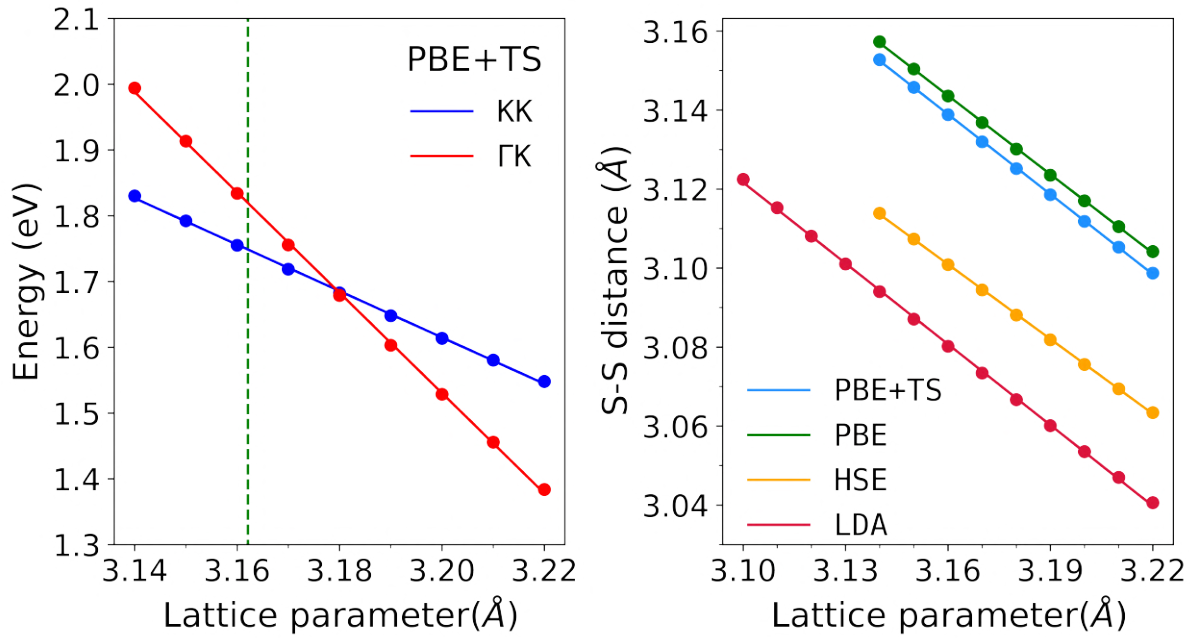

Figure 2.3: Left: Direct and indirect band gaps for the PBE+TS geometry. The green line corresponds to the optimized value reported in Table 2.1 for PBE+TS. Right: Dependence of d_{SS} on the lattice constant a obtained from different XC functionals.

2.1.2 Electronic properties

For the geometries described above, we calculate the direct and indirect band gaps using the same XC functionals as in the geometry optimization, *i.e.*, we use LDA on top of the LDA geometry, PBE on top of the PBE geometry and so on. We consider here the direct gap at the **K** point (E_g(**KK**)) as well as the indirect gaps between **Γ** and **K** (E_g(**ΓK**)) and between **K** and **T** (E_g(**KT**)). The **T** point corresponds to a point between towards **Γ** and **K**, see Fig. 2.2. The values for the direct gap and the indirect gaps are given in Table 2.2. Regardless of the method chosen, E_g(**KK**) corresponds to the fundamental gap, except for the PBE case, where the fundamental gap is indirect, *i.e.*, E_g(**ΓK**). This is a clear difference from the optimized geometry using PBE and PBE+TS. To better understand this difference, we examine the effect of the lattice parameter on the direct and indirect band gap for the PBE+TS geometry, as shown in the left panel of Fig. 2.3. At the optimized lattice parameter (green dashed line in Fig. 2.3), a direct fundamental gap is obtained at the **K** point. As the lattice parameter increases, the character of the gap changes from direct to indirect. In fact, the PBE lattice parameter of 3.18 Å has an energy of approximately 1.7 eV, which coincides with the transition from direct to

indirect fundamental gap.

Table 2.2: Direct and indirect band gaps of the MoS_2 monolayer obtained with LDA, PBE, HSE, and PBE+TS. For each case, the fundamental gap is highlighted in bold.

Functional	$E_g(\mathbf{KK})$ [eV]	$E_g(\mathbf{\Gamma K})$ [eV]	$E_g(\mathbf{KT})$ [eV]
LDA	**1.86**	1.96	1.97
PBE	1.67	**1.65**	1.94
HSE	**2.19**	2.23	2.60
PBE+TS	**1.75**	1.82	1.92
HSE+TS	**2.28**	2.41	2.51
Experiment [165]	2.50		

Overall, all XC functionals underestimate the experimental gap of 2.50 eV [165], measured by photocurrent spectroscopy. HSE+TS has the closest value with 2.28 eV, a difference of approximately 0.2 eV. To overcome this issue, and to properly reproduce the experimental gap with our theoretical calculations we use MBPT within the G_0W_0 approximation. In conclusion, 2D materials, such as the MoS_2 monolayer, are highly sensitive to the structural parameters, and a small change in the lattice constant already has a large impact on the energy gap [118, 135, 139].

Before describing the QP band structure, we discuss two important aspects. The first aspect concerns whether a direct or an indirect gap is found. This depends on the dimensionality [31, 127] of the system. We compare the band structures of bulk and monolayer calculated with PBE+TS, as shown in Fig. 2.4. The fundamental band gap of the bulk structure is 0.87 eV, that of the monolayer is 1.75 eV. The indirect gap from $\mathbf{\Gamma}$ to $\mathbf{T}$ represents the fundamental band gap in the bulk system.

The second aspect to consider in the description of the electronic properties is spin-orbit coupling (SOC) [166]. We show the band structure of MoS_2 monolayer including SOC for the PBE+TS geometry in Fig. 2.5. There are three main features with the inclusion of SOC: First, the fundamental gap is reduced to 1.60 eV. Second, the valence band maximum (VBM) splitting at $\mathbf{K}$ amounts to 148 meV, in good agreement with Ref. [166]. Third, the conduction band splitting at $\mathbf{T}$ is approximately 3 meV.

We conclude this section by showing in Fig. 2.6 the band structure of the MoS_2 monolayer as obtained from PBE and G_0W_0 calculations. The QP band structure is calculated on top of the PBE eigenvalues. The QP gap amounts to 2.6 eV, an increase

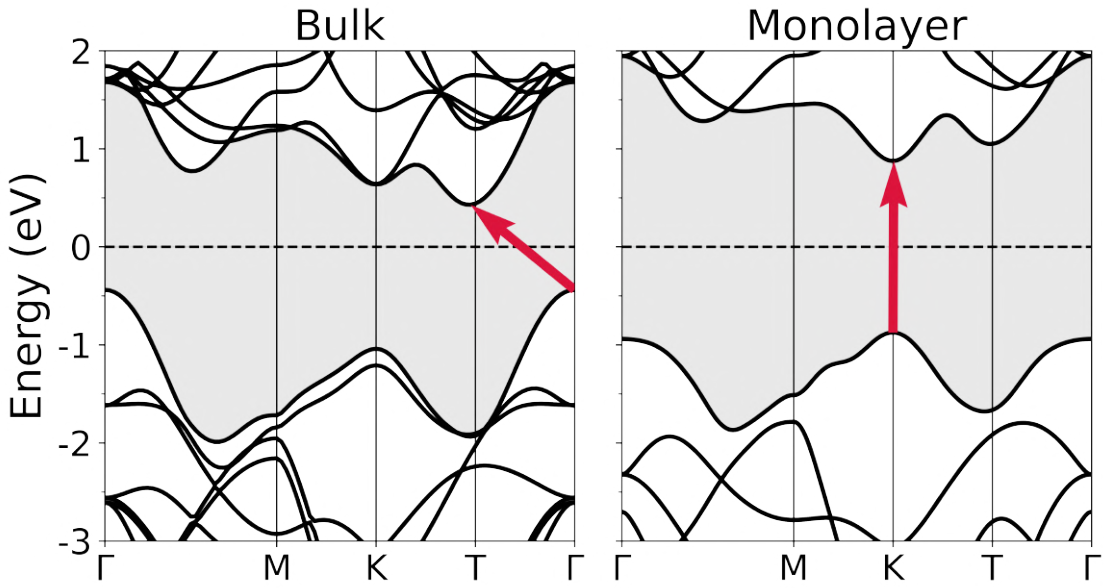

Figure 2.4: Band structure of bulk (left) and monolayer (right) MoS_2 obtained by PBE+TS, showing an indirect and direct fundamental gap (red arrows), respectively.

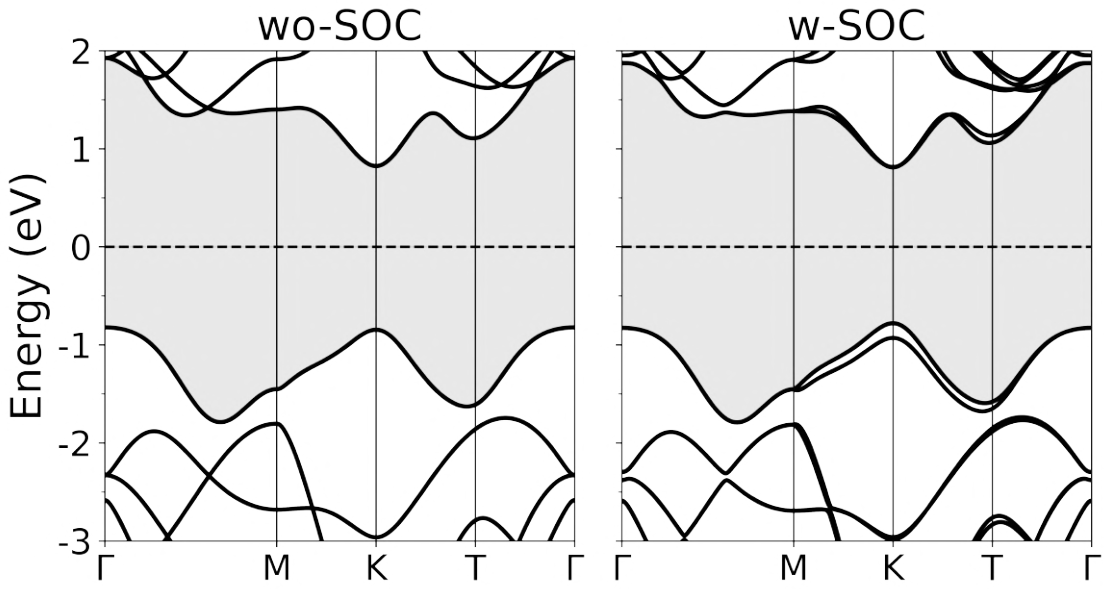

Figure 2.5: Band structure of MoS_2 monolayer in the PBE+TS geometry without (left) and with (right) spin-orbit coupling (SOC).

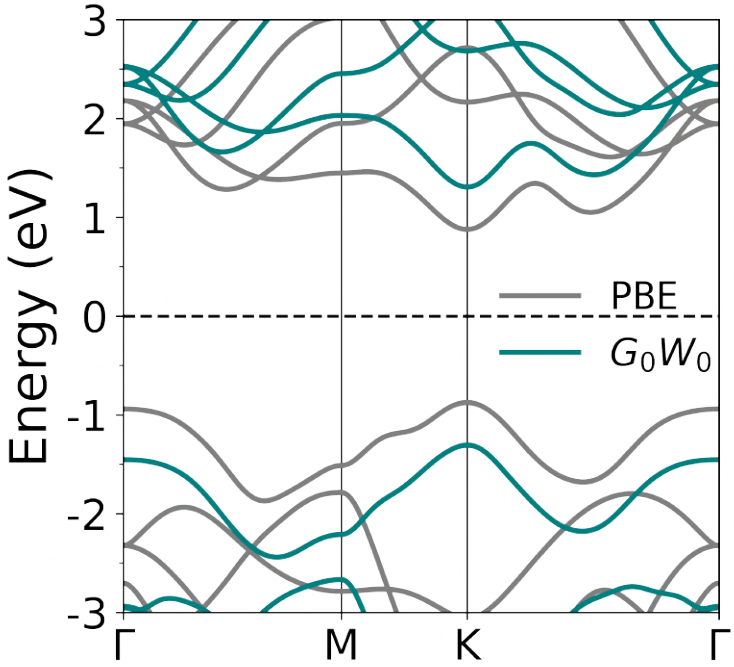

Figure 2.6: Band structure of MoS_2 monolayer calculated with PBE and G_0W_0.

of 0.9 eV from the KS band gap of 1.7 eV. As expected, the QP gap agrees more closely with the experimental value of 2.5 eV.

2.1.3 Phonon dispersion

The phonon dispersions of MoS_2 bulk and monolayer are shown in the left and right panels of Fig. 2.7, respectively. The interatomic force constants are calculated by the finite-displacement method using PBE as the exchange-correlation functional. The LO/TO splitting is included by calculating the Born effective charges and the macroscopic dielectric constant. The latter is important for polar systems, since the phonons can couple to macroscopic electric fields in the long-wavelength limit [127].

The phonon dispersion of bulk MoS_2 contains 18 phonon branches, which are reduced to nine in the monolayer case. There is very little difference in the optical phonons between the bulk and the monolayer, which is explained by the weak interlayer interaction. For both materials, the largest phonon energy is roughly 60 meV. In 2D materials, the violation of the rotational invariance is expected to affect the out-of-plane flexural acoustic mode [167] by exhibiting negative energies when approaching $\mathbf{\Gamma}$, but the phonon dispersion of the MoS_2 monolayer shows minimal affection. Overall, the phonon dispersions of

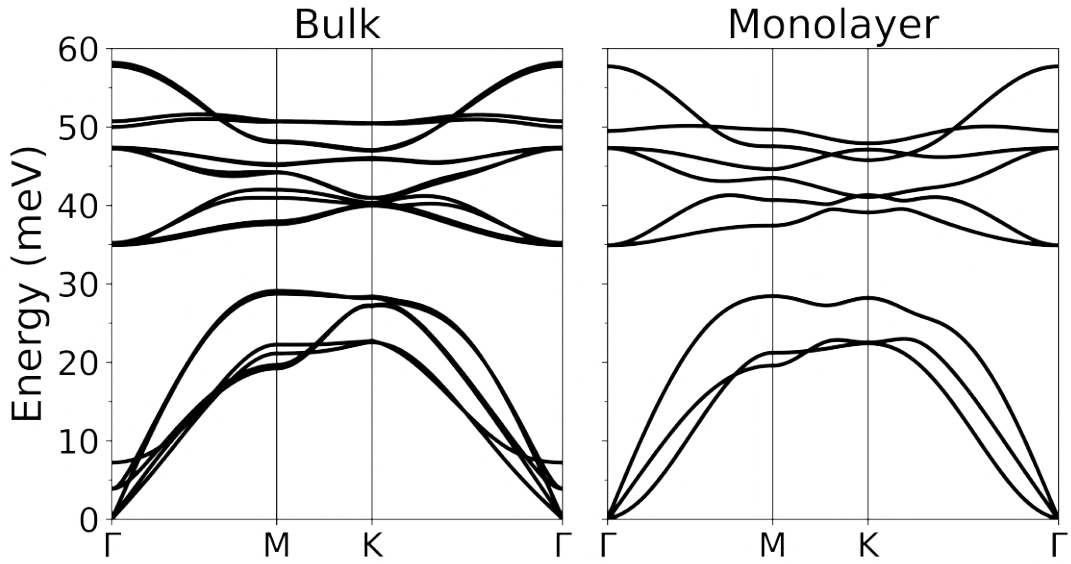

Figure 2.7: Phonon dispersion of bulk (left) and monolayer MoS_2 (right).

both materials are remarkably similar.

2.1.4 Electron-phonon interaction

After presenting the electronic and vibrational properties in the previous sections, we compute the electron-phonon interaction in the MoS_2 monolayer. The electron-phonon matrix elements (Eq. (1.38)) and the electron-phonon self-energy (Eq. (1.44)) are calculated using the QP eigenvalues obtained from the G_0W_0 approximation. Our study is not limited to just the temperature-dependent band gap, but we extend the investigation to the complete band structure and the features obtained by analyzing the spectral function.

We begin our discussion by showing the temperature-dependent band structure for 0K, 300K, 600K, and 900K in Fig. 2.8. We immediately notice that the band gap decreases as the temperature increases. This renormalization of the bands is expected, as also observed in Ref. [129]. Interestingly, in our calculations, we also observe a spectral signature on the lower parabola in the top valence band at the minimum between **K** and **Γ**. Another feature is observed at 600K and 900K, where the parabolic shape at the VBM experiences a distortion. Overall, as the temperature increases, in particular the lower- and higher-energy bands become more distorted.

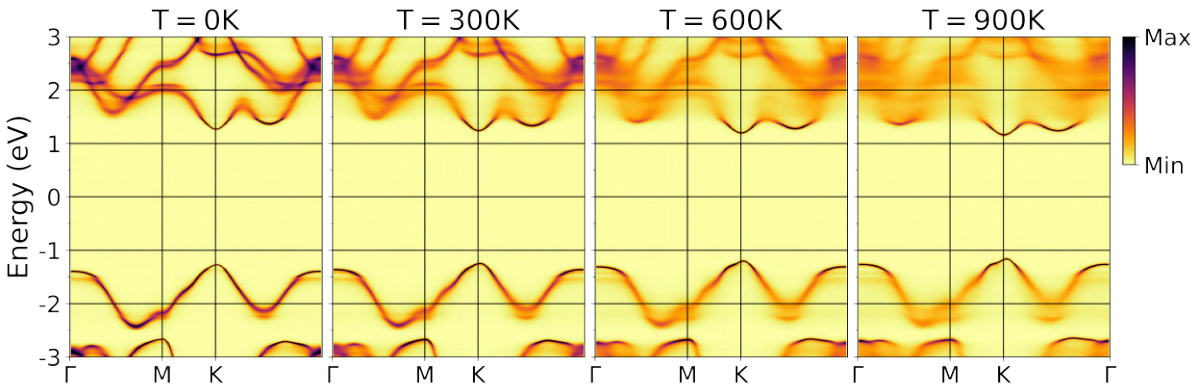

Figure 2.8: Temperature-dependent band structure of the MoS_2 monolayer. The color scale bar indicates the maximum value (black) and minimum value (white) of the spectral function, respectively.

To further investigate the band gap renormalization due to temperature effects, we plot in the left panel of Fig. 2.9 the spectral function of the VBM and conduction band minimum (CBM), for temperatures ranging from 0K to 900K, in 100K steps. As expected, we observe a renormalization in energy with a slight increase in broadening as the temperature increases. This indicates that the electron lifetimes at the band edges are reduced upon increasing temperature. The band gap renormalization, as derived from the spectral functions of the band edges, is shown in the right panel of Fig. 2.9.

This difference between the band gap at 0K and the band gap obtained from the G_0W_0 approximation amounts to 60 meV, in reasonable good agreement with the 75 meV reported in Ref.[129, 168]. The difference of 15 meV could be explained due to the fact that we have only considered the FM self-energy, thus neglecting the effect of the DW term. This would mean that the DW term adds up to 15 meV to the zero-point renormalization (ZPR) in this material. The latter would be consistent with the typical contribution of the DW term.

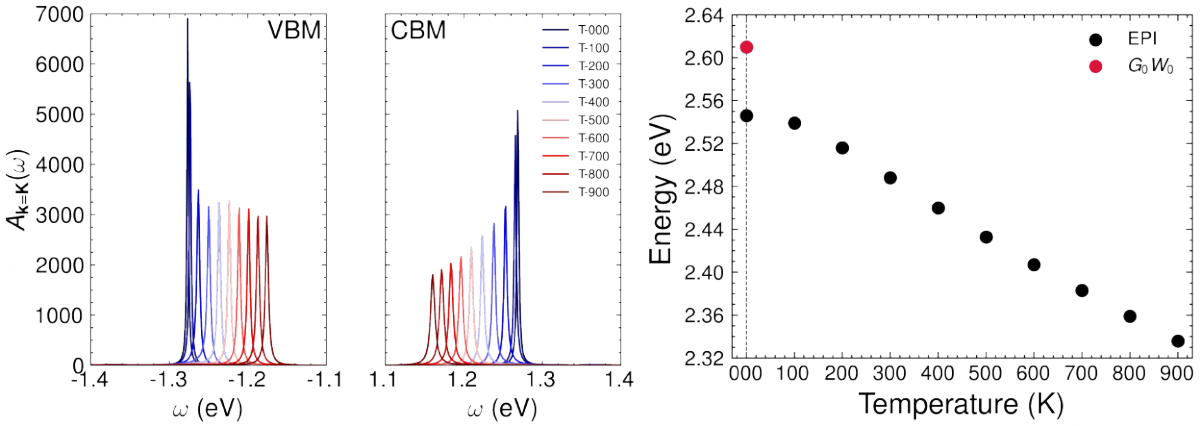

Figure 2.9: Spectral functions for the VBM and CBM of the the MoS_2 monolayer (left) and temperature-dependence of the band gap (right). The QP gap obtained with the G_0W_0 approximation is indicated by the red dot.

2.1.5 Optical properties

The imaginary part of the frequency-dependent macroscopic dielectric function of MoS_2 monolayer is shown in Fig. 2.10. It is obtained by solving the BSE on top of the QP band structure. For comparison, we show the independent quasi-particle approximation (IQPA) spectrum, which ignores excitonic effects. The difference between the two spectra highlights the large contribution of the electron-hole interactions for this system [32, 129]. To reduce computational cost, we have neglected the effects of SOC, its impact on the electronic structure have been shown in Section 2.1.2. The most prominent result is the splitting of the VBM at the **K**-point, which leads to a splitting of the lowest-energy exciton peak by 150 meV [166]. The optical gap of 2.29 eV is overestimated, when compared to values reported from similar calculations [19, 52]. Thebinding energy of the lowest-energy exciton is estimated as the difference between the electronic gap (2.6 eV) and the optical gap (2.29 eV), yielding a value of 310 meV, which corresponds to a medium-sized exciton binding energy.

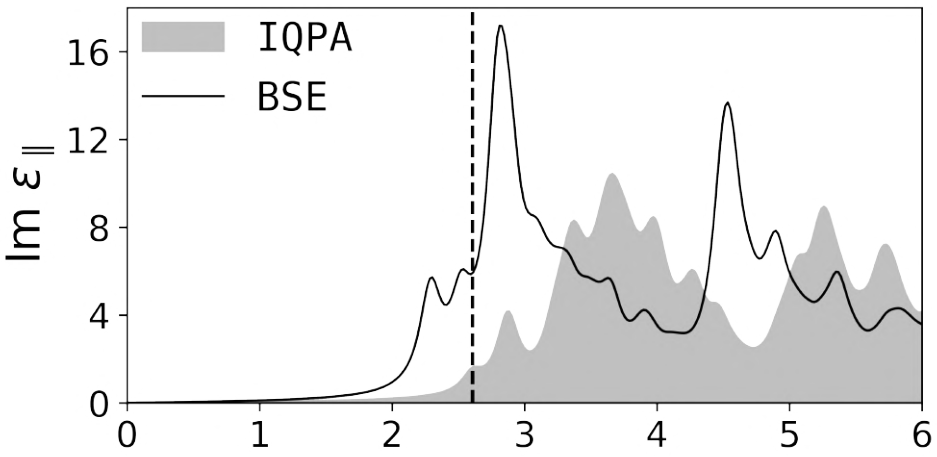

Figure 2.10: Imaginary part of the dielectric function of MoS_2 monolayer averaged over the in-plane components, including (BSE, solid lines) and negletic (IQPA, gray area) excitonic effects. Note that SOC has not been accounted for.

2.2 Tungsten diselenide

2.2.1 Geometry optimization

The crystal structure of WSe_2 belongs to the same crystal family as MoS_2. The geometry of WSe_2 monolayer, shown in the left panel of Fig. 2.11, is determined by the in-place lattice parameter a and the bond length between the selenium atoms, d_{SeSe}. The unit-cell size $\mathbf{L}$ along the out-of-plane direction z is chosen to be 20 Å in our calculations. Geometry optimization is performed using PBE, resulting in a and d_{SeSe} values of 3.32 Åand 3.36 Å, respectively, which are in good agreement with other theoretical studies [28, 116, 143, 145, 147, 150]. The geometry of the WSe_2 bilayer is shown in the right panel of Fig. 2.11. The interlayer distance d has a value of 3.21 Å, after optimization using the TS vdW correction. We choose the bilayer to show the effect of dimensionality on the electronic, vibrational, and optical properties of WSe_2.

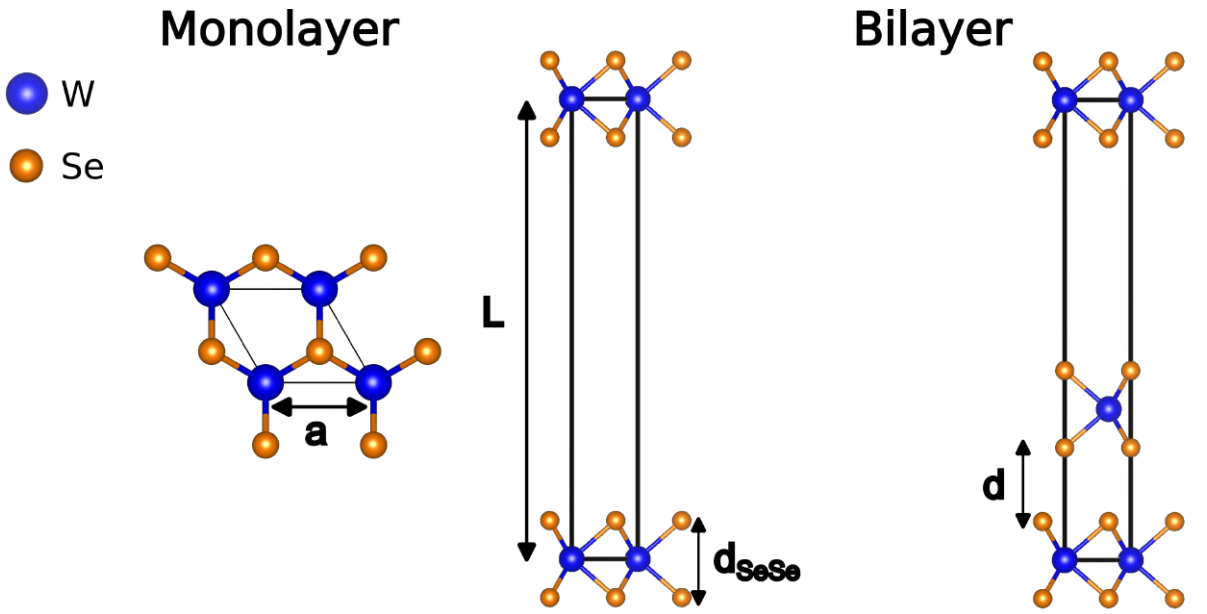

Figure 2.11: Left: 2D geometry of the WSe_2 monolayer. The in-plane lattice parameter is denoted by *a*. d_{SeSe} is the distance between Se atoms of the two atomic Se layers. **L** is the unit cell size size along the out-of-plane direction *z*. Right: Geometry of WSe_2 bilaye in AB stacking. The interlayer distance is denoted by *d*.

2.2.2 Electronic properties

We begin by describing the PBE band structure of WSe_2 bilayer, as shown in the left panel of Fig. 2.12. The fundamental band gap of WSe_2 bilayer is 1.4 eV, resulting from the indirect gap, $E_g(\mathbf{\Gamma T})$. The direct band gap at **K** amounts to 1.5 eV, about 0.1 eV larger than the fundamental gap. The indirect gap $E_g(\mathbf{KT})$ has a value of about 1.48 eV, only slightly smaller than the fundamental gap. We use the PBE band structure as a starting point to calculate the QP band structure (violet), as shown in the left panel of Fig. 2.13. When self-energy effects are included, the fundamental gap still corresponds to the indirect band gap $E_g(\mathbf{\Gamma T})$, with a value of 1.8 eV. The QP gap has increased by 0.4 eV with respect to the PBE gap. The $E_g(\mathbf{KK})$ has increased by approximately 0.6 eV (from 1.5 eV to 2.1 eV).

In the case of the monolayer, the fundamental gap is assigned to $E_g(\mathbf{KK})$, as shown in the right panel of Fig. 2.12. The direct gap at **K** amounts to 1.6 eV. We calculate the QP band structure (green) on top of the PBE eigenvalues, as shown in the right panel of Fig. 2.13. The QP direct gap at **K** is 2.4 eV, an increase of 0.8 eV with respect to the PBE band gap, in good agreement with previous calculations [145, 147]. However, the QP gap

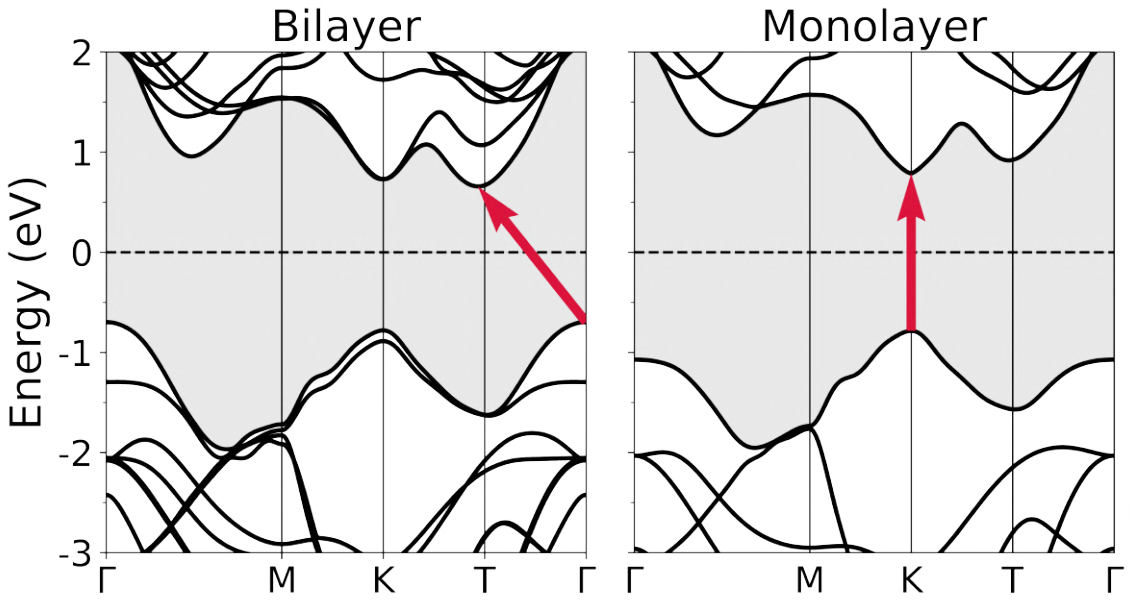

Figure 2.12: PBE band structure of WSe_2 bilayer (left) and monolayer (right). The indirect and direct fundamental gap are shown by red arrows.

is larger compared to the experimental value of 1.95 eV [65, 169], measured by scanning tunneling spectroscopy (STS). Overall, the G_0W_0 corrections are not uniform over all **k**-points, *i.e.*, a simple scissors approximation is, strictly speaking, not applicable [135].

The last aspect that we consider for the electronic properties of WSe_2 monolayer is the inclusion of SOC. Fig. 2.14 shows the band structure of WSe_2 monolayer without SOC (left) and with SOC (right) calculated with PBE. There are three main features, first, the fundamental gap is reduced to 1.34 eV, second, the valence band splitting at **K** is 456 meV, an increase of more than 300 meV with respect to the MoS_2 monolayer. Third, the conduction band splitting at **T** is about 44 meV. These results are in good agreement with Ref. [166]. We conclude this section by highlighting the main differences between the electronic properties of the WSe_2 bilayer and monolayer. First, there is a change in the fundamental band gap from direct (monolayer) to indirect (bilayer). Second, the reduction of the direct gap at **K** due to the additional layer. In the case of the bilayer, the gap is 0.3 eV smaller. This reduction can be explained by the additional screening introduced by the extra layer. These effects can only be capture via the *GW* approximation, and we will further emphasize this necessity with the examples of our prototypical HIOS.

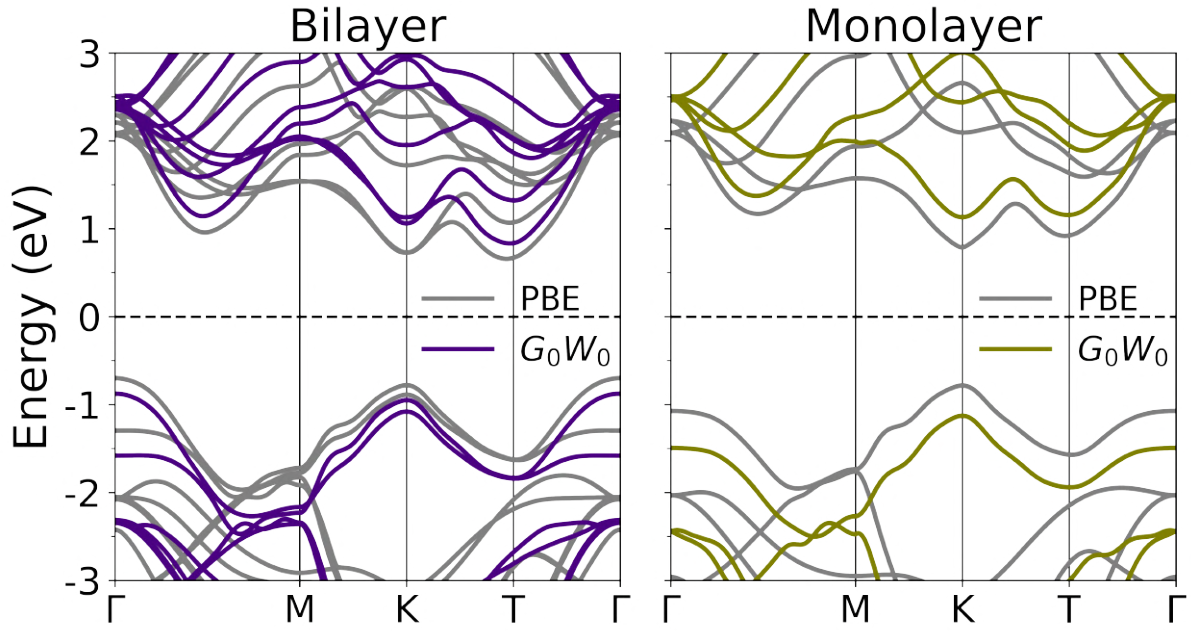

Figure 2.13: Left: QP band structure of WSe_2 bilayer (left) and WSe_2 monolayer (right).

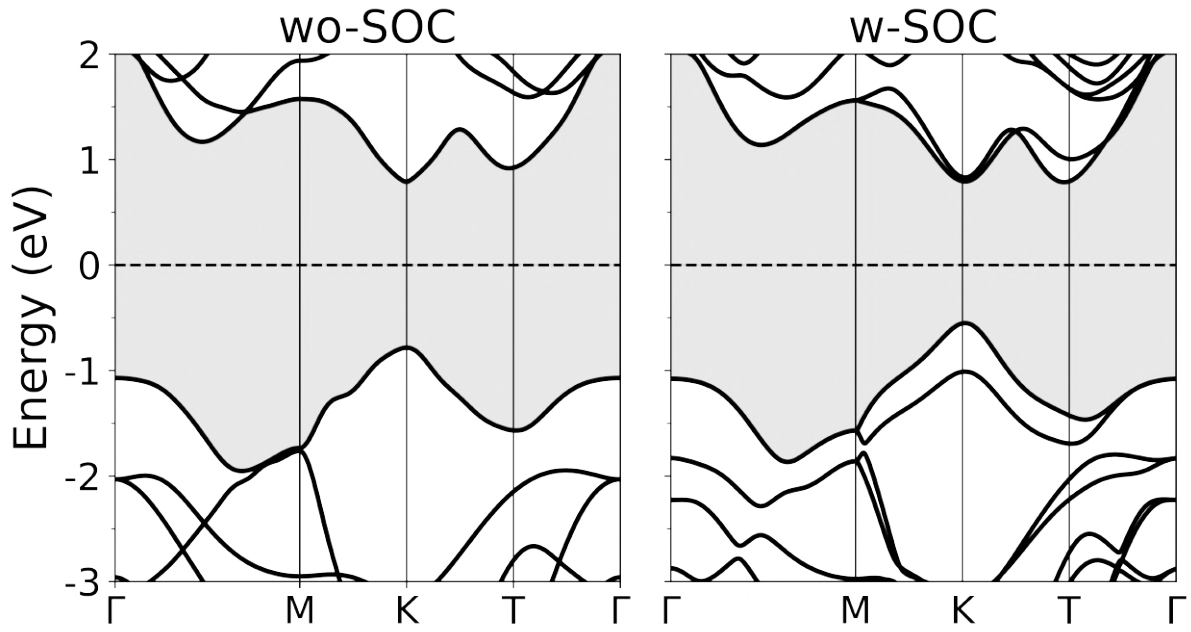

Figure 2.14: Band structure of monolayer WSe_2 without (left) and with (right) SOC.

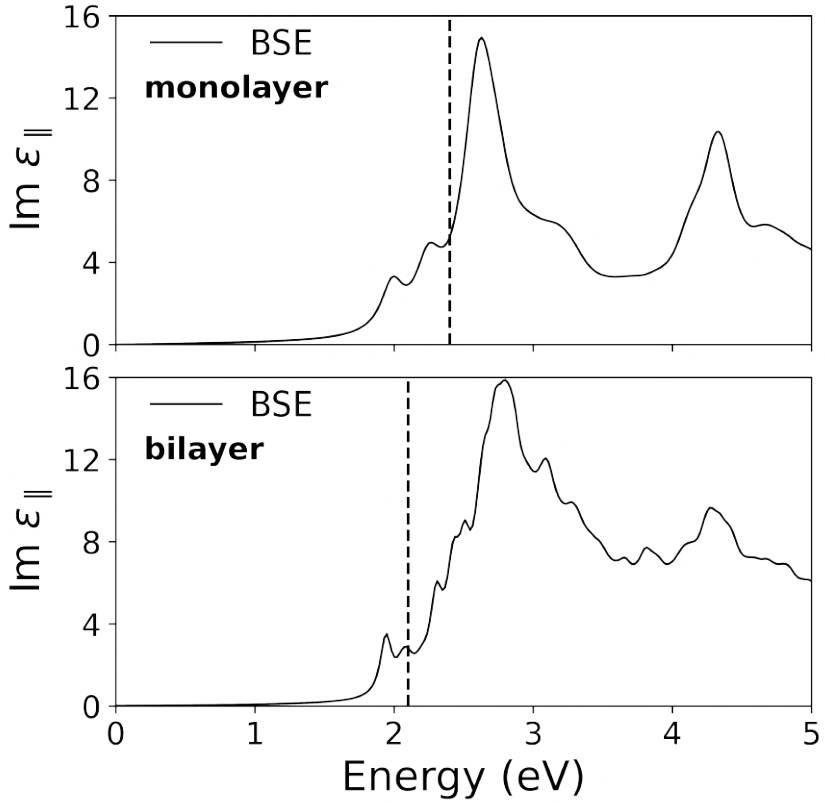

Figure 2.15: Imaginary part of the dielectric function of WSe_2 monolayer (top) and bilayer (bottom) averaged over the in-plane components, calculated with BSE. Note that SOC has not been accounted for.

2.2.3 Optical properties

In Fig. 2.15 we compare the imaginary part of the frequency-dependent macroscopic dielectric function between monolayer (top) and bilayer (bottom) as obtained by averaging over the in-plane components. The optical gap of the bilayer is approximately 1.95 eV, we estimate the exciton binding energy of the first exciton as 150 meV by using the direct gap at **K**. In the case of the monolayer, the optical gap amounts to 2.0 eV, a very close value to that of the bilayer. However, the binding energy of the lowest-energy exciton is about 300 meV higher with a value of 428 meV. Overall, both absorption spectra are very similar, but the additional screening reduces the optical gap of the bilayer.

Most important part of doing physics is the knowledge of approximation.

Lev Landau

3

Many-body effects in pyrene@MoS_2

In this chapter, we systematically study the electronic and optical properties of the prototypical system, pyrene@MoS_2. We calculate the QP correction to the PBE and HSE band structures of the heterostructure using the G_0W_0 approximation. From these results, we rationalize the level alignment of this system. Based on the QP band structure, we then solve the BSE to calculate the optical properties. Finally, we study the temperature-dependence of the band structure and spectral signatures arising from EPI.

3.1 Geometry optimization

We use a slab model to describe the 2D unit cell of the hybrid system. It consists of a 3×3×1 supercell of the pristine MoS_2 structure, *i.e.*, containing 9 Mo and 18 S atoms. We consider a starting configuration consisting of a monolayer of upright standing molecules at a vertical distance of about 3 Å. The internal coordinates of the combined system are then relaxed using PBE+TS. The adsorption geometry of pyrene turns out tilted by an angle of 17°. The shortest (largest) distance of the physisorbed molecule to the TMDC is 3.23 Å (4.28 Å), measured from the topmost atomic position of the substrate. This inclination is attributed to the weak interactions between neighboring molecules. Regardless of the inclination, at the separation distance, no chemical bonding occurs, *i.e.*, the interaction between pyrene and substrate is primarily due to vdW forces. The side and top views of the optimized supercell are shown in Fig. 3.1

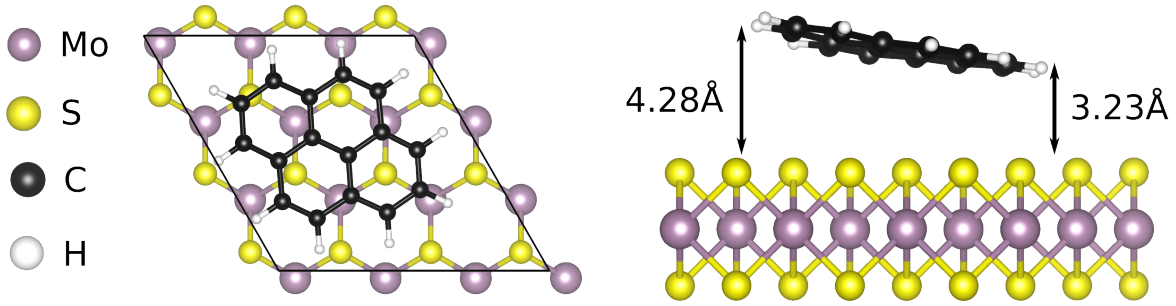

Figure 3.1: Side and top view of the optimized structure of pyrene@MoS_2 in a 3×3×1 MoS_2 supercell.

3.2 Electronic properties

The PBE band structure of the hybrid heterostructure is shown in Fig. 3.2 (left). The material exhibits a direct gap at the **Γ**-point. Its appearance at the **Γ** is a consequence of the band folding in the 3×3×1 supercell [170]. PBE yields an energy level alignment of type II, where the highest occupied molecular orbital (HOMO) of the molecular monolayer constitutes the highest occupied valence state, while the lowest-lying unoccupied states arise from the MoS_2 bands [52, 171]. The fundamental KS gap of this heterostructure is 1.3 eV. An analysis of the band features indicate that, at the PBE level, this vdW-bound hybrid system largely preserves the band structure of the pristine constituents. For example, the PBE band gap of MoS_2 coincides with the direct band gap of 1.7 eV in pristine MoS_2, as described in Chapter 2.

The adsorption of pyrene manifests itself through the emergence of a flat band around −0.6 eV in the valence region, as shown in the left panel of Fig. 3.2. Visualization of the corresponding wave function at the **Γ**-point (marked by the orange circle) confirms that this level corresponds to the HOMO of pyrene. The energy difference between the HOMO and the VBM of MoS_2 amounts to 0.4 eV, making hybridization of these states unlikely. Another flat band appears at around −1.5 eV. Inspecting the KS orbital (brown circle), it can be attributed to the HOMO-1 of pyrene. Both, HOMO and HOMO-1 are molecular orbitals of π character. The three topmost bands of MoS_2, *i.e.*, VBM, VB-1, and VB-2, are almost degenerate at **Γ**, with an energy of −1.1 eV. Visualization of the corresponding KS orbitals reveals the well-defined MoS_2 character, preserving the composition of Mo-4d and S-3p states (blue circles). Although there is hybridization between the molecular orbitals and the MoS_2 bands, it turns out to be minimal. This can be explained by the fact that pyrene has no permanent dipole and, thus, vdW forces

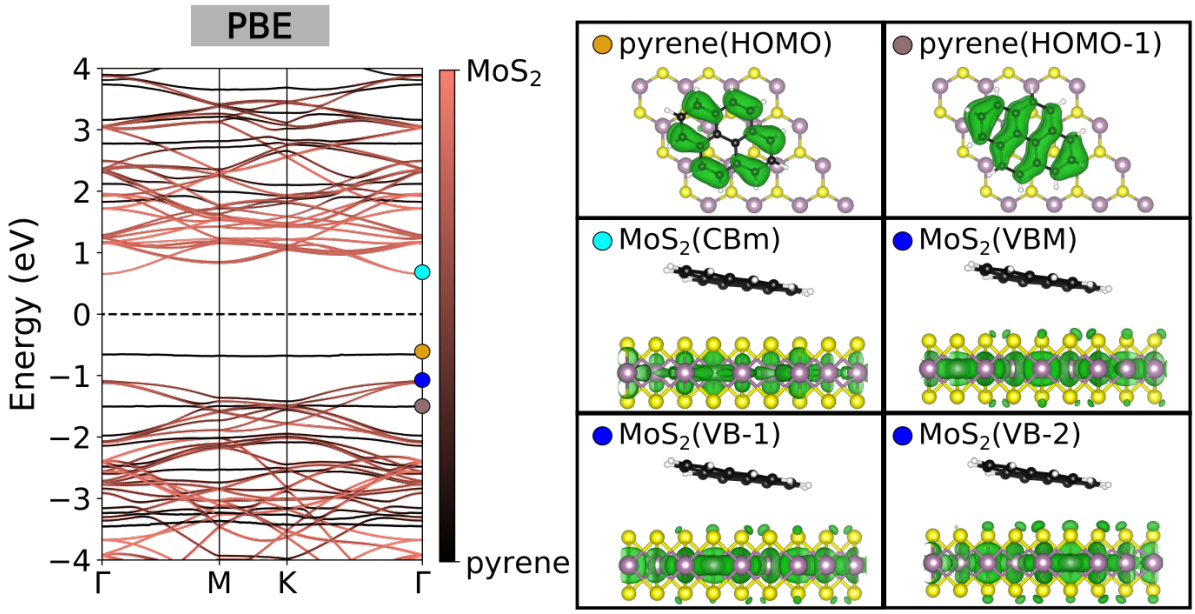

Figure 3.2: Left: Band structure of pyrene@MoS_2 calculated with PBE. The color code, going from red (MoS_2) to black (molecule), indicates the contribution of the pristine entities to the bands. Right: Kohn-Sham (KS) wave functions of selected bands at the **Γ**-point.

dominate the formation of the hybrid heterostructure. The lowest unoccupied molecular orbital (LUMO) of pyrene appears at an energy of about 1.9 eV, hence the HOMO-LUMO distance of pyrene in this system amounts to 2.5 eV.

To further investigate the level alignment at the PBE level, we unfold the bands into the BZ of the unit cell, as displayed in the left panel of Fig. 3.3. Both the HOMO and HOMO-1 are clearly observed at the **K**-point with energies of −0.6 and −1.5 eV, respectively. The band gap of MoS_2 at **K**, E_g(**KK**), is direct with a value of 1.7 eV. Overall, the band structure of Fig. 3.3 confirms the type-II level alignment with a fundamental gap of 1.3 eV as deduced above.

We calculate the plane-averaged charge density difference $\Delta\varrho$ along the vertical direction defined as

$$\Delta\varrho = \varrho_{\text{tot}} - (\varrho_{\text{MoS}_2} + \varrho_{\text{mol}}) \tag{3.1}$$

where ϱ_{tot}, ϱ_{MoS_2}, and ϱ_{mol} correspond to the plane-averaged charge density of the total pyrene@MoS_2 system, the isolated MoS_2 supercell, and the free standing pyridine monolayer, respectively. Significant oscillation are found at the interface between the substrate and the molecular layer, as seen in the right panel of Fig. 3.3. In other words,

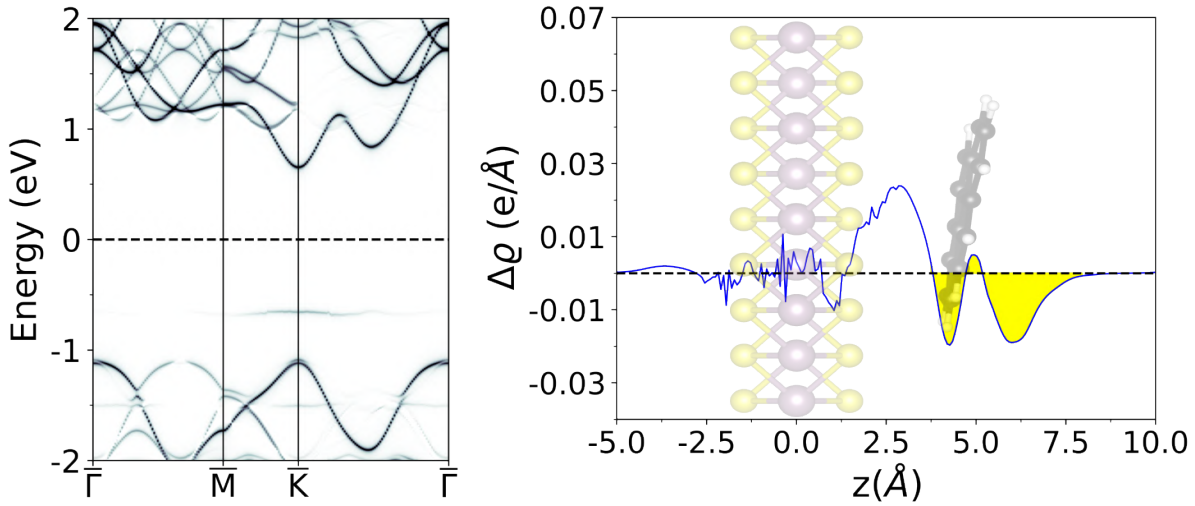

Figure 3.3: Left: PBE band structure of pyrene@MoS_2 unfolded to the BZ of the MoS_2 unit cell. Right: Plane-averaged charge-density difference between the heterostructure and the individual components along the z-direction. A positive (negative) value of $\Delta\varrho$ represents accumulation (depletion) of charge density.

the charge rearrangement is mainly confined to this region. The charge density is increased in the region just above the S-atom, while it is depleted in the region around the molecule, suggesting a donor behavior of pyrene. To quantify the amount of charge transfer, we integrate $\Delta\varrho$ in the region marked in yellow in the right panel of Fig. 3.3, obtaining -0.07 electrons.

After describing the PBE results of our system, we calculate the electronic properties using the G_0W_0 approximation with the PBE energies and wavefunctions as starting point. The QP band structure is plotted in Fig. 3.4 along the high-symmetry points in the BZ of the supercell (left) and the unit cell (right) of MoS_2. The HOMO of pyrene is now located below the three topmost valence bands of MoS_2, indicating a qualitatively change of the level alignment to type I.

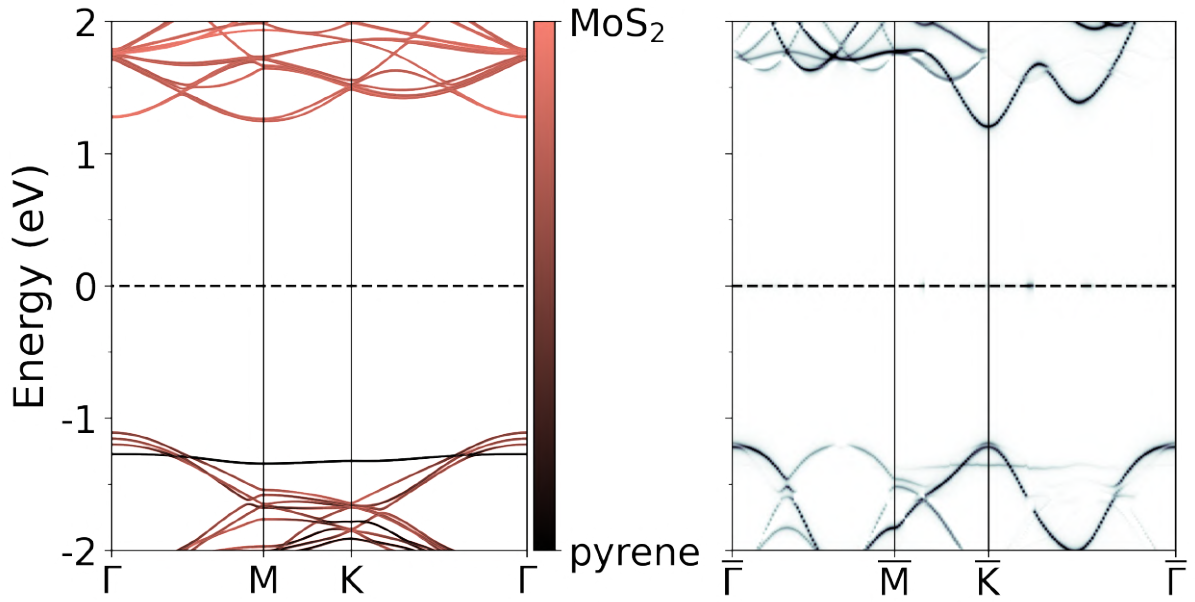

Figure 3.4: QP band structure of pyrene@MoS_2, computed using the G_0W_0 approximation, plotted along high-symmetry points in the BZ of the supercell (left) and the unit cell (right) of MoS_2.

To properly describe the effects of the G_0W_0 approximation on the electronic properties we plot the energy-level alignment as shown in Fig. 3.5. Here, the PBE HOMO/VBM of the isolated systems are aligned with their respective counterparts in the heterostructure. The PBE VBM of MoS_2 is taken as the global reference, which means that this level does not appear to be affected by G_0W_0 while all others are aligned with respect to it. Self-energy effects, also accounting for self-interaction correction, increase the band gaps of both components, while polarization effects induced by mutual interaction counteract the former [62, 171, 172]. At the MoS_2 side, the self-energy correction increases the gap from 1.7 eV to 2.3 eV, a value significantly smaller than the 2.6 eV gap found in pristine MoS_2. The reduction of the gap by -0.3 eV indicates that the molecular layer enhances the screening of the Coulomb interaction, described in Section 1.3.2. Also on the molecular side of the heterostructure, the electronic levels are renormalized by both effects. The renormalization of the HOMO-LUMO gap of pyrene in the hybrid system amounts to 1.2 eV. A large amount arises from the pronounced self-interaction error of KS-DFT, being removed at the G_0W_0 level [86, 173–175]. However, the corresponding value of the isolated molecular monolayer, is even much larger, *i.e.*, 2.7 eV. In other words, the polarization-induced renormalization of the HOMO-LUMO gap is as much as -1.5 eV. Table 3.1 summarizes the values of the self-energy correction for the band edges at the

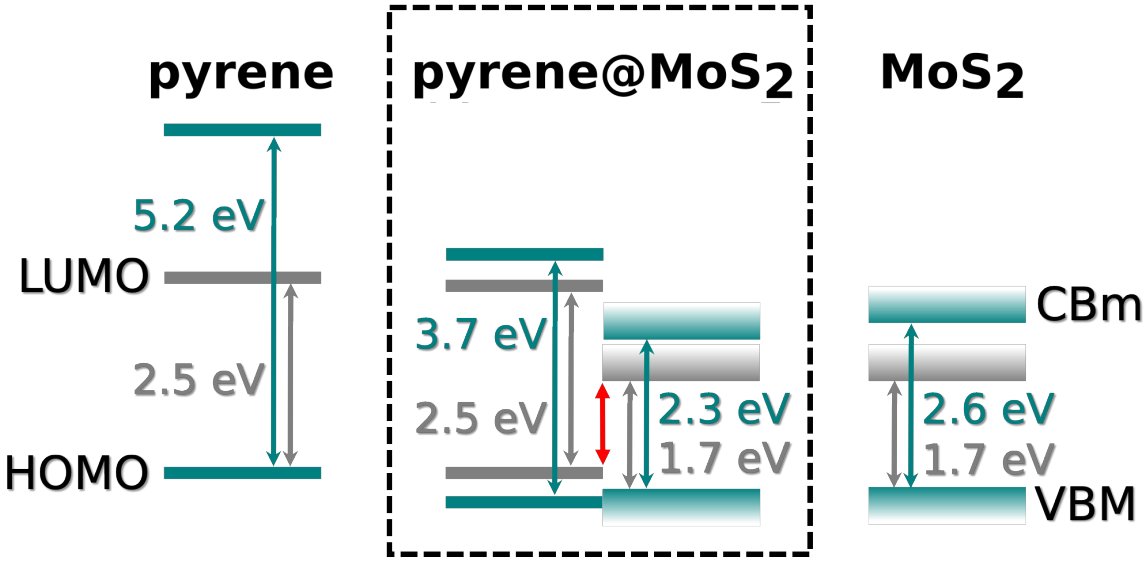

Figure 3.5: Energy-level alignment obtained from PBE (gray) and G_0W_0 (teal) for pyrene@MoS2. The middle panel shows the hybrid material, and the left (right) panel shows the corresponding scheme for the molecular monolayer (MoS_2 monolayer). The red arrow indicates the band gap as obtained from DFT.

heterostructure and the prisitine components.

Table 3.1: Energy renormalization, computed with the G_0W_0 approximation, of the HOMO-LUMO and the VBM-CBM distance of the pristine components and the heterostructure. The difference corresponds to the polarization-induced correction due to mutual screening between the components.

Gap/System	Pyrene	MoS_2	Pyrene@MoS_2
HOMO-LUMO (eV)	2.7	–	1.2
VBM-CBM (eV)	–	0.9	0.6

The QP correction is also evident in the density of states (DOS), displayed for pristine MoS_2 (top), the isolated molecular monolayer, and pyrene@MoS_2 (bottom panel) in Fig. 3.6. The most prominent difference between the molecular states from the isolated molecular layer and the heterostructure is seen in the unoccupied states, for example the LUMO is shifted from approximately 4 eV to about 2.5 eV, which corresponds to the -1.5 eV arising from polarization-induced effects.

At this point, we have argued that the type-II alignment at the PBE level is wrong, while G_0W_0 changes it to type I. Furthermore, the G_0W_0 approximation based on PBE

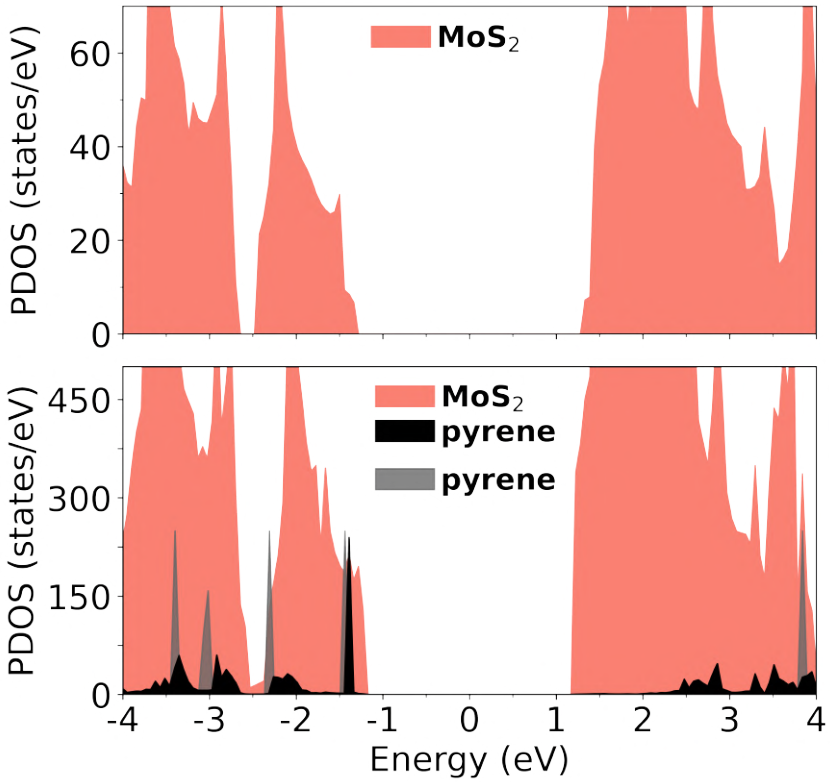

Figure 3.6: Projected density of states (PDOS) in states per eV and unit cell calculated at the G_0W_0 level for pristine MoS_2 (top) and pyrene@MoS_2 (bottom panel). To facilitate comparison, the HOMO of the isolated molecular monolayer (gray) is aligned to that of the molecular monolayer in the heterostructure (black).

is a rather good choice for the MoS_2 side [176], unfortunately, not for the molecular side. The remaining question is: would a hybrid functional as a starting point affect the qualitative behavior of the level alignment? To answer this question, we calculate the electronic properties using HSE [101–103]. The left panel of Fig. 3.7 shows the band structure calculated with HSE. The gap of MoS_2 (pyrene) is 2.1 eV (3.2 eV), *i.e.*, increased by 0.4 eV (0.7 eV) with respect to the PBE value. The HOMO of pyrene appears within the MoS_2 gap, consistent with the PBE case. This observation confirms the type-II level alignment on the DFT level. The HOMO-1 appears at around -1.7 eV, only a difference of -0.2 eV with respect to the PBE value.

We also calculate the QP band structure using the HSE wavefunctions as a starting point. As expected, the HOMO appears at a lower energy than the valence bands of MoS_2, analogous to the G_0W_0@PBE case. At the MoS_2 side, the self-energy correction

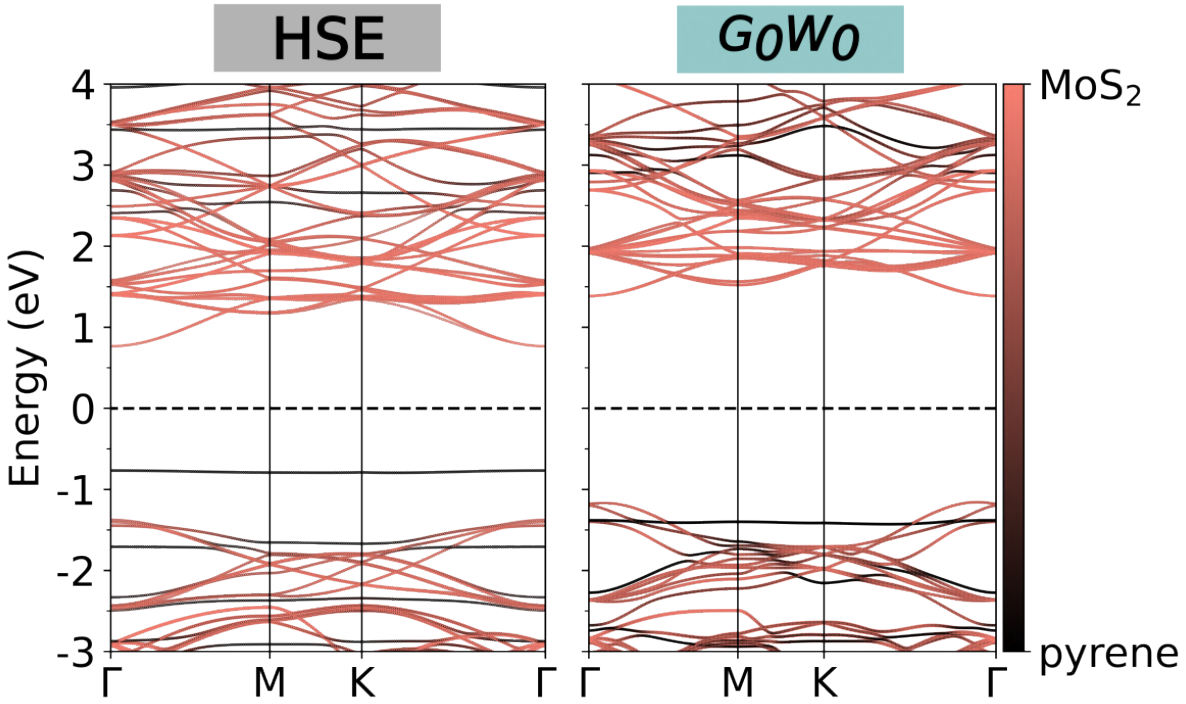

Figure 3.7: Band structures of pyrene@MoS_2, obtained from HSE (left) and G_0W_0 (right). The color code, going from red (MoS_2) to black (molecule) indicates the contributions of the pristine entities to the bands.

increases the gap from 2.1 eV to 2.8 eV, a renormalization of 0.7 eV. At the molecular side, the HOMO-LUMO gap increases from 3.2 eV to 4.3 eV, a change of 1.1 eV. In comparison, the VBM-CBM (HOMO-LUMO) gap is increased by 0.6 eV (1.2 eV) when using PBE as starting point, suggesting that HSE is a better starting point for the molecular crystal. In conclusion, there is no game change when using a hybrid functional as demonstrated by the example of HSE. Overall, the MoS_2 side is less affected by the transition from PBE to HSE, and the increased HOMO-LUMO distance on the molecular side does not lead to a qualitative change in the alignment type. The comparison between the PBE and HSE level alignments is illustrated in Fig. 3.8.

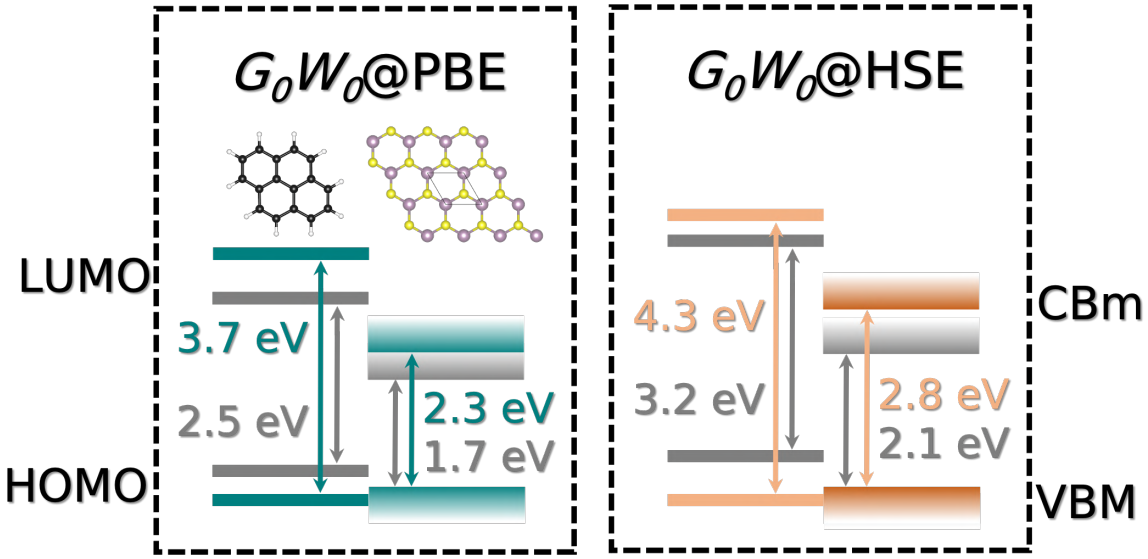

Figure 3.8: Level alignment in pyrene@MoS_2 as obtained by G_0W_0 using PBE (left) and HSE (right) as the starting point. The gray bars indicate the DFT values, the colored bars the resulting quasiparticle levels. In both panels, they are projected onto pyrene at the left side and onto MoS_2 at the right side, and the VBM of MoS_2 obtained from DFT is taken as the reference.

3.3 Optical properties

We calculate the optical properties by solving the BSE on top of the G_0W_0@PBE band structure. In Fig. 3.9 we compare the imaginary part of the frequency-dependent macroscopic dielectric function between pristine MoS_2 (top) and pyrene@MoS_2 (bottom) as obtained by averaging over the in-plane components. For comparison we also show the IQPA that ignores excitonic effects. We focus only on bound excitons, whose energies are located within the QP gap. These features result exclusively from electron-hole interactions and are therefore absent in the IQPA. In pyrene@MoS_2, the lowest-energy exciton originates from MoS_2-derived transitions around the band edges. The corresponding excitonic peak is located at about 2.0 eV, which is 380 meV below its QP gap. Thus, the binding energy of the first exciton, estimated as the difference between the QP gap and the exciton energy, is 70 meV higher in pyrene@MoS_2 than in pristine MoS_2.

We classify the bound excitons according to the predominant layer in which the involved electrons and holes are located. In this system, we mainly study MoS_2-like excitons and charge-transfer excitons (which also have a hybrid nature). Interestingly, we find that both types coexist in the visible region. We proceed by selecting one of each type for further analysis. The MoS_2-like excitons are characterized by the highest

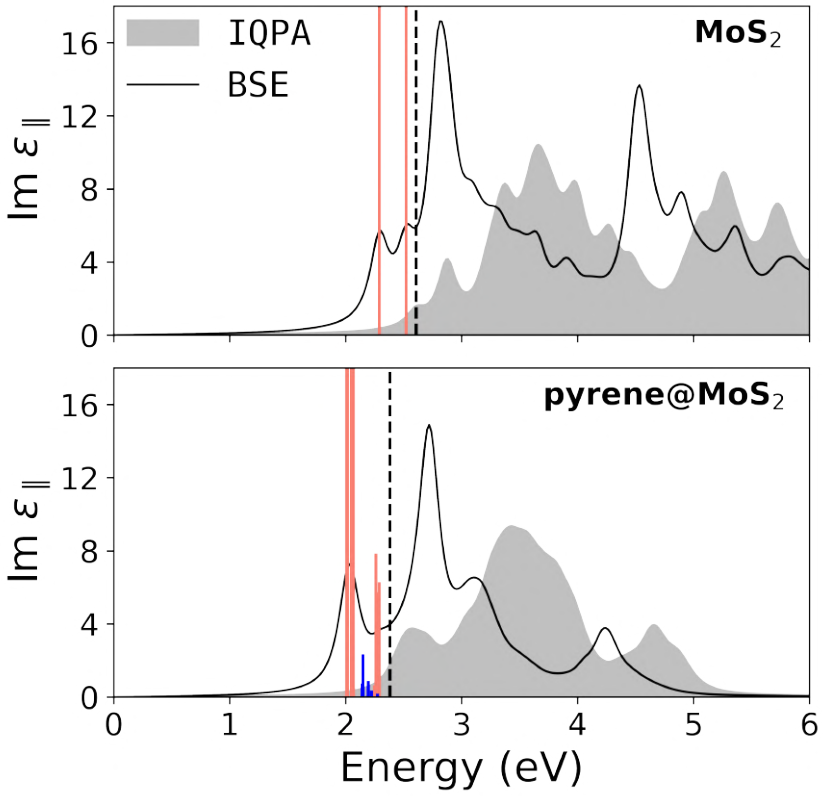

Figure 3.9: Imaginary part of the dielectric function of pristine MoS_2 (top) and pyrene@MoS_2 (bottom), averaged over the in-plane components, including (BSE, solid lines) and neglecting (IQPA, gray areas) excitonic effects. The oscillator strenghts of selected excitations are indicated by red (MoS_2-derived excitons) and blue bars (charge-transfer excitons). The dashed lines mark the positions of the respective QP gap between the VBM and CBM of MoS_2.

oscillator strengths (marked in red in Fig. 3.9). As an example, we show in the top panel of Fig. 3.10 the exciton wave function corresponding to the lowest-energy exciton of the system. The real-space plot shows moderately localized distributions of both the electron (green) and the hole (red) in this e-h pair, indicating a medium-sized exciton binding energy as also mentioned in Section 2.1.5. Fixing the hole near a Mo atom (red dot in the left panel), the electron distribution reflects the Mo d_{z^2} character of the lowest MoS_2 conduction bands.

We will now to describe the second type of bound excitons obtained for this heterostructure. Charge-transfer excitons (marked in blue in Fig. 3.9) are characterized by small oscillator strengths. The chosen representative of this type, located at at an energy of 2.15 eV, has a binding energy of 230 meV. This excitation involves transitions

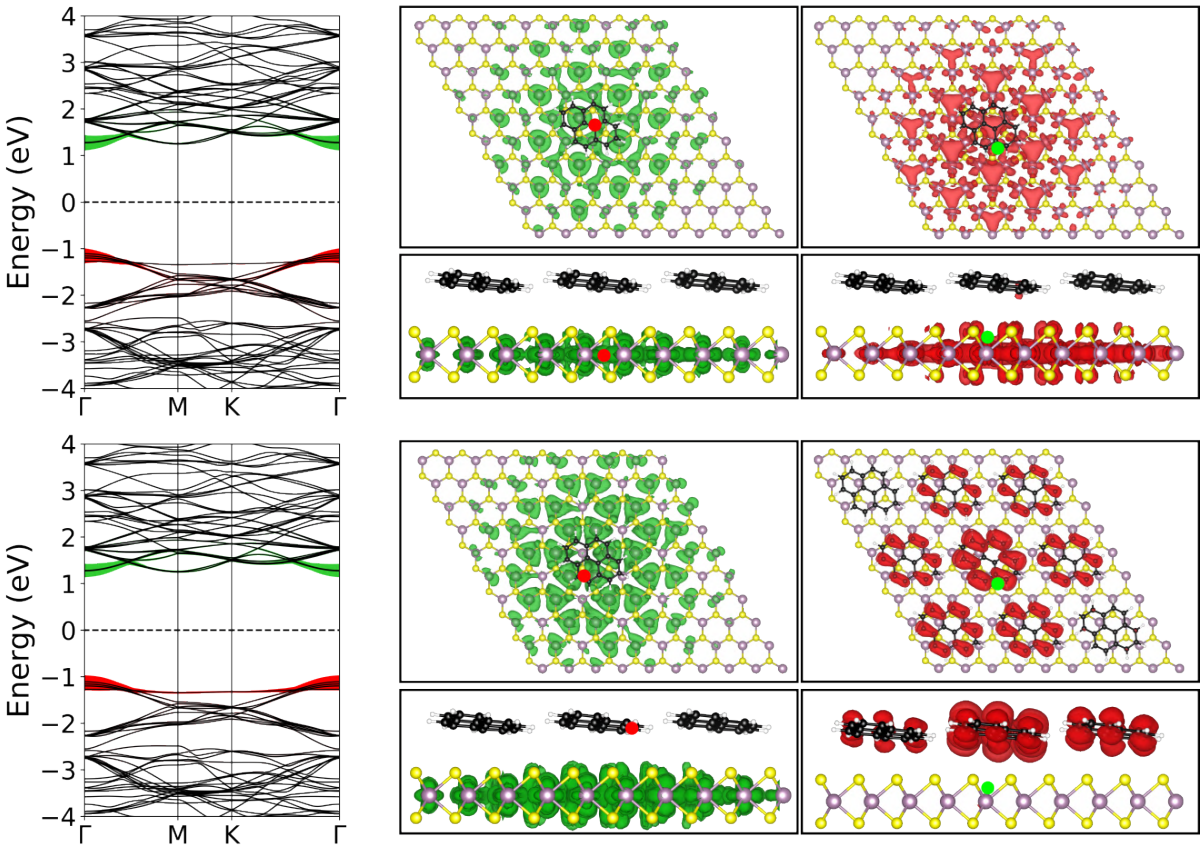

Figure 3.10: Reciprocal and real space representation of an MoS_2-like exciton (top) and a charge-transfer exciton (bottom panels) in pyrene@MoS_2. The contributions of the involved states are indicated in the band structures on the left by red and green circles. Their sizes are proportional to the transition weight (see Eq. (1.30)). The real-space representations, depicted in a 3×3 supercell, show the probability density of finding the hole of the e-h wave function given a fixed position of the electron (left panels) and vice versa (right panels). The electron (hole) probability distribution is depicted in green (red) with the corresponding hole (electron) position marked by the red (green) dots.

between the HOMO of pyrene and the lowest conduction band of MoS_2 as seen from the reciprocal-space analysis on the left in the bottom panel of the figure. The real-space plot shows that the exciton is more delocalized and has a different electronic distribution than the MoS_2 exciton. A similar behavior has been found for charge-transfer excitons in other vdW materials, such as layered h-BN [66, 177]. When the hole is fixed on pyrene, the electron distribution resembles a projection of the molecular π-orbital onto the MoS_2 surface, as shown in Fig. A.1. With the electron position fixed near a Mo atom, the hole distribution reflects the HOMO of pyrene (bottom right panel of Fig. 3.10).

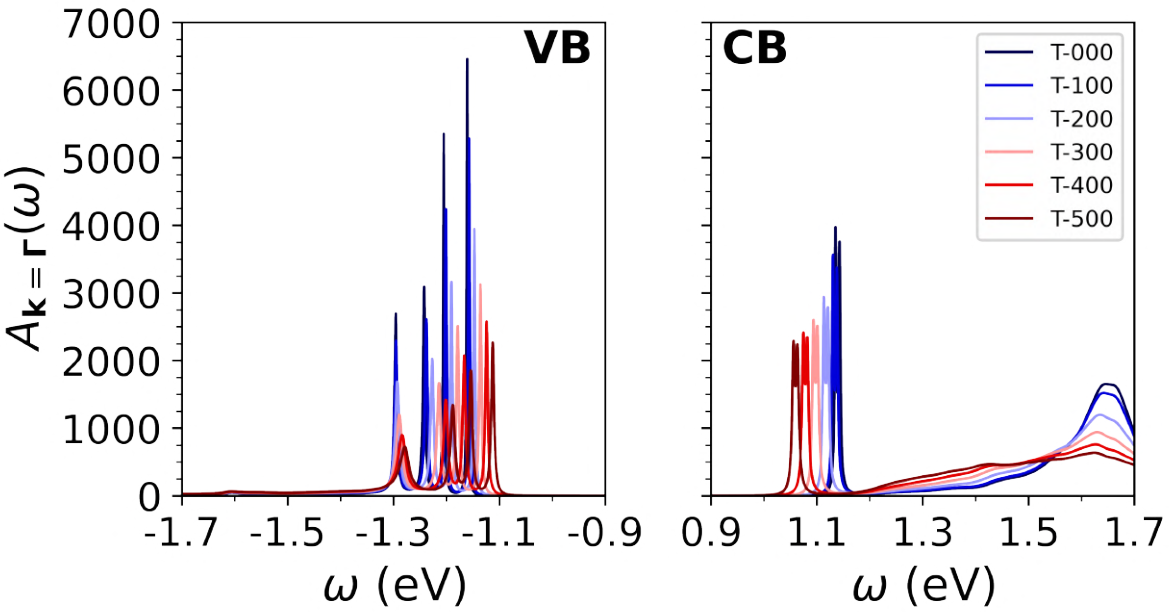

Figure 3.11: Spectral functions of pyrene@MoS_2 for valence and conduction bands at the Γ-point in an energy range from -1.7 eV to 1.7 eV.

3.4 Electron-phonon interaction

We have so far described the electronic properties of pyrene@MoS_2, but without considering vibrational effects. In this section, we present the impact of EPI on the electronic properties of pyrene@MoS_2. As in the case of the MoS_2 monolayer (see Section 2.1.4), the electron-phonon matrix elements (Eq. (1.38)) and the electron-phonon self energy are calculated using the QP eigenvalues obtained from the G_0W_0 approximation.

In Fig. 3.11 we plot the spectral function of the valence and conduction bands at the **Γ**-point for the energy range from -1.7 eV to 1.7 eV and a temperature range from 0K to 500K, in 100K increments. The first three peaks, from right to left in the energy range from -1.3 eV to -1.1 eV, correspond to the three highest valence bands of MoS_2, namely VBM, VB-1, and VB-2. The fourth peak at around -1.3 eV, is assigned to the HOMO of pyrene. Interestingly, the temperature-dependent renormalization of the MoS_2 states is more pronounced than that of the molecular states. The QP peak of the CBM is well recognized at an energy of 1.1 eV, but the higher-energy peaks cannot longer be properly distinguished. Using the spectral function for the band edges, we estimate the ZPR of the band gap to be about -70 meV, a value 10 meV smaller than the value for pristine MoS_2 (Section 2.1.4). The fundamental gap of pyrene@MoS_2, upon renormalization due

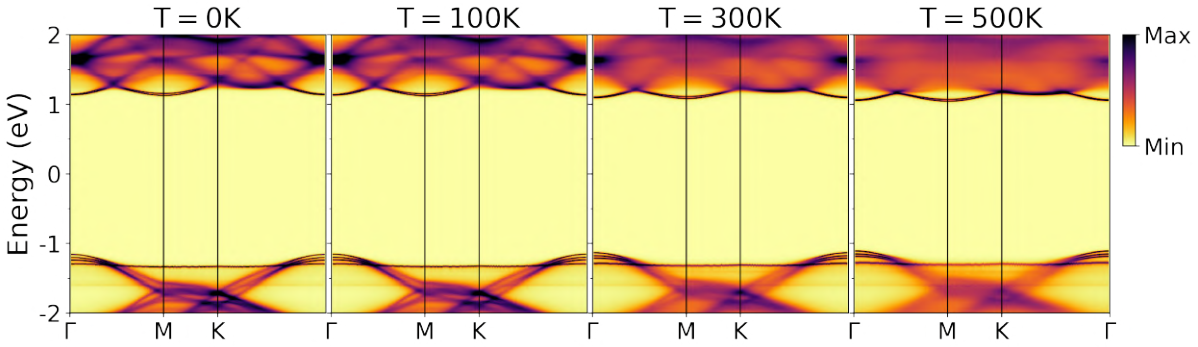

Figure 3.12: Temperature-dependent band structure of pyrene@MoS_2 for temperatures of 0K, 100K, 300K and 500K (from left to right). The color scale bar indicates the maximum (black) and minimum (white) values of the spectral function.

to the G_0W_0 approximation and EPI, amounts to 2.23 eV, a total increase of 0.53 eV with respect to the PBE gap.

We now focus our attention on the low-intensity feature that appears at an energy of -1.6 eV. We notice that there is no band state at this energy in the QP band structure of Fig. 3.4, thus this is an example of a *satellite* [178]. This spectral signature does not increase or decrease in intensity with temperature, as expected from polaronic spectral features. The origin of such satellites is explained by looking at the energy difference between a QP peak and the satellite, which should correspond to a phonon energy of the system. We recall that the largest phonon energy of MoS_2 is approximately 60 meV (see Section 2.1.3), while the vibrational energies of pyrene have a range from 14 meV to 390 meV (see Appendix A.1). The energy difference between the QP peak assigned to the HOMO (around -1.3 eV) and the latter is about 300 meV. The vibrational modes of pyrene, summarized in Table A.1, show that the C-H stretching modes have a similar energy. Therefore, we classify this spectral signature as a *molecular satellite*.

To further investigate this molecular satellite we plot the temperature-dependent band structure for temperatures of 0K, 100K, 300K, and 500K in Fig. 3.12. We immediately observe the band gap renormalization at the $\mathbf{\Gamma}$-point. Moreover, the spectral feature at -1.6 eV, assigned to a molecular satellite, appears along the high-symmetry points of the BZ. Its flat dispersion resembles that of the HOMO, underpinning the molecular origin.

A scientist is happy, not in resting on his attainments but in the steady acquisition of fresh knowledge.

Max Planck

4

Many-body effects in pyridine@MoS_2

In this chapter, we study the electronic and optical properties of pyridine@MoS_2. We use the same framework presented in Chapter 3, starting with the description of the optimized geometry. Then, we compute the QP correction to the PBE band structure. Based on the QP band structure, we calculate the optical properties, classifying the bound excitons found for this heterostructure. Finally, we examine the temperature-dependent band gap and the spectral signatures.

4.1 Geometry optimization

Similar to pyrene@MoS_2, we construct a 3×3×1 supercell and we consider a starting configuration consisting of an upright standing molecule at a vertical distance of about 3 Å, with the nitrogen atom pointing toward the MoS_2 monolayer. The internal coordinates are then relaxed using PBE. Unlike pyrene, where the final geometry is tilted (see Fig. 3.1), pyridine lies parallel to the MoS_2 plane, and the center of the aromatic ring is located above the S atom at an interlayer distance of 3.19 Å from the monolayer, as shown in Fig. 4.1. Like in pyrene@MoS_2 no chemical bonding occurs, and the interaction is predominantly due to vdW forces.

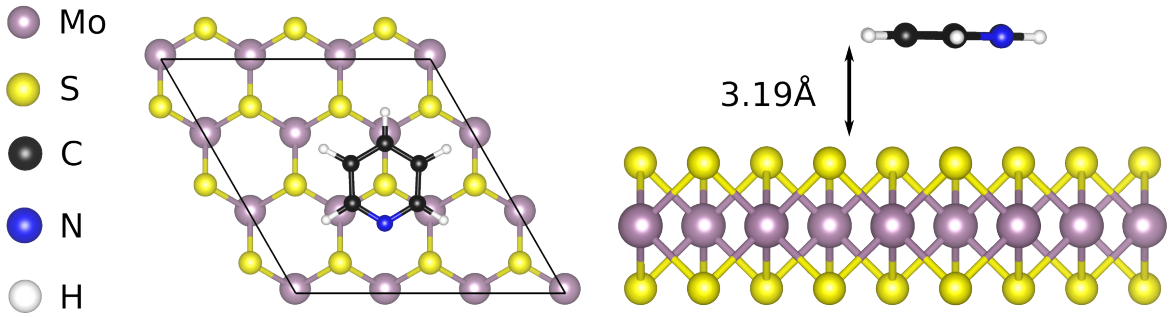

Figure 4.1: Side and top view of the optimized structure of pyridine@MoS_2 in a 3×3×1 MoS_2 supercell.

4.2 Electronic properties

The PBE band structure is shown in the left panel of Fig. 4.2. The material exhibits a direct gap of 1.7 eV at the **Γ**-point, due to the band folding in the 3×3×1 supercell. The HOMO of pyridine and the three upper-most valence bands (VBM, VB-1, and VB-2) of MoS_2 have a similar energy of −0.8 eV at **Γ**. These bands have mixed character as observed for the MoS_2 VB-1/VB-2 states, as depicted in the right panel of Fig. 4.2 (blue circles), which shows the KS wave functions of selected bands at the **Γ**-point. Such a mixed character of the top valence states has also been identified at the hybrid interface pyridine@ZnO [68, 69] and has been attributed to the high electronegativity of nitrogen and the permanent dipole of pyridine. The HOMO of pyridine corresponds to a sp^2 orbital (orange circle), with contributions from carbon and nitrogen [86]; it also shows hybridization with Mo-4d orbitals. We identify another flat band around 1.4 eV, corresponding to the HOMO-1 of pyridine (brown circle), which is a molecular orbital with π character.

PBE yields an energy-level alignment of type II, where the HOMO of the molecular monolayer constitutes the highest occupied valence state, whereas the lowest-lying unoccupied states arise from the conduction band of MoS_2. PBE preserves the band structure of the pristine constituents to a large extent, with a band gap of 1.7 eV on the MoS_2 side. In the left panel of Fig. 4.3, the band structure is plotted along the high-symmetry points in the BZ of the MoS_2 unit cell, after an unfolding procedure. This band structure confirms the type-II level alignment by identifing the HOMO at an energy of −0.8 eV, slightly higher than the top valence band of MoS_2 at the **K** point.

We calculate the plane-averaged charge density difference $\Delta\varrho$ along the vertical direction, as defined in Eq. (3.1). Analogous to the case of pyrene, in the region right above the S-atom the charge density is increased, while it is depleted in the region around the

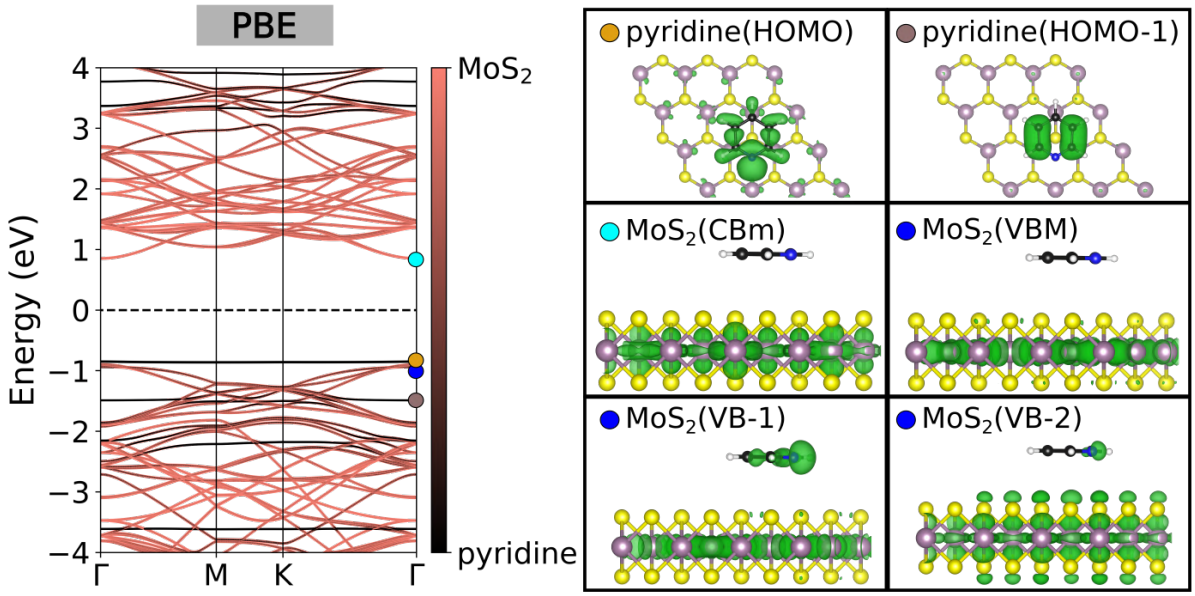

Figure 4.2: Left: Band structure of pyridine@MoS_2 calculated with PBE. The color code, going from red (MoS_2) to black (molecule) indicates the contribution for the pristine entities to the bands. Right: Kohn-Sham (KS) wave functions of selected bands at the **Γ**-point.

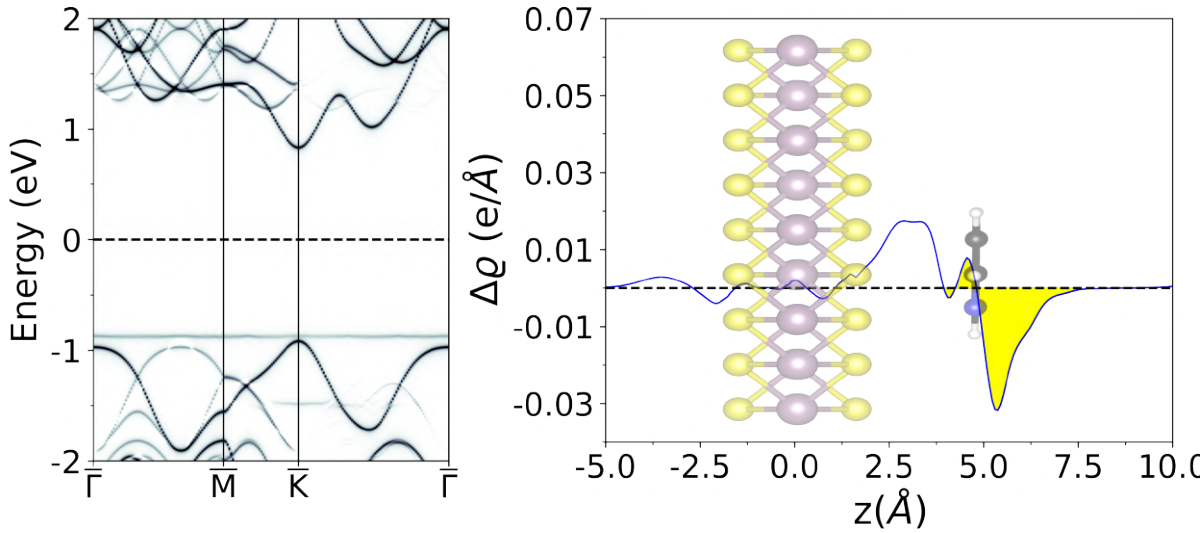

Figure 4.3: Left: PBE band structure of pyridine@MoS_2 plotted along the high-symmetry points in the BZ of the unit cell of MoS_2. Right: Plane-averaged charge density difference along the z-direction. A positive (negative) value of $\Delta\varrho$ represents accumulation (depletion) of charge density.

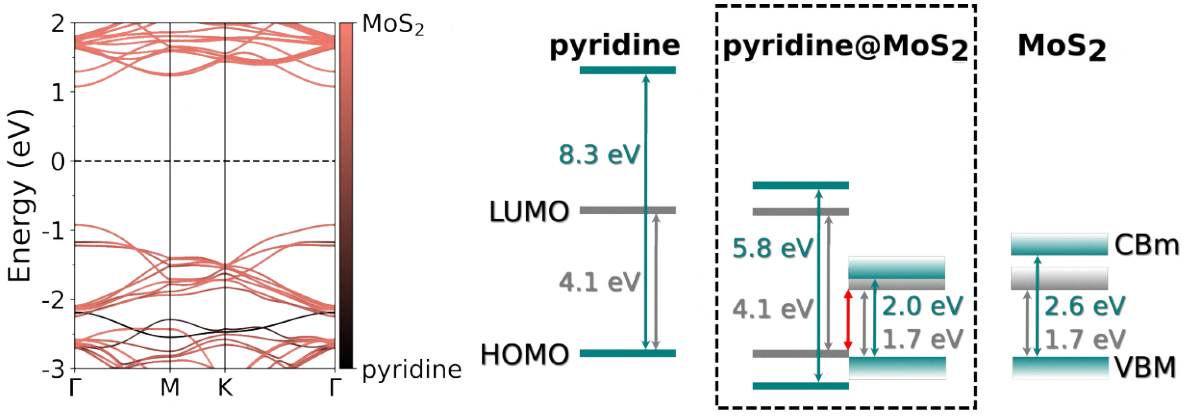

Figure 4.4: Left: Band structure of pyridine@MoS_2 calculated with G_0W_0. The color code, going from red (MoS_2) to black (molecule) indicates the contribution for the pristine entities to the bands. Right: Energy-level alignment obtained from PBE (gray) and G_0W_0 (teal). The middle panel shows the result for the hybrid material, on the left (right) the corresponding scheme is depicted for the molecular monolayer (MoS_2). The red arrow indicates the DFT band gap.

molecule, as shown in the right panel of Fig. 4.3. By integrating over the area in the highlighted region, the amount of redistributed charge is obtained to be -0.05 electrons.

After describing the PBE results of our heterostructure, we calculate the electronic properties using the G_0W_0 approximation and the PBE wavefunctions as starting point. The QP band structure is shown in the left panel of Fig. 4.4. The HOMO-derived band is located deep in the valence-band region and intertwined with the HOMO-1 at an energy below -2 eV. Most important, the many-body effects on the energy levels of both the TMDC and the molecular layer lead to a qualitative change of the level alignment, from type II, obtained with PBE, to type I. To properly describe this change, we plot the level alignment as shown in the right panel of Fig. 4.4. Here, the PBE HOMO/VBM of the isolated systems are aligned to their respective counterparts in the heterostructure. In the latter, the PBE VBM of MoS_2 is taken as the global reference. This means that this level does not appear to be affected by G_0W_0, while all others are aligned with respect to it.

The QP correction increases the gap of MoS_2 by 0.3 eV (from 1.7 to 2.0 eV). This value is not only notably reduced in comparison with the counterpart in pristine MoS_2 (2.6 eV), but even smaller than in the case of pyrene@MoS_2 (2.3 eV). Thus, polarization-induced effects at the MoS_2 side amount as much as -0.6 eV for this heterostructure. At the molecule side, the HOMO-LUMO gap of pyridine in the heterostructure is renormalized by approximately 1.7 eV. However, the corresponding value of the isolated molecular monolayer is much larger, *i.e.*, 4.2 eV. This means that the polarization-induced effect,

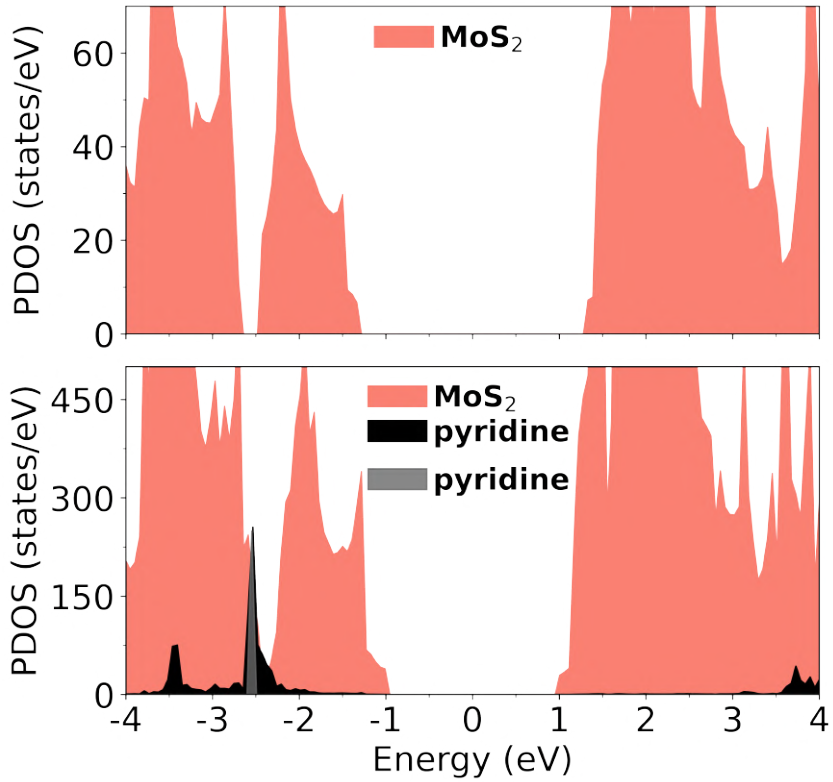

Figure 4.5: Projected density of states (PDOS) in states per eV and unit cell calculated at the G_0W_0 level for pristine MoS_2 (top), and pyridine@MoS_2 (bottom). To facilitate comparison, the HOMO of the isolated molecular monolayer (gray) is aligned to that of the molecule in the heterostructure (black).

due to the presence of the MoS_2 monolayer, reduces the self-energy and thus the gap by about -2.5 eV. Table 4.1 summarizes the values of the self-energy correction for the band edges at the heterostructure and prisitine components.

Table 4.1: Energy renormalization, computed with the G_0W_0 approximation, of the HOMO-LUMO and VBM-CBM distance of the pristine components and the heterostructure. The difference corresponds to the polarization-induced correction due to mutual screening between the components.

Gap/System	Pyridine	MoS_2	Pyridine@MoS_2
HOMO-LUMO (eV)	4.2	–	1.7
VBM-CBM (eV)	–	0.9	0.3

Overall, for the molecules studied so far, pyridine and pyrene, the polarization effects represent a small contribution to the total self-energy correction on the frontier molecular levels. The larger polarization in pyridine@MoS_2, compared to pyrene@MoS_2, is assigned to the permanent molecular dipole as well as the smaller interlayer distance of 3.19 Å. These findings re-emphasize the need for many-body corrections to reliably determine the level alignment of hybrid heterostructures [45]. While type-II band alignment usually favors charge transfer and exciton dissociation, type-I, can also lead to exciton- and energy-transfer processes.

The QP correction is also evident in the DOS displayed in Fig. 4.5 for pristine MoS_2 (top), the isolated molecular monolayer, and pyridine@MoS_2 (both in the bottom panel). The molecular states at -2.5 eV of the pristine pyridine are spread over an energy range from -3 eV to -0.25 eV in the heterostructure, due to the dispersion of the HOMO state observed in the QP band structure. The molecular states of the pristine pyridine monolayer in the conduction region are out of the shown energy range, however, we observe some molecular character of the heterostructure also around 3 eV. This renormalization of the conduction states is due to the polarization-induced effects discussed above. This interplay between various (mutual) effects on the individual components may be used as a tool to tailor the electronic properties. Moreover, all of these features have an important impact on the optical properties of these systems, which will be discussed in the next section.

4.3 Optical properties

In Fig. 4.6, we compare the imaginary part of the frequency-dependent macroscopic dielectric function for pristine MoS_2 (top), and pyridine@MoS_2 (bottom), as obtained by averaging over the in-plane components. The IQPA spectrum that ignores excitonic effects is also shown for comparison. In the following discussion, we focus only on bound excitons. The lowest-energy exciton originates from MoS_2-derived transitions between the VBM and the CBM at the $\mathbf{\Gamma}$-point. This first exciton is located at approximately 1.7 eV, which is 300 meV below the QP gap. The exciton binding energy is thus 10 meV lower in pyridine@MoS_2 than in MoS_2.

We classify the bound excitons in two different categories, which are MoS_2-like excitations and hybrid-like excitations. The former correspond to the same type found in pyrene@MoS_2, characterized for their high oscillator strengths, while the latter originate from hybridized bands. We find that both types of excitons coexist in the visible region. The top panel of Fig. 4.7 shows the exciton wave function of the lowest-energy exciton, which correspond to a MoS_2-like excitation. The real-space plots on the right indicate

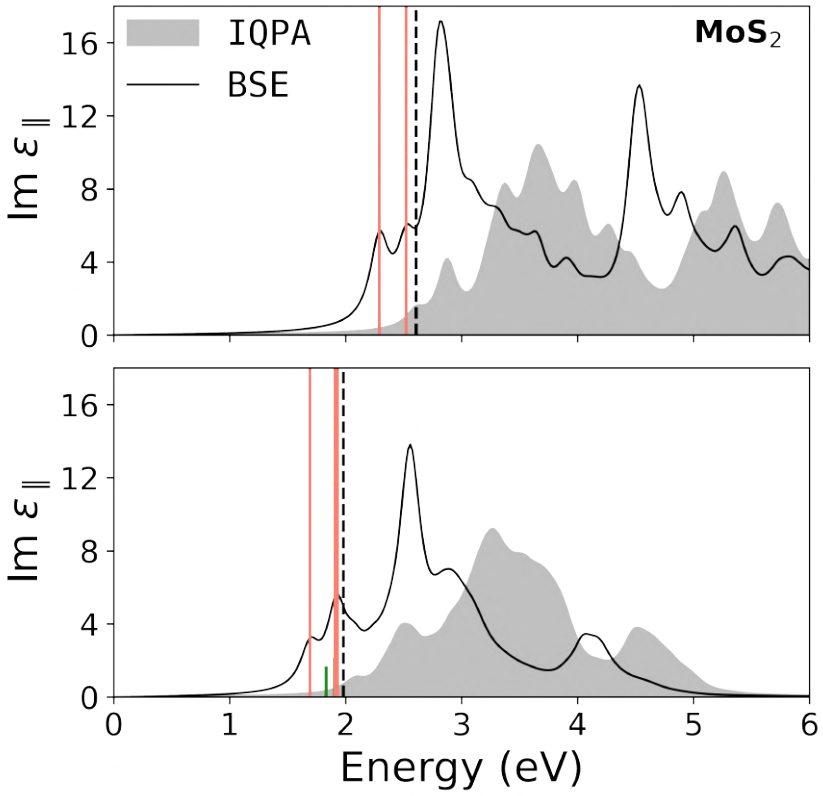

Figure 4.6: Imaginary part of the dielectric function of pristine MoS_2 (top) and pyridine@MoS_2 (bottom), averaged over the in-plane components, including (BSE, solid lines) and neglecting (IQPA, gray areas) excitonic effects. The oscillator strenghts of selected excitons are indicated by red bars (MoS_2-derived excitons) and green bars (hybrid excitons). The dashed lines mark the positions of the respective QP gap between the VBM and CBM of MoS_2.

moderately localized distributions of both the electron (green) and the hole (red) in this e-h pair. Fixing the hole coordinate near a Mo atom (red dot in the left panel), the electron distribution reflects the Mo d_{z^2} orbitals. Moreover, the electron isosurface exhibits the hexagonal distribution characteristic of TMDCs. With the electron fixed near the Mo atom (green dot in the right panel), the mixed Mo-4d and S-3s character of the valence bands becomes apparent. Conspicuously, the hole distribution is different compared to the MoS_2-like exciton of pyrene@MoS_2 (compare the top right panels of Fig. 3.10 and 4.7). This is explained by noting that the valence bands involved in the formation of this exciton are VB-1 and VB-2, unlike the MoS_2 exciton found in pyrene@MoS_2 where the VBM also contributed.

Hybrid-like excitons involve transitions between predominantly hybridized bands and

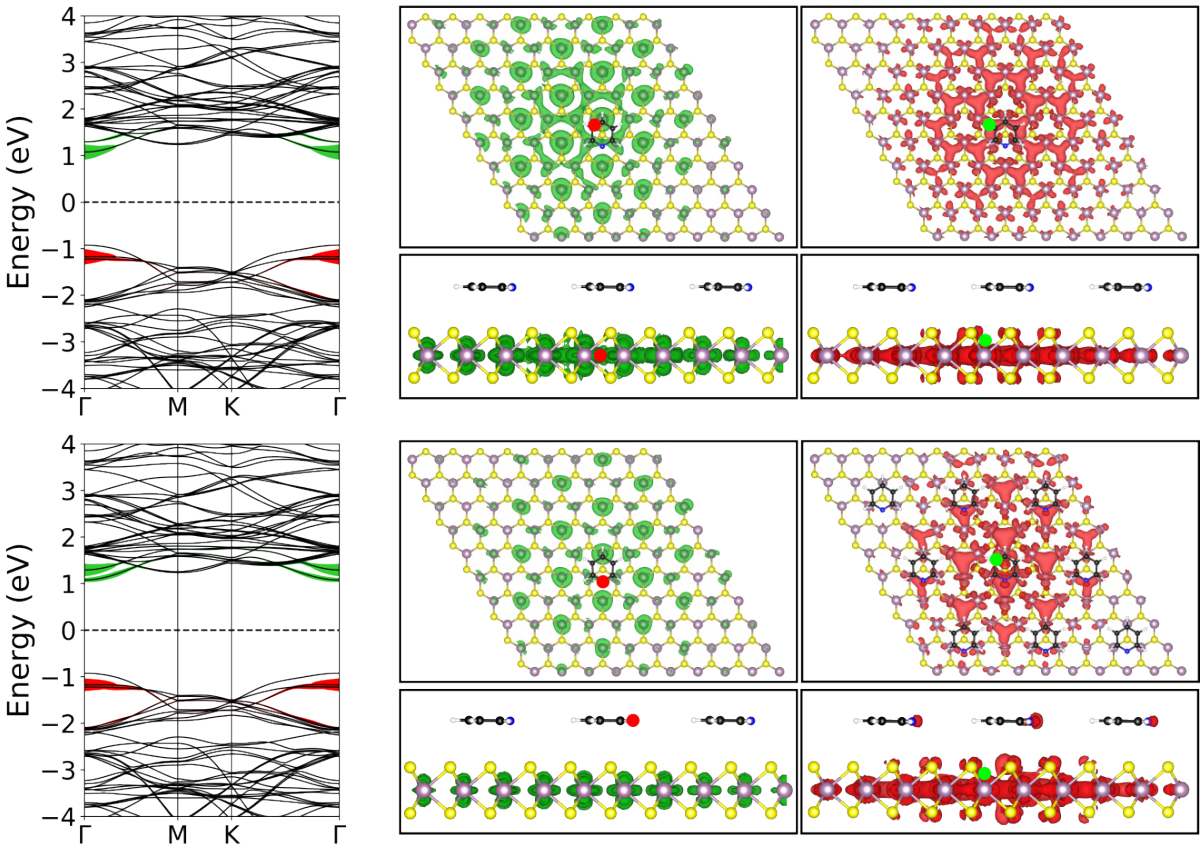

Figure 4.7: Reciprocal and real space representation of an MoS_2-like exciton (top panels) and a hybrid exciton (bottom panels) in pyridine@MoS_2. The band structures on the left indicate the contributions of the involved states as red and green circles. Their sizes are proportional to the transition weight (see Eq. (1.30)). The real-space representations, depicted in a 3×3 supercell show the probability density of finding the hole of the e-h wave function given a fixed position of the electron (left panels) and vice versa (right panels). The electron (hole) probability distribution is depicted in green (red) with the corresponding hole (electron) position marked by the red (green) dots.

are thus typically characterized by small oscillator strengths. As an example of a bound hybrid exciton, we select an excitation (marked in green in Fig. 4.6) with a binding energy of 200 meV at 1.8 eV. The reciprocal-space representation shows the contribution from the hybridized valence bands VB-1 and VB-2 (left bottom panel of Fig. 4.7). The real-space representation shows the electron and hole distributions (right bottom panel of Fig. 4.7) delocalized over the substrate surface. In the hole distribution, we see contributions from both the molecule and the substrate, a major difference from the charge-transfer type studied in the previous chapter. Since the hole is fixed close to the nitrogen atom, a very delocalized electron distribution over the MoS_2 monolayer is found.

4.4 Electron-phonon interaction

As in the previous heterostructure, we compute the electron-phonon quantities using the QP eigenvalues obtained from the G_0W_0 approximation. Figure 4.8 shows the spectral function of the valence and conduction bands at the $\mathbf{\Gamma}$-point within the energy range from -1.6 eV to 1.6 eV and in a temperature range from 0K to 500K, in 100K increments. In the valence region, the first QP peak at an energy of -0.98 eV is assigned to the VBM, while the two peaks at an energy of -1.21 eV and -1.24 eV, are assigned to the VB-1, and VB-2, respectively. In the conduction region, we observe two distinctive QP peaks, one at an energy of approximately 0.96 eV, corresponding to the CBM, and a second peak at an energy of 1.1 eV is attributed to the CB+1. Similar to the results for pyrene@MoS_2 (Section 3.4), higher-energy peaks cannot longer be properly distinguished. Using the spectral function for the band edges, we estimate the ZPR of the band gap to be about -60 meV, the same value calculated for prisitine MoS_2, and 10 meV larger than pyrene@MoS_2. The influence of pyridine in the temperature-dependent renormalization of the band gap is therefore minimal, which could be explained by the smaller surface coverage compared to pyrene. The fundamental gap of pyridine@MoS_2, after the renormalization of the eigenvalues by the G_0W_0 approximation and the EPI, amounts to 1.94 eV, a total increase of 0.24 eV with respect to the PBE gap.

We focus our attention on two low-intensity features that appear at energies of -1.30 eV and -1.36 eV, which we label S_1 and S_2, respectively (see inset of Fig. 4.8). We note that there are no band states at these specific energies in the QP band structure of Fig. 4.4. Consequently, these peaks are designated as *satellites*. We now discuss possible explanations for the origin of these satellites. We recall that the largest phonon energy of MoS_2 is approximately 60 meV, while the vibrational energies of pyridine have a range from 56 meV to 420 meV (see Table A.2 in Appendix A). The energy difference between the VB-2 and S_1 peaks would correspond to an energy of 60 meV, which is consistent with the hypothesis of a MoS_2 origin. However, this possibility is disregarded due to the absence of a comparable feature observed in the analysis of the EPI on the MoS_2 monolayer (see Section 2.1.4). We then explore two possible explanations considering the vibrational energies of pyridine. In the event that the QP peak involved corresponds to VB-1, the energy difference with S_1 and S_2 is 90 meV and 150 meV, respectively. Accordingly, the responsible vibrational modes would be the out-of-plane ring bend (mode 5 or 6) and the C-H pendulum (mode 15). Assuming that VB-2 is responsible for the spectral signature, the energy differences are 60 meV and 120 meV, respectively. The modes with similar energies include the out-of-plane ring bend and the out-of-plane C-H types. The second explanation would be more substantiated, as the out-of-plane vibrations should

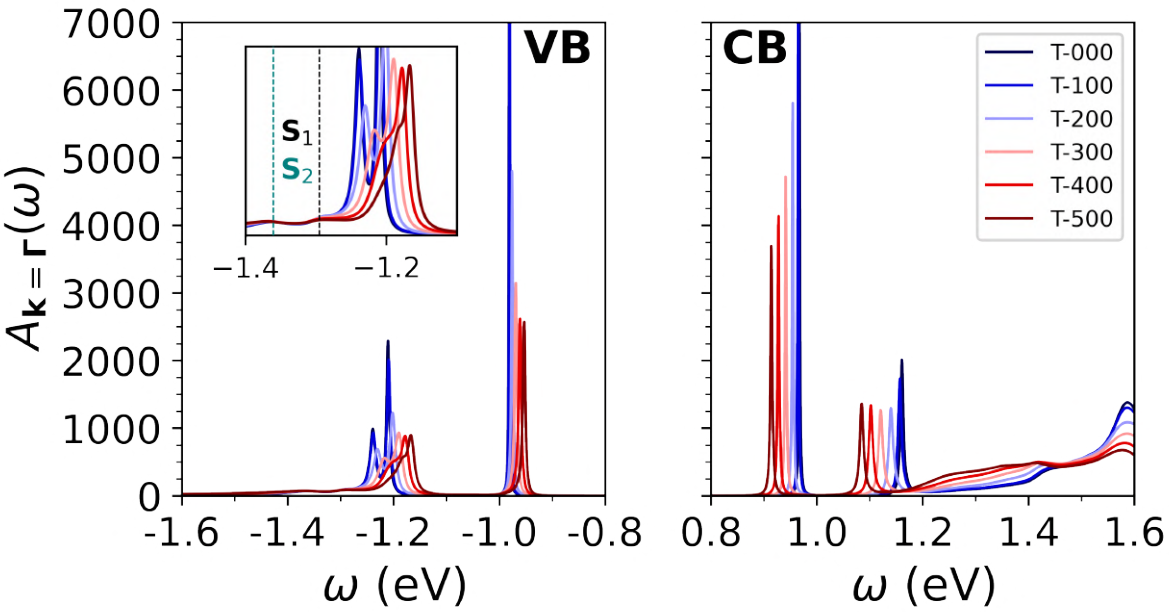

Figure 4.8: Spectral functions of pyridine@MoS_2 for valence and conduction bands at the Γ-point in an energy range from -1.6 eV to 1.6 eV.

exert a more substantial influence on the MoS_2 monolayer.

Nothing in life is to be feared, it is only to be understood. Now is the time to understand more, so that we may fear less.

Marie Curie

5

Hybrid excitations in PTCDA@WSe_2

In this chapter, we study the electronic and optical properties of PTCDA@WSe_2. We systematically investigate the electronic and optical properties, using the same framework as for the previous heterostructures. We begin with the description of the optimized geometry, then we calculate the QP band structure using the G_0W_0 approximation. From these results, we rationalize the level alignment. Finally, we solve the BSE to obtain the optical properties.

5.1 Geometry optimization

We construct a 4×4×1 supercell of the pristine WSe_2 structure (see Chapter 2), *i.e.*, containing 16 W and 32 Se atoms. We consider a starting configuration of a parallel molecule at a vertical distance of about 3 Å with respect to the WSe_2 monolayer. The atomic positions are then relaxed using PBE+TS. The adsorption geometry of PTCDA is tilted with the shortest (longest) distance between the WSe_2 monolayer and the physisorbed molecules is 4.98 Å (2.87 Å), measured from the topmost atomic position of the substrate. The inclination is attributed to the weak interactions between neighboring molecules. Identically to the previous heterostructures, the interactions between molecule and substrate is primarily due to vdW forces. The side and top views of the optimized supercell are shown in Fig. 5.1.

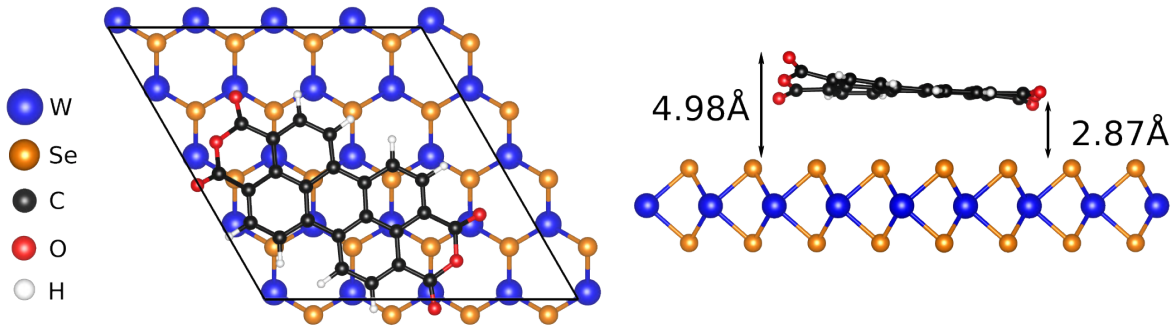

Figure 5.1: Side and top view of the optimized structure of PTCDA@WSe_2 in a 4×4×1 WSe_2 supercell.

5.2 Electronic properties

The PBE band structure is shown in the left panel of Fig. 5.2. The fundamental gap in this material corresponds to the direct gap at the **K** point and amounts to 1.2 eV. Unlike the previous heterostructures, the direct gap at the **K** point is obtained, since for this supercell there is no exact band folding of the **K** point into **Γ**. The WSe_2 band gap in this heterostructure is 1.6 eV, which coincides with the band gap of pristine WSe_2 (see Chapter 2). Visualization of the KS orbitals at the **K** point for the VBM (blue circle) and CBM (light blue circle) of WSe_2 reveals a well defined WSe_2 character, preserving the composition of d and p orbitals (right panel of Fig. 5.2). The adsorption of PTCDA is manifested by the flat band around −0.9 eV in the valence region. A second flat band is observed at an energy of 0.6 eV, now in the conduction region and within the WSe_2 band gap. Visualization of the KS orbitals at the **K** point (right panel of Fig. 5.2) reveals that the flat band in the valence region (pink circle) corresponds to the HOMO of PTCDA, while the mid-gap state (brown circle) corresponds to the LUMO. Overall, PBE preserves the band structure of the pristine constituents and yields an energy-level alignment of type II, with the distinction that the LUMO constitutes the lowest unoccupied conduction state, whereas the highest-lying occupied bands arise from the valence bands of WSe_2.

We perform a band unfolding procedure to confirm the type-II level alignment. The PBE band structure is plotted along the high-symmetry points in the BZ of the WSe_2 unit cell, as displayed in the left panel of Fig. 5.3. The WSe_2 gap of 1.6 eV is confirmed, while the HOMO is observed at a lower energy than the VBM of WSe_2, with an energy difference of 50 meV. The LUMO is also clearly observed as a mid-gap state, confirming the preservation of the band structures of the pristine constituents, and the derived type-II level alignment. We calculate the plane-averaged charge density difference $\Delta\varrho$ along

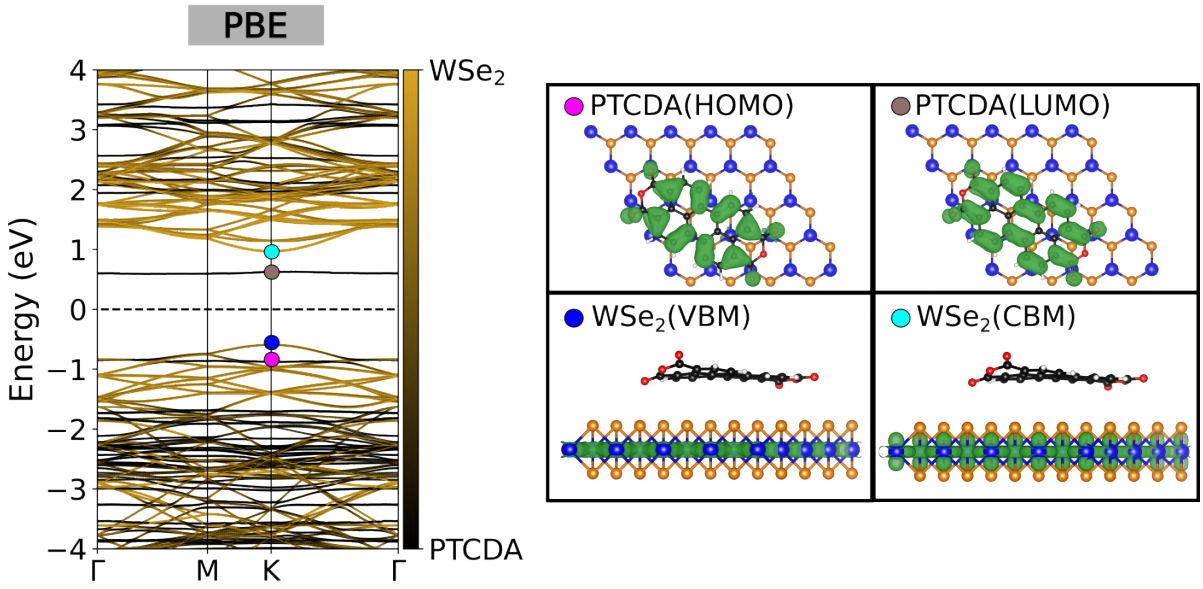

Figure 5.2: Left: Band structure of PTCDA@WSe_2 calculated with PBE. The color code, going from yellow (WSe_2) to black (molecule) indicates the contribution for the pristine entities to the bands. Right: Kohn-Sham (KS) wave functions of selected bands at the **K**-point.

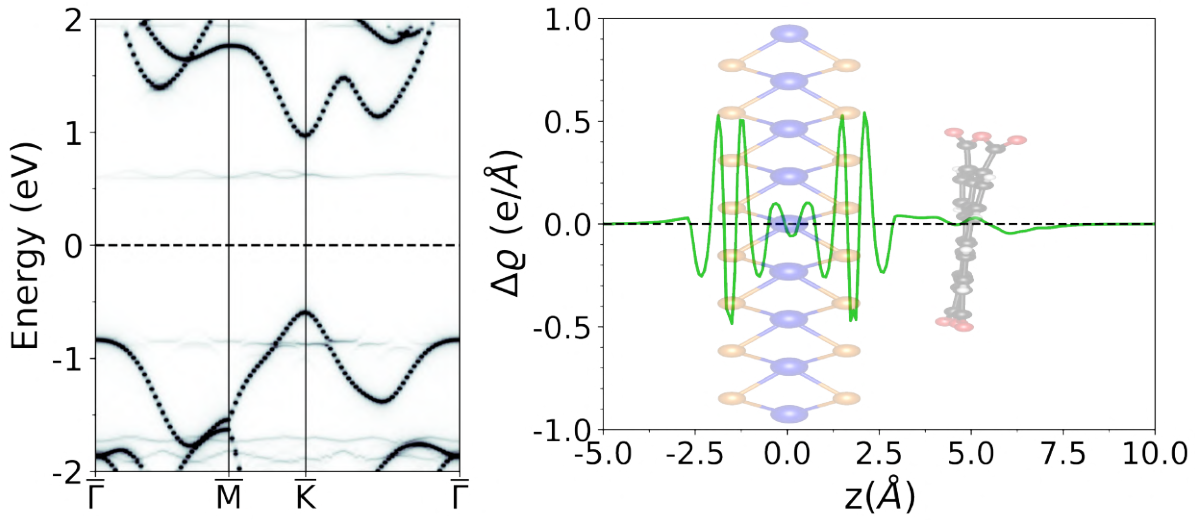

Figure 5.3: Left: PBE band structure of PTCDA@WSe_2 plotted along the high-symmetry points in the BZ of the unit cell of WSe_2. Right: Plane-averaged charge density difference along the z-direction. A positive (negative) value of $\Delta\varrho$ represents accumulation (depletion) of charge density.

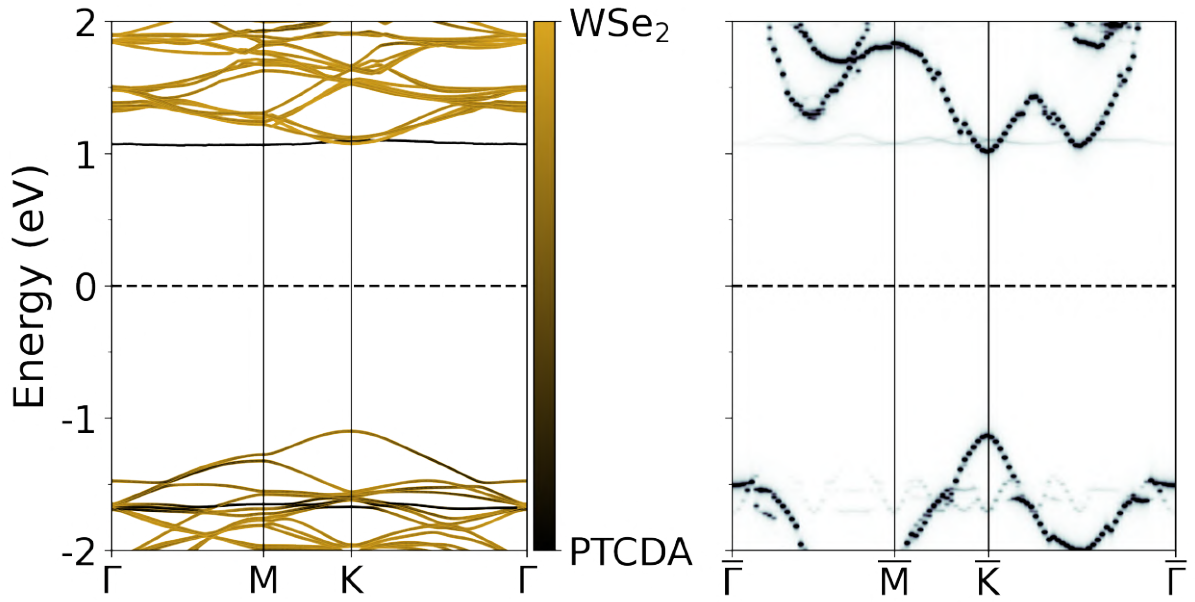

Figure 5.4: QP band structure of PTCDA@WSe_2, computed, using the G_0W_0 approximation, plotted along the high-symmetry points in the BZ of the supercell (left) and the unit cell (right) of WSe_2.

the vertical direction, as defined in Eq. (3.1). In contrast to the previous heterostructures, which have a donor character, the oscillations of $\Delta\varrho$ are found at the WSe_2 monolayer, more specifically, at the position of the Se atoms, hinting an acceptor nature of PTCDA. This could be explained owing to the electron-withdrawing properties of the anhydride groups (C-O).

After describing the PBE results of our system, we calculate the QP band structure using the G_0W_0 approximation on top of the PBE eigenvalues. The QP band structure is plotted in Fig. 5.4 along the high-symmetry points in the BZ of the supercell (left) and unit cell (right) of WSe_2. The LUMO of PTCDA is now located above the CBM of WSe_2 at an energy of 1.1 eV, indicating a qualitatively change of the level alignment, from type II to type I. This energy alignment is consistent with reported scanning tunneling spectroscopy (STS) experiments [65, 169].

To properly discussed this change, we plot the level alignment as shown in Fig. 5.5. Here, the PBE HOMO/VBM of the isolated systems are aligned to their respective counterparts in the heterostructure. In the latter, the PBE VBM of WSe_2 is taken as the global reference. This means that this level is not affected by G_0W_0 while all others are aligned with respect to it.

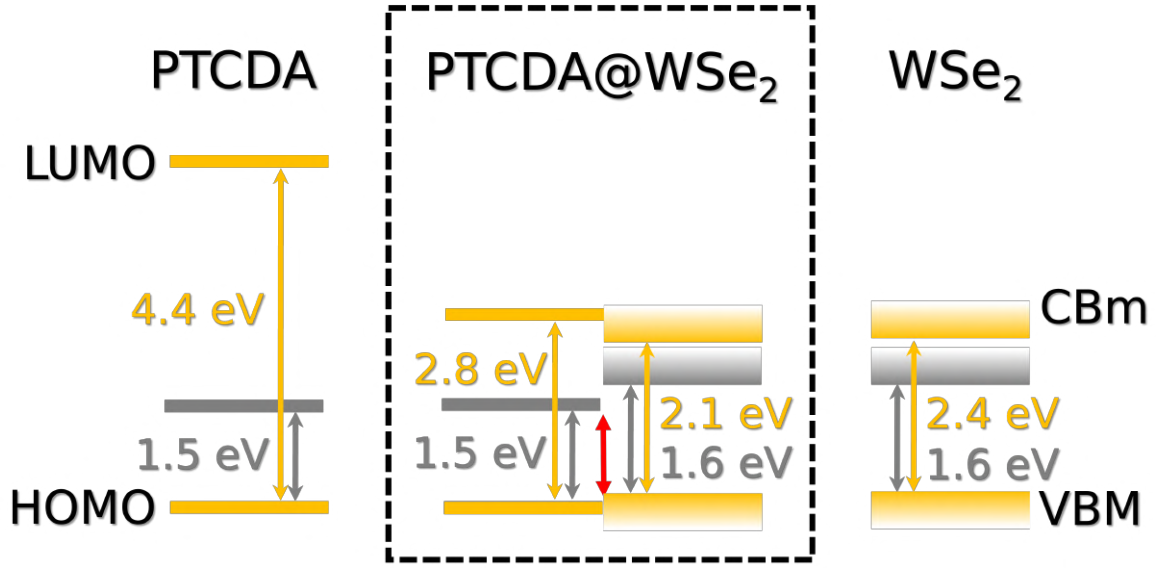

Figure 5.5: Energy-level alignment obtained from PBE (gray) and G_0W_0 (gold) for PTCDA@WSe2. The middle panels show the respective hybrid material, on the left (right) the corresponding scheme is depicted for the molecular monolayer (WSe_2). The red arrow indicates the band gap as obtained from DFT.

Table 5.1: Energy renormalization, computed with the G_0W_0 approximation, of the HOMO-LUMO and VBM-CBM distance for the pristine components and the heterostructure. The difference corresponds to the polarization-induced correction due to mutual screening between the components.

Gap/System	PTCDA	WSe_2	PTCDA@WSe_2
HOMO-LUMO (eV)	2.9	–	1.3
VBM-CBM (eV)	–	0.8	0.5

The QP correction increases the gap of WSe_2 by 0.5 eV (from 1.6 eV to 2.1 eV). However, this gap is smaller than that of pristine WSe_2, where the QP gap amounts to 2.4 eV. At the molecule side, the HOMO-LUMO gap of PTCDA increases by 1.3 eV, again a value much smaller than that obtained in the pristine case, where the gap is increased by 2.9 eV. This means that the polarization-induced effects reduces the self-energy by about -0.3 eV in the WSe_2 side, while -1.6 eV in the molecule side. Table 5.1 summarizes the values of the self-energy correction for the band edges at the heterostructure and pristine components.

We conclude this section by noting that the qualitatively change of the level alignment from type II to type I at the G_0W_0 level has been obtained irrespectively of which

molecular orbital is renormalized. In the previous heterostructures, the HOMO appeared as a mid-gap state between the band gap of MoS_2, while in PTCDA@WSe_2 the LUMO had that role. Regardless, the G_0W_0 approximation predicts a type I alignment for all the HIOS considered in this work.

5.3 Optical properties

In Fig. 5.6, we compare the imaginary part of the frequency-dependent macroscopic dielectric function for pristine WSe_2 (top), and PTCDA@WSe_2 (bottom), as obtained by averaging over the in-plane components. The IQPA spectrum that ignores excitonic effects is also shown for the heterostructure. As in the previous heterostructures, we focus only on bound excitons. The lowest-energy exciton has an energy of 1.72 eV, which corresponds to a binding energy of 430 meV, a very similar value as in WSe_2 monolayer (428 meV). However, the smaller oscillator strength suggest a different type of exciton. The second exciton at an energy of 1.74 eV, has a larger oscillator strength and a binding energy of 408 meV.

We further analyze these excitons by plotting them in both reciprocal and real space representation, as shown in Fig. 5.7. The first exciton corresponds to a charge-transfer exciton, where the excited electron component derives its wavefunction from the LUMO of PTCDA, while the hole component has contributions from the WSe_2 top valence band and the HOMO of PTCDA (bottom of Fig. 5.7). The second exciton is of full WSe_2 intralayer character and derives its wave function purely from WSe_2 bottom conduction and top valence band Bloch states (top of Fig. 5.7). After analyzing them we conclude the two types of excitons that can be found at this interface, WSe_2-like, and charge-transfer, similar to pyrene@MoS_2. However, for this heterostructure the BSE calculations imply that the hybridization of intralayer HOMO $\rightarrow$ LUMO and interlayer VBM $\rightarrow$ LUMO transitions lead to the formation of an energetically favorable hybrid exciton with multi-orbital contributions, which is not present in the previous heterostructures.

Having access to the excitonic wavefunction contributions of the WSe_2 states and the PTCDA orbitals, we evaluate the real-space Frenkel- and/or Wannier-character of the charge-transfer exciton. Specifically, we aim to characterize the exciton's relative electron-hole distance parallel and perpendicular to the heterostructure. To achieve this goal, we analyze the exciton's electron-hole correlation function by using the definition of Ref. [179],

$$F^{\lambda}(\mathbf{r}) = \int_{\Omega} \mathrm{d}^3\mathbf{r}_e \, |\Phi_{\lambda}(\mathbf{r}_h = \mathbf{r}_e + \mathbf{r}, \mathbf{r}_e)|^2 \,, \tag{5.1}$$

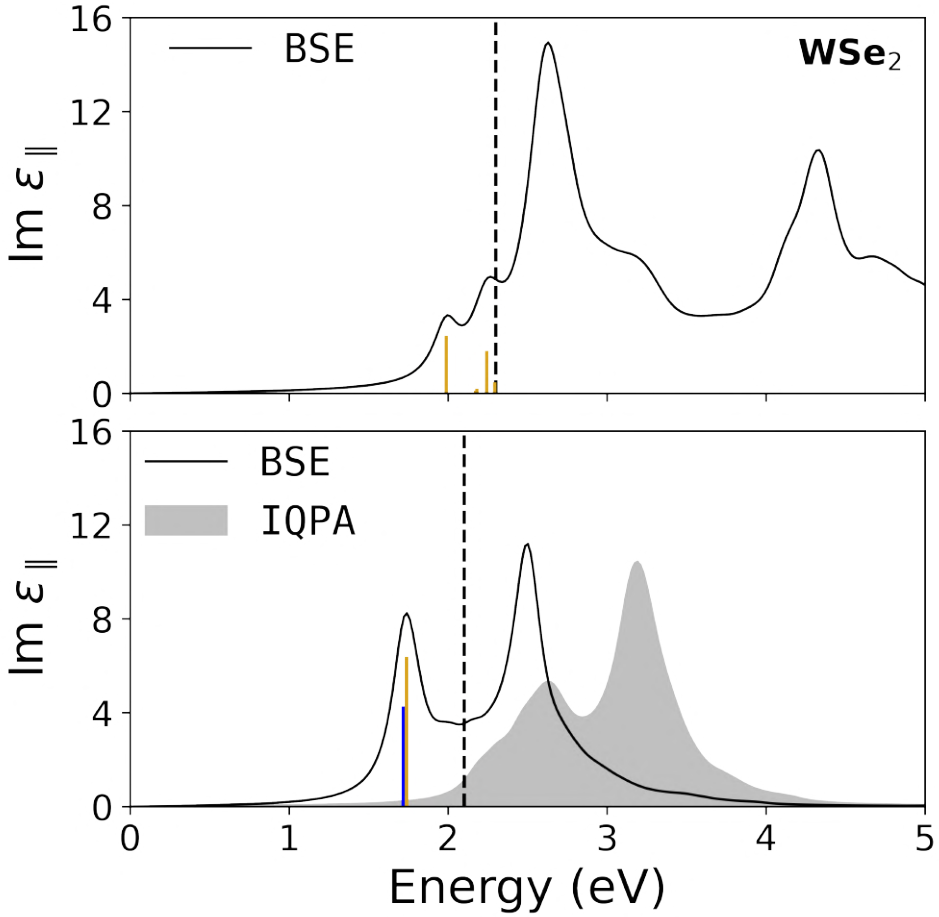

Figure 5.6: Imaginary part of the dielectric function of pristine WSe_2 (top) and PTCDA@WSe_2 (bottom), averaged over the in-plane components, including (BSE, solid lines) and neglecting (IQPA, gray areas) excitonic effects. The oscillator strenghts are indicated by gold bars (WSe_2-derived excitons) and blue bars (charge-transfer excitons). The dashed lines mark the positions of the respective QP gap between the VBM and CBM of MoS_2.

where Φ_λ is the excitonic wave function from Eq. (1.29) and F^λ describes the probability of finding electron and hole separated by the vector $\mathbf{r} = \mathbf{r}_h - \mathbf{r}_e$. We approximate this integral by a discrete sum over a finite number of fixed electron coordinates. For each electron position, the hole probability $|\Phi^\lambda(\mathbf{r}_h = \mathbf{r}_e + \mathbf{r}, \mathbf{r}_e)|^2$ is computed on an evenly spaced, dense grid of 100×100×100 sampling points, covering approximately 9×9×1 of the pristine WSe_2 unit cell. For the WSe_2-exciton, we sample 16 positions close to the W atoms where we expect a high probability of finding the electron. For the charge-transfer exciton, we sampled 60 positions on the PTCDA molecule (0.5 $Å^{-1}$ below and above the

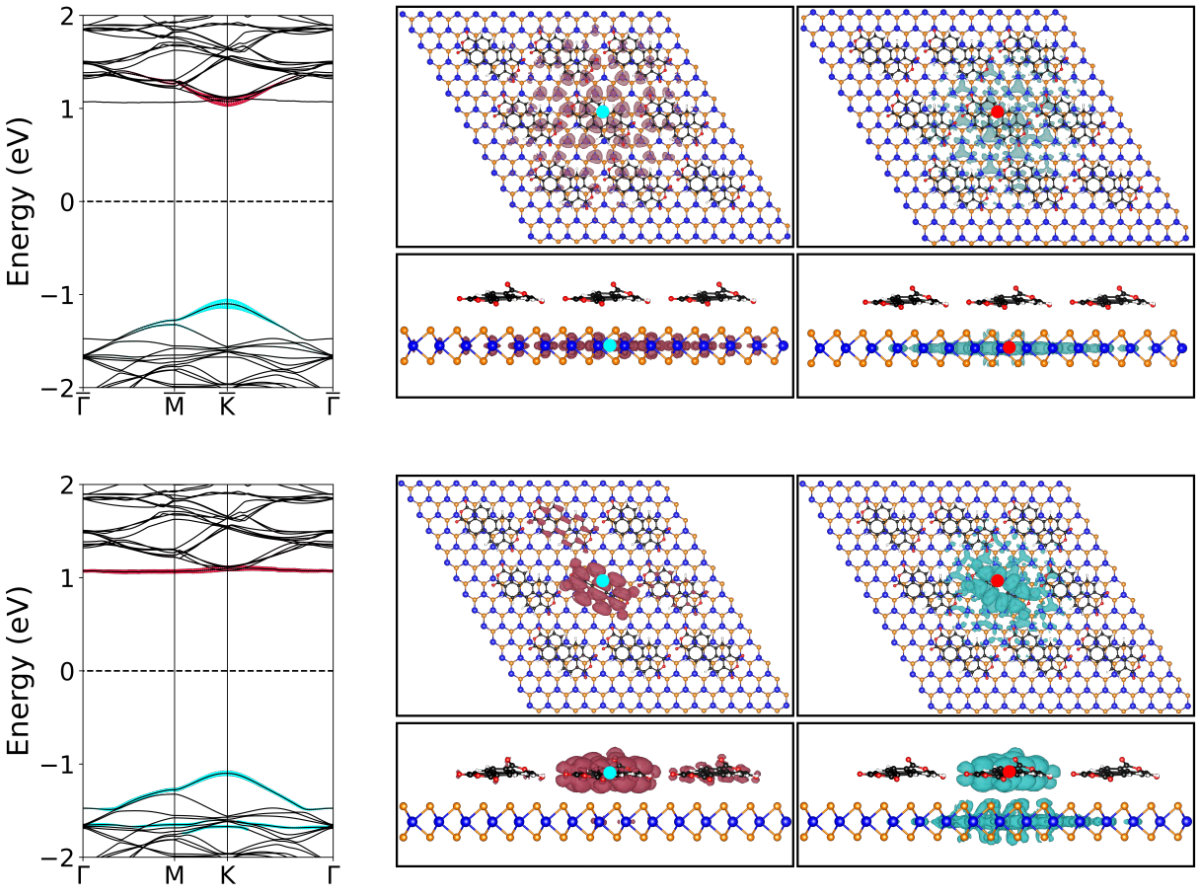

Figure 5.7: Reciprocal and real space representation of a WSe_2-like exciton (top) and charge-transfer exciton (bottom panels) in PTCDA@WSe_2. The band structures on the left indicate the contributions of the involved states as cyan and red circles. Their sizes are proportional to the transition weight. The real-space representations, depicted in a 3×3 supercell show the probability density of finding the hole of the e-h wave function given a fixed position of the electron (left panels) and vice versa (right panels). The electron (hole) probability distribution is depicted in red (cyan) with the corresponding hole (electron) position marked by the cyan (red) dots.

carbon and oxygen atoms) since its electronic contribution is almost entirely comprised of the LUMO of PTCDA.

We split the correlation function into its in-plane and out-of-plane components, as shown in Fig. 5.8. We begin by describing the results for the WSe_2 exciton (left panel of Fig. 5.8). The out-of-plane correlation function is dominated by a single peaked feature centered around 0 Å. Next to the dominant peak two side peaks are present at a separation that matches the distance between the tungsten and selenium planes of the WSe_2 monolayer. Consequentially, the probability density to find WSe_2-excitons in

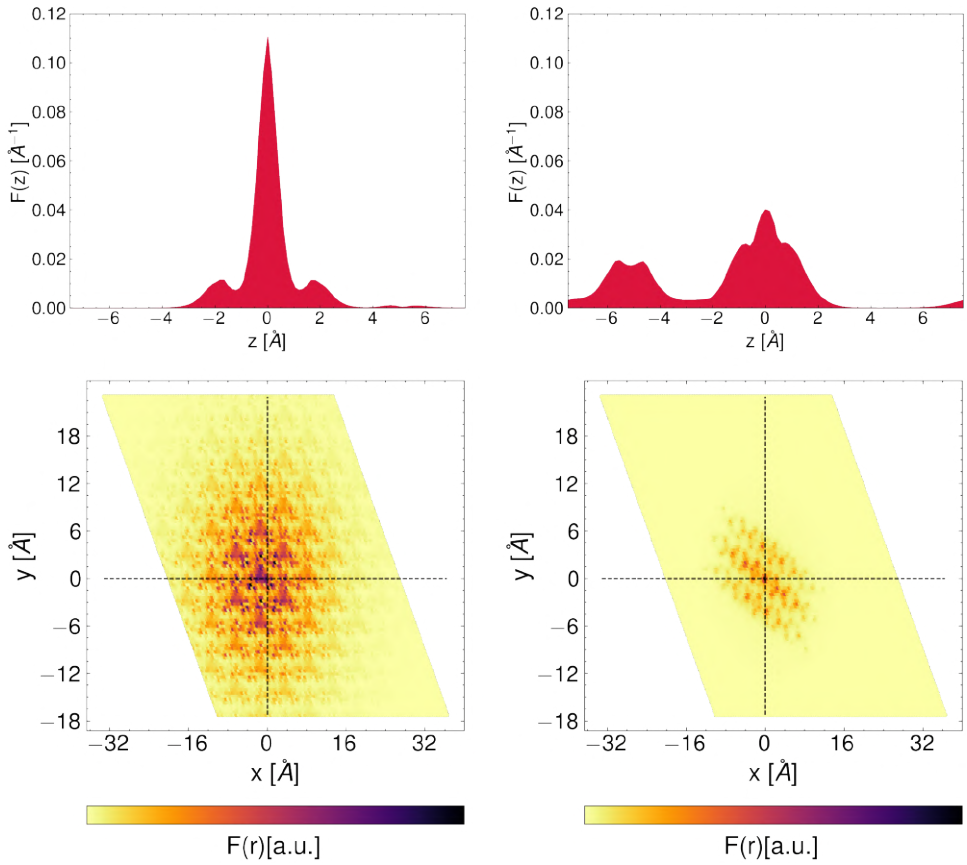

Figure 5.8: The relative out-of-plane and in-plane components of the electron-hole correlation function for the WSe_2 exciton (left panel) and the charge-transfer exciton (right panel).

the WSe_2 layer is nearly 100%. The in-plane correlation function of the WSe_2-exciton resembles the hexagonal distribution observed in the real space plots, as well as, the moderate localization of the wave function. Indeed, since the WSe_2 wavefunction is purely localized in the WSe_2 layer, the exciton is of true Wannier-type. For either fixing the hole or the electron in the WSe_2 layer, the corresponding electron and hole is localized in the inorganic layer, and extends over multiple WSe_2 unit cells.

For the charge-transfer exciton (right panel of Fig. 5.8), the out-of-plane correlation function shows not only a peak around 0 Å, but also a peak centered at −5 Å, which highlights that the wavefunction has contributions from both the organic and inorganic layers. The in-plane correlation function resembles the LUMO of PTCDA, suggesting that both electron and hole components are confined to a single molecule. We found that when the hole is placed on the PTCDA molecule, as shown in Fig. 5.7, the electron is

almost completely localized on the same molecule. In other words, the isosurface now describes a Frenkel-type exciton. When the electron is fixed on the PTCDA layer, the hole isosurface includes a localized part on the same PTCDA molecule, but also a weaker delocalized contribution on the WSe_2 layer. Hence, the hole isosurface has a Wannier and a Frenkel character. This hybrid intra- and interlayer and hybrid Frenkel- and Wannier-nature of the charge-transfer exciton is a unique feature of HIOS that highlights the versatility of these combined platforms for controlling optoelectronic energy conversion pathways.

We conclude by highlighting that while in pure TMDCs heterostructures charge and energy transfers across the interface is mediated and explained by band structure hybridization [180–182], the general preconception for HIOS, like the ones studied in this thesis, is that orbital hybridization is weak [7, 54]. The latter is confirmed by plotting the KS orbitals. In consequence, the formation of the charge-transfer exciton cannot be mediated by hybridized states between the layers. Instead, we conclude that energy transfer must be mediated by dipole-dipole interactions, *i.e.*, in a Förster-type energy transfer process (FRET) [44].

Physics has a history of synthesizing many phenomena into a few theories.

Richard P. Feynman

6 Expansion and addition screening

In this chapter, we extend the *expansion & addition screening* (EAS) method to the so-called mixed-product basis used in excited-state calculations based on the (linearized) augmented planewave (L)APW method [108]. We derive the formalism and implement it within the G_0W_0 module of the **exciting** code [83, 93]. Furthermore, we implement an analogous method for the BSE framework [111]. These developments allow for the calculation of the electronic structure as well as of the optical absorption spectra of large interfaces with high accuracy at low computational cost.

6.1 Background

The dielectric function ϵ, Eq. (1.56), is a central quantity for both *GW* and BSE calculations. In developing this method, we focus on the polarizability, which is typically expanded into a set of basis functions $\{\chi_i\}$ according to

$$P(\mathbf{r},\mathbf{r}',\omega) = \sum_{\mathbf{q}}^{\mathrm{BZ}} \sum_{ij} P_{ij}(\mathbf{q},\omega)\, \chi_i^{\mathbf{q}}(\mathbf{r}) \left[\, \chi_j^{\mathbf{q}}(\mathbf{r}') \,\right]^* , \tag{6.1}$$

where the matrix elements of the polarizability are defined by

$$P_{ij}(\mathbf{q},\omega) = \iint \mathrm{d}\mathbf{r}\,\mathrm{d}\mathbf{r}'\,\left[\,\chi_i^{\mathbf{q}}(\mathbf{r})\,\right]^*\,P(\mathbf{r},\mathbf{r}',\omega)\,\chi_j^{\mathbf{q}}(\mathbf{r}')\,, \tag{6.2}$$

ij refer to the index of the basis. We consider two different basis sets for the expansion of the polarizability in Eq. (6.1), namely a mixed-product basis for GW calculations and planewaves for the BSE. From this point on, we drop the frequency dependence of the polarizability, since all of the following applies to all frequencies.

The main idea of the EAS method is an additive ansatz of the polarizability [48, 49] according to $P = P^1 + P^2$, where P^μ is the polarizability obtained from the individual system μ. The additive approach is applicable to systems with negligible covalent interactions, *i.e.*, the heterostructure can be easily separated in two distinctive components. Using a plane-wave expansion of the polarizability in terms of the reciprocal lattice vectors $\mathbf{G}$, *i.e.*, $\chi_i^{\mathbf{q}}(\mathbf{r}) \to \chi_{\mathbf{G}}^{\mathbf{q}}(\mathbf{r}) = e^{i(\mathbf{q}+\mathbf{G})\mathbf{r}}/\sqrt{V}$, this approach can be trivially implemented by computing the polarizabilities of the two independent systems to obtain the coefficients $P^\mu_{\mathbf{G}\mathbf{G}'}(\mathbf{q})$ and the subsequent addition according to

$$P_{\mathbf{G}\mathbf{G}'}(\mathbf{q}) = P^1_{\mathbf{G}\mathbf{G}'}(\mathbf{q}) + P^2_{\mathbf{G}\mathbf{G}'}(\mathbf{q})\,. \tag{6.3}$$

Due to the quartic scaling of the polarizability, the additive approach itself already offers significant computational savings. Further savings can be achieved when expanding the individual polarizabilities. In the expansion step, the smallest possible unit cell is identified for each individual component for computing the polarizability. Then the polarizability of the respective component in the supercell of the heterostructure is obtained by an expansion (folding) procedure. This expansion requires to map all $(\mathbf{q}_{\mathrm{uc}}+\mathbf{G}_{\mathrm{uc}})$ vectors of the unit cell to the corresponding $(\mathbf{q}_{\mathrm{sc}}+\mathbf{G}_{\mathrm{sc}})$ vectors of the supercell, where $\mathbf{G}$ are reciprocal lattice vectors:

$$P^\mu_{\mathbf{G}_{\mathrm{uc}}\mathbf{G}'_{\mathrm{uc}}}(\mathbf{q}_{\mathrm{uc}}) \to P^\mu_{\mathbf{G}_{\mathrm{sc}}\mathbf{G}'_{\mathrm{sc}}}(\mathbf{q}_{\mathrm{sc}})\,, \tag{6.4}$$

with $\mathbf{q}_{\mathrm{uc}} + \mathbf{G}_{\mathrm{uc}} = \mathbf{q}_{\mathrm{sc}} + \mathbf{G}_{\mathrm{sc}}$ and $\mathbf{q}_{\mathrm{uc}} + \mathbf{G}'_{\mathrm{uc}} = \mathbf{q}_{\mathrm{sc}} + \mathbf{G}'_{\mathrm{sc}}$. The expansion is therefore only possible for commensurate grids $\{\mathbf{q}_{\mathrm{sc}} + \mathbf{G}_{\mathrm{sc}}\} \subseteq \{\mathbf{q}_{\mathrm{uc}} + \mathbf{G}_{\mathrm{uc}}\}$. The EAS approach has been successfully applied to the calculation of energy level alignment at molecule-metal interfaces [48, 49]. However, the developed approaches make use of a plane-wave representation of the polarizability and are not directly applicable to other basis sets, in particular those used in all-electron codes [82–84].

We extend the EAS approach in the framework of the (L)APW method, which em-

ploys augmented planewaves and local orbitals (lo) as basis functions. As we have described in section 1.5.1, in the (L)APW method, the unit cell is divided into the muffin-tin (MT) and interstitial (I) regions, where wavefunctions are described differently [93], see Eq. (1.47). The G_0W_0 implementation in **exciting** employs an auxiliary basis [83] that provides a highly flexible representation of the polarizability. This so-called mixed-product basis, used to optimally represent the product of two Kohn-Sham states, is defined as:

$$\chi_j^{\mathbf{q}}(\mathbf{r}) = \begin{cases} \gamma^{\mathbf{q}}_{\alpha NLM}(r^\alpha) = \mathrm{e}^{\mathrm{i}\mathbf{q}\cdot\mathbf{r}_\alpha}\, v_{\alpha NL}(r^\alpha)\, Y_{LM}(\hat{\mathbf{r}}^\alpha) & r^\alpha < R^\alpha_{\mathrm{MT}}\,, \\ \Lambda^{\mathbf{q}}_i(\mathbf{r}) = \frac{1}{\sqrt{\Omega}} \sum_{\mathbf{G}} \tilde{S}^*_{\mathbf{G}i}\, \mathrm{e}^{\mathrm{i}(\mathbf{G}+\mathbf{q})\cdot\mathbf{r}}\, \theta_I(\mathbf{r}) & \mathbf{r} \in \mathrm{I}\,, \end{cases} \tag{6.5}$$

where R^α_{MT} is the radius of the sphere of atom α, centered at position $\mathbf{R}_\alpha$, and the difference vector from this center is labeled as $\mathbf{r}^\alpha = \mathbf{r} - \mathbf{R}_\alpha$. Inside the MT region, the basis is constructed in terms of radial functions $v_{\alpha NL}(r^\alpha)$ for an atom of index α, and spherical harmonics $Y_{LM}(\hat{\mathbf{r}}^\alpha)$ with quantum numbers L and M. In particular, one can make use of the fact that in the MT spheres, the product of two spherical harmonics can again be expanded in spherical harmonics using Clebsch-Gordan coefficients. Therefore, an optimal set of radial functions $v_{\alpha NL}(r_\alpha)$ is constructed from the products of the radial wavefunctions $u_{\alpha l}(r^\alpha, \epsilon_{\alpha l})$, see Eq. (1.47). We calculate the overlap matrix between these products functions,

$$\mathbb{O}_{ll';l_1l'_1} = \int_0^{R^\alpha_{\mathrm{MT}}} \mathrm{d}r^\alpha\, u_{\alpha l}(r^\alpha)\, u_{\alpha l'}(r^\alpha)\, u_{\alpha l_1}(r^\alpha)\, u_{\alpha l'_1}(r^\alpha)(r^\alpha)^2\,, \tag{6.6}$$

which is then diagonalized to give the corresponding set of eigenvalues, λ^{MB}_N, and eigenvectors, $c_{ll',N}$. The eigenvectors are filtered and normalized to describe the radial basis set

$$v_{\alpha NL}(r^\alpha) = \sum_{ll'} c_{ll',N}\, u_l(r^\alpha)\, u_{l'}(r^\alpha)\,. \tag{6.7}$$

In the interstitial region, $\tilde{S}_{\mathbf{G}i}$ are the renormalized planewave eigenvectors and $\theta_I(\mathbf{r})$ is the Heaviside function which has a value of 1 in the interstitial region and zero otherwise. The product of two planewaves is a planewave, thus the overlap is given by

$$\mathbb{O}_{\mathbf{G}\mathbf{G}'} = \frac{1}{\Omega}\int_\Omega \mathrm{d}\mathbf{r}\, \theta_I(\mathbf{r})\, \mathrm{e}^{\mathrm{i}(\mathbf{G}-\mathbf{G}')\cdot\mathbf{r}}\,. \tag{6.8}$$

To obtain a set of orthonormal basis function, the overlap matrix is then diagonalized

and the basis is defined in terms of the eigenvalues λ_i^I and eigenvectors $S_{\mathbf{G}i}$, thus the normalized eigenvectors defined as

$$\tilde{S}_{\mathbf{G}i} \equiv \frac{S_{\mathbf{G}i}}{\sqrt{\lambda_i^I}} \,. \tag{6.9}$$

Finally, to take advantage of the planewave representation we define the overlap matrix elements between a mixed-basis function and a planewave as

$$w_{i\mathbf{G}}(\mathbf{q}) \equiv \frac{1}{\Omega} \int_\Omega \mathrm{d}\mathbf{r} \left[\, \chi_i^{\mathbf{q}}(\mathbf{r}) \, \right]^* \mathrm{e}^{\mathrm{i}(\mathbf{q}+\mathbf{G})\cdot\mathbf{r}} \,. \tag{6.10}$$

This quantity will be useful to construct the transformation in the addition steps.

While the polarizability is a key component in G_0W_0 in the screening of the electron-electron interaction, it plays an analogous role in the screening of the electron-hole interaction in optical excitations. We therefore make use of the same concept and extend the EAS approach to the calculations of optical properties by means of the Bethe-Salpeter equation. Unlike the G_0W_0 implementation, the BSE implementation of **exciting** currently employs a planewave representation of the polarizability. Therefore, the originally developed addition approach, Eq. (6.3), is directly applicable here.

6.2 Expansion step

We begin by outlining the procedure for expanding the polarizability (orange in Fig. 6.1). Our goal is to construct the polarizability of the supercell,

$$P^{\mathrm{sc}} = \begin{pmatrix} P_{MT,MT} & P_{MT,I} \\ P_{I,MT} & P_{I,I} \end{pmatrix} \,, \tag{6.11}$$

by expanding the polarizability of the smallest unit cell for each component through a folding procedure. In this notation, the block P_{XY} includes all matrix elements P_{ij} with $\chi_i(\mathbf{r})$ ($\chi_j(\mathbf{r}')$) being defined in the region X (Y). Note that in the preceding equation the index MT does not refer to one specific muffin-tin sphere but includes all muffin-tin spheres of the heterostructure. Due to the nature of the mixed-product basis, the MT spheres and the interstitial require very different approaches for performing the expansion. We first detail the procedure for the case, where both coordinates are in atomic spheres, $P_{\mathrm{MT,MT}}$. The matrix elements of the supercell, $P^{\mathrm{sc}}_{\mathrm{MT,MT}}$, can be obtained in terms of the matrix elements of the unit cell, $P^{\mathrm{uc}}_{\mathrm{MT,MT}}$, via a transformation from real to reciprocal

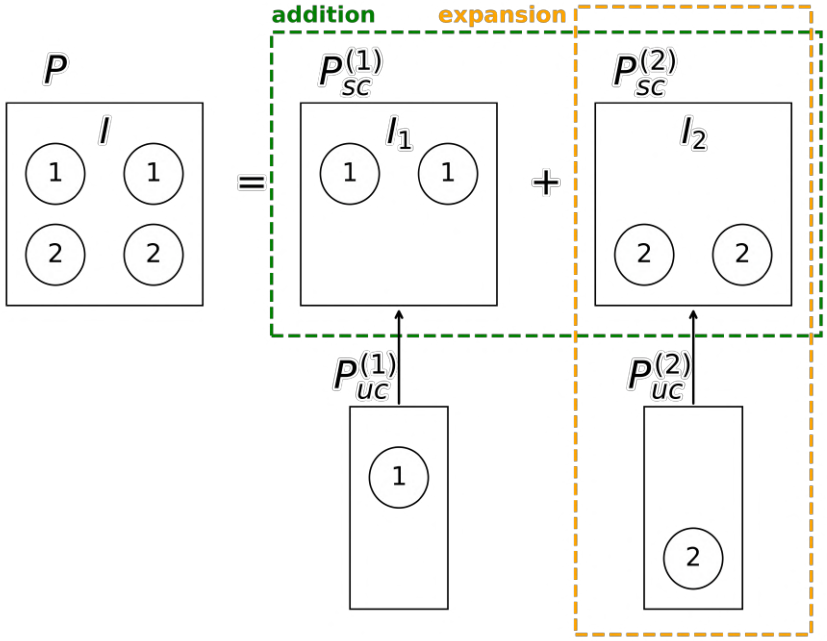

Figure 6.1: Scheme of the *expansion* & *addition* screening. The polarizability of the heterostructure, P, is approximated as the sum of the individual polarizabilities, $P^{(1)}_{\mathrm{sc}}$ and $P^{(2)}_{\mathrm{sc}}$, which are obtained as the expansion of their respective polarizability from the unit cell, $P^{(1)}_{\mathrm{uc}}$ and $P^{(2)}_{\mathrm{uc}}$, respectively.

space as follows:

$$
\begin{aligned}
P^{\mathrm{sc}}_{\alpha_{\mathrm{sc}}\alpha'_{\mathrm{sc}}}(\mathbf{q}_{\mathrm{sc}}) &= \sum_{\mathbf{R}^{\mathrm{sc}}} \mathrm{e}^{-\mathrm{i}\mathbf{q}_{\mathrm{sc}}\cdot\mathbf{R}^{\mathrm{sc}}}\, P^{\mathrm{sc}}_{\alpha_{\mathrm{sc}}\alpha'_{\mathrm{sc}}}(\mathbf{R}^{\mathrm{sc}})\,, \\
&= \sum_{\mathbf{R}^{\mathrm{sc}}} \mathrm{e}^{-\mathrm{i}\mathbf{q}_{\mathrm{sc}}\cdot\mathbf{R}^{\mathrm{sc}}}\, P^{\mathrm{uc}}_{\alpha_{\mathrm{uc}}\alpha'_{\mathrm{uc}}}(\mathbf{R}^{\mathrm{sc}} + \mathbf{R}^{\mathrm{uc}}_{\alpha'} - \mathbf{R}^{\mathrm{uc}}_{\alpha})\,, \\
&= \frac{1}{N^{\mathrm{uc}}_{\mathbf{q}}} \sum_{\mathbf{q}_{\mathrm{uc}}} \left[\sum_{\mathbf{R}^{\mathrm{sc}}} \mathrm{e}^{\mathrm{i}(\mathbf{q}_{\mathrm{uc}}-\mathbf{q}_{\mathrm{sc}})\cdot\mathbf{R}^{\mathrm{sc}}} \right] \mathrm{e}^{-\mathrm{i}\mathbf{q}_{\mathrm{uc}}\cdot(\mathbf{R}^{\mathrm{uc}}_{\alpha'}-\mathbf{R}^{\mathrm{uc}}_{\alpha})}\, P^{\mathrm{uc}}_{\alpha_{\mathrm{uc}}\alpha'_{\mathrm{uc}}}(\mathbf{q}_{\mathrm{uc}})\,, \\
&= \frac{N^{\mathrm{sc}}_{\mathbf{q}}}{N^{\mathrm{uc}}_{\mathbf{q}}} \sum_{\mathbf{q}_{\mathrm{uc}}} \mathrm{e}^{-\mathrm{i}\mathbf{q}_{\mathrm{uc}}\cdot(\mathbf{R}^{\mathrm{uc}}_{\alpha'}-\mathbf{R}^{\mathrm{uc}}_{\alpha})}\, P^{\mathrm{uc}}_{\alpha_{\mathrm{uc}}\alpha'_{\mathrm{uc}}}(\mathbf{q}_{\mathrm{uc}})\,,
\end{aligned}
\tag{6.12}
$$

where $\mathbf{R}$ are the real-space lattice vectors, $N_{\mathbf{q}}$ the number of $\mathbf{q}$-points, and the subscript uc (sc) is used to represent all unit cell (supercell) quantities. The difference of real-space

lattice vectors is re-written in terms of the atomic positions, $\tau_{\alpha_{\rm sc}} = \tau_{\alpha_{\rm uc}} + \mathbf{R}^{\rm uc}_{\alpha}$, as

$$\mathbf{R}^{\rm uc}_{\alpha'} - \mathbf{R}^{\rm uc}_{\alpha} = (\tau_{\alpha'_{\rm sc}} - \tau_{\alpha'_{\rm uc}}) - (\tau_{\alpha_{\rm sc}} - \tau_{\alpha_{\rm uc}}) \,. \tag{6.13}$$

Once the equivalent atoms in the supercell have been identified and Eq. (6.13) has been constructed, the implementation of Eq. (6.12) is straightforward.

We then construct the interstitial part of the polarizability,$P_{I,I}$, where planewaves are employed, we apply Eq. (6.4) to the interstitial mixed-product basis functions. This is achieved by first transforming the mixed-product basis to the original set of planewaves using

$$\begin{aligned} P_{\mathbf{G}\mathbf{G}'}(\mathbf{q}) &= \int \mathrm{d}\mathbf{r}\, \mathrm{d}\mathbf{r}' \left[\, \chi^{\mathbf{q}}_{\mathbf{G}}(\mathbf{r}) \,\right]^* \left\{ \sum_{\mathbf{q}'} \sum_{ij} P_{ij}(\mathbf{q}')\, \chi_i^{\mathbf{q}'}(\mathbf{r}) \left[\, \chi_j^{\mathbf{q}'}(\mathbf{r}') \,\right]^* \right\} \chi^{\mathbf{q}}_{\mathbf{G}'}(\mathbf{r}') \,, \\ &= \sum_{ij} P_{ij}(\mathbf{q})\, \langle \chi_i^{\mathbf{q}} | \chi^{\mathbf{q}}_{\mathbf{G}} \rangle^* \, \langle \chi_j^{\mathbf{q}} | \chi^{\mathbf{q}}_{\mathbf{G}'} \rangle \,, \end{aligned} \tag{6.14}$$

where the overlaps are given by

$$\begin{aligned} \langle \chi_i^{\mathbf{q}} | \chi^{\mathbf{q}}_{\mathbf{G}} \rangle =& \frac{1}{V} \int \mathrm{d}\mathbf{r} \sum_{\mathbf{G}'} \tilde{S}^*_{\mathbf{G}'i}\, \mathrm{e}^{-\mathrm{i}(\mathbf{q}+\mathbf{G}')\mathbf{r}}\, \mathrm{e}^{\mathrm{i}(\mathbf{q}+\mathbf{G})\mathbf{r}} \,, \\ =& \frac{1}{V} \sum_{\mathbf{G}'} \frac{1}{\sqrt{\lambda_i}}\, S^*_{\mathbf{G}'i} \int \mathrm{d}\mathbf{r} \mathrm{e}^{\mathrm{i}(\mathbf{G}-\mathbf{G}')\mathbf{r}} \,, \\ =& \sum_{\mathbf{G}'} \frac{1}{\sqrt{\lambda_i}}\, \lambda_i\, S^*_{\mathbf{G}i} \,, \\ =& \sqrt{\lambda_i}\, S^*_{\mathbf{G}i} \,, \end{aligned} \tag{6.15}$$

Second, the polarizability is expanded according to Eq. (6.4) to obtain it for the supercell in the planewave basis. Finally, we transform this matrix back to the mixed-product basis of the supercell using the inverse transformation of Eq. (6.14).

The polarizability matrix has two off-diagonal blocks, *i.e.*, $P_{\rm MT/\mathit{I}}$ and $P_{\mathit{I}/\rm MT}$. In these cases, the procedure described above for $P_{\rm MT,MT}$ ($P_{I,I}$) is applied only to the rows (columns) and columns (rows) of $P_{\rm MT,\mathit{I}}$ and $P_{\mathit{I},\rm MT}$, respectively. Once the expansion is performed, we transform this matrix back to the mixed-product basis of the supercell using the inverse transformation of Eq. (6.14). Finally, the polarizability of the supercell is added to its counterpart coming from the other component of the heterostructure. This addition step is described in the next section.

6.3 Addition step

We continue with the description of the addition step, where we construct the polarizability of the heterostructure by calculating the sum of the individual contributions according to $P^{\mathrm{HS}}(\mathbf{q}) = P^1(\mathbf{q}) + P^2(\mathbf{q})$ (green in Fig. 6.1). For this part, we assume that the polarizabilities of the individual components are available, either by a direct calculation of the supercell or by applying the expansion procedure presented in the preceding section. This addition procedure is again not trivial due to the dual representation of our basis. It requires to transform the polarizability from the basis of the individual components, $\{\chi_a^{\mu,\mathbf{q}}\}$, to the basis set of the heterostructure $\{\chi_A^{\mathbf{q}}\}$. The coefficients of the individual polarizability for component μ in the basis of the full heterostructure can be expressed as

$$\begin{aligned} P_{AB}^{\mu}(\mathbf{q}) &= \sum_{\mathbf{q}'} \sum_{ab} P_{ab}^{\mu}(\mathbf{q}') \, \langle \chi_A^{\mathbf{q}} | \chi_a^{\mathbf{q}'} \rangle \, \langle \chi_b^{\mathbf{q}'} | \chi_B^{\mathbf{q}} \rangle \,, \\ &= \sum_{ab} C_{aA}^{\mu *}(\mathbf{q}) \, P_{ab}^{\mu}(\mathbf{q}) \, C_{bB}^{\mu}(\mathbf{q}) \,, \end{aligned} \tag{6.16}$$

where the overlap matrix elements $C_{aA}^{\mu}(\mathbf{q}) = \langle \chi_a^{\mu,\mathbf{q}} | \chi_A^{\mathbf{q}} \rangle$ are introduced. Similar to Eq. (6.11), it is convenient to partition the polarizability of the heterostructure into different blocks according to

$$P^{\mathrm{HS}} = \begin{pmatrix} P_{MT_1,MT_1} & P_{MT_1,MT_2} & P_{MT_1,I} \\ P_{MT_2,MT_1} & P_{MT_2,MT_2} & P_{MT_2,I} \\ P_{I,MT_1} & P_{I,MT_2} & P_{I,I} \end{pmatrix} , \tag{6.17}$$

where each term represents a block of the polarizability with the basis functions coming from the different regions, similar to Eq. (6.12). We are taking advantage of the fact that the MT region of the heterostructure Ω_{MT} can be further divided into the two individual MT regions, *i.e.*, $\Omega_{\mathrm{MT}} = \Omega_{\mathrm{MT}_1} \cup \Omega_{\mathrm{MT}_2}$ with $\Omega_{\mathrm{MT}_1} \cap \Omega_{\mathrm{MT}_2} = 0$. For convenience, we drop the $\mathbf{q}$-vector index from now on. We begin by constructing the transformation matrix

$$C^{\mu} = \begin{pmatrix} C_{MT_\mu/MT_1} & C_{MT_\mu/MT_2} & C_{MT_\mu/I} \\ C_{I_\mu/MT_1} & C_{I_\mu/MT_2} & C_{I_\mu/I} \end{pmatrix} . \tag{6.18}$$

The first term, C_{MT_μ/MT_1}, corresponds to the overlap between the MT region of any of the individual layers and the MT region of layer 1 expressed in the basis of the heterostructure. For example, if $\mu = 1$, then the transformation matrix refers to the same

region MT_1, thus no transformation is required since the radial functions are equivalent for each atom in both the individual component and the heterostructure. If $\mu \neq 1$, then we have the transformation matrix between the MT region of layer 2, *i.e.*, MT_2 and MT_1, which by simple observation does not require any transformation, since these two regions are clearly distinctive. From the latter, we can conclude that $C_{MT_\mu/MT_\nu} = \delta_{\mu\nu}$.

The next term that we consider is $C_{MT_\mu/I}$, and we note that the MT region of any individual component does not overlap with the I region of the heterostructure, since all of the MT region are expressed the same way in the basis of the heterostructure, therefore, $C_{MT_\mu/I} = 0$.

For the case of the superposition of the I region of the individual components and the MT region of the heterostructure, *i.e.*, C_{I_μ/MT_1} and C_{I_μ/MT_2}, we use as an example the case of $\mu = 1$, this means, C_{I_1/MT_1}, which does not require any transformation since we are referring to the same individual component, while C_{I_1/MT_2} does require an explicit expression, since some of the planewave functions of the I region have to be transform to the MT basis of the heterostructure. From the latter, we conclude that $C_{I_\mu/MT_\mu} = 0$, while $C_{I_\mu/MT_\nu} \neq 0$.

Finally, the last term $C_{I_\mu/I}$ refers to the overlap of the I region of the individual layers and the heterostructure, since in the heterostructure we have more MT regions, these two are different, and we have to find an explicit expression for this term, *i.e.*, $C_{I_\mu/I} \neq 0$. Next, to further emphasized our previous analysis we show the transformation matrices for the two layers, *i.e.*,

$$\begin{aligned} C^1 &= \begin{pmatrix} C_{MT_1/MT_1} & C_{MT_1/MT_2} & C_{MT_1/I} \\ C_{I_1/MT_1} & C_{I_1/MT_2} & C_{I_1/I} \end{pmatrix}, \\ &= \begin{pmatrix} 1 & 0 & 0 \\ 0 & C_{I_1/MT_2} & C_{I_1/I} \end{pmatrix}, \end{aligned} \tag{6.19}$$

and

$$\begin{aligned} C^2 &= \begin{pmatrix} C_{MT_2/MT_1} & C_{MT_2/MT_2} & C_{MT_2/I} \\ C_{I_2/MT_1} & C_{I_2/MT_2} & C_{I_2/I} \end{pmatrix}, \\ &= \begin{pmatrix} 0 & 1 & 0 \\ C_{I_2/MT_1} & 0 & C_{I_2/I} \end{pmatrix}. \end{aligned} \tag{6.20}$$

In the case of the first component, Eq. (6.19), the only non-trivial components to compute are C_{I_1/MT_2} and $C_{I_1/I}$, and in the following we show how to compute them in terms of the

plane-wave eigenvectors, $S_{\mathbf{G}i}$, and the overlap matrix elements, $w^i_{\mathbf{G}}(\mathbf{q})$, see Eq. (6.10). We begin with C_{I_1/MT_2}, the interstitial region I_1 correspond to the basis of the first component , while the MT_2 comes from the basis of the second component in the heterostructure, therefore

$$\begin{aligned} C_{I_1/MT_2} &= \frac{1}{\sqrt{VN_c}} \int_{MT} \mathrm{d}\mathbf{r} \left[\sum_{\mathbf{G}} \tilde{S}^*_{\mathbf{G}i}\, \mathrm{e}^{\mathrm{i}(\mathbf{q}+\mathbf{G})\cdot\mathbf{r}} \right]^* \left[\sum_{\mathbf{R}} \mathrm{e}^{-\mathrm{i}\mathbf{q}\cdot(\mathbf{R}+\mathbf{r}_\alpha)}\, v_{\alpha NL}(r^\alpha)\, Y^*_{LM}(\mathbf{r}^\alpha) \right]^* , \\ &= \left[\sum_{\mathbf{G}} \tilde{S}^*_{\mathbf{G}i}\, \frac{1}{\sqrt{VN_c}} \int_{MT} \mathrm{d}\mathbf{r}\, \mathrm{e}^{\mathrm{i}(\mathbf{q}+\mathbf{G})\cdot\mathbf{r}} \sum_{\mathbf{R}} \mathrm{e}^{-\mathrm{i}\mathbf{q}\cdot(\mathbf{R}+\mathbf{r}_\alpha)} v_{\alpha NL}(r^\alpha)\, Y^*_{LM}(\mathbf{r}^\alpha) \right]^* , \\ &= \sum_{\mathbf{G}} \tilde{S}_{\mathbf{G}i}\, w^*_{I\mathbf{G}}(\mathbf{q}) , \end{aligned} \tag{6.21}$$

where $w_{I\mathbf{G}}(\mathbf{q})$ is the overlap element of a normal planewave with the basis functions in the MT region of the heterostructure. The other non-zero component of Eq. (6.19), $C_{I_1/I}$, is constructed by considering the basis representation of the interstitial region of the individual component and the heterostructure,

$$\begin{aligned} C_{I_1/I} &= \frac{1}{V} \int_{I_{HS}} \mathrm{d}\mathbf{r} \sum_{\mathbf{G}'\mathbf{G}} \tilde{S}_{\mathbf{G}'i}\, \mathrm{e}^{-\mathrm{i}(\mathbf{q}+\mathbf{G}')\cdot\mathbf{r}}\, \tilde{S}^*_{\mathbf{G}I}\, \mathrm{e}^{\mathrm{i}(\mathbf{q}+\mathbf{G})\cdot\mathbf{r}} , \\ &= \frac{1}{\Omega} \sum_{\mathbf{G}'\mathbf{G}} \tilde{S}_{\mathbf{G}'i}\, \tilde{S}^*_{\mathbf{G}I} \int_{I_{HS}} \mathrm{d}\mathbf{r}\, \mathrm{e}^{\mathrm{i}(\mathbf{G}-\mathbf{G}')\cdot\mathbf{r}} , \\ &= \sum_{\mathbf{G}'} \tilde{S}_{\mathbf{G}'i}\, \frac{1}{\Omega} \sum_{\mathbf{G}} \tilde{S}^*_{\mathbf{G}I} \int_{I_{HS}} \mathrm{d}\mathbf{r}\, \mathrm{e}^{\mathrm{i}(\mathbf{G}-\mathbf{G}')\cdot\mathbf{r}} . \end{aligned} \tag{6.22}$$

We may define the integral $\mathcal{I}_{\mathbf{G}}$ over a planewave evaluated for the interstitial region of the heterostructure unit cell as

$$\mathcal{I}_{\mathbf{G}} = \int_{I_\Omega} \mathrm{d}\mathbf{r}\, \mathrm{e}^{\mathrm{i}\mathbf{G}\cdot\mathbf{r}} , \tag{6.23}$$

such that we can express the matrix elements

$$\begin{aligned} C_{I_1/I} &= \sum_{\mathbf{G}'} \tilde{S}_{\mathbf{G}'i}\, \frac{1}{\Omega} \sum_{\mathbf{G}} \tilde{S}^*_{\mathbf{G}I}\, \mathcal{I}_{\mathbf{G}-\mathbf{G}'} \,, \\ &= \sum_{\mathbf{G}'} \tilde{S}_{\mathbf{G}'i} \left[\frac{1}{\Omega} \sum_{\mathbf{G}} \tilde{S}_{\mathbf{G}I}\, \mathcal{I}^*_{\mathbf{G}-\mathbf{G}'}\right]^* , \\ &= \sum_{\mathbf{G}'} \tilde{S}_{\mathbf{G}'i}\, w^*_{I\mathbf{G}'} \,. \end{aligned} \tag{6.24}$$

where $w_{I\mathbf{G}}(\mathbf{q})$ is the overlap element of a normal planewave with the basis functions in the I region of the heterostructure. We note that the transformation of the second component can be achieved by using Eq. (6.21) for C_{I_2/MT_1} and Eq. (6.24) for $C_{I_2/I}$. We now show the general expressions to calculate the components of Eq. (6.17). If both indices AB belong to the same MT region, *i.e.*, P_{MT_μ,MT_μ}, the transformation to the heterostructure's basis is given by the following expression

$$P_{MT_\mu,MT_\mu} = P^\mu_{MT_\mu,MT_\mu} + (C^\nu_{I_\nu,MT_\mu})^*\, P^\nu_{I_\nu,I_\nu}\, C^\nu_{I_\nu,MT_\mu} \,. \tag{6.25}$$

To construct the polarizability of two different MT regions, *i.e.*, P_{MT_μ,MT_ν}, we need to consider the contribution of the interstitial region of one of the components

$$P_{MT_\mu,MT_\nu} = P^\mu_{MT_\mu,I_\mu}\, C^\mu_{I_\mu,MT_\nu} + (C^\nu_{I_\nu,MT_\mu})^*\, P^\nu_{I_\nu,MT_\nu} \,. \tag{6.26}$$

If both indices AB belong to the interstitial region of the heterostructure, *i.e.*, $P_{I,I}$, the polarizability is written as

$$P_{I,I} = \sum_{\mu} (C^\mu_{I_\mu,I})^*\, P^\mu_{I_\mu,I_\mu}\, C^\mu_{I_\mu,I} \,. \tag{6.27}$$

If either A or B correspond to the MT region, while the other to the interstitial region of the heterostructure, the polarizabilities, $P_{MT_1,I}$ and P_{I,MT_1} are calculated as

$$P_{MT_\mu,I} = P^\mu_{MT_\mu,I_\mu}\, C^\mu_{I_\mu,I} + (C^\nu_{I_\nu,MT_\mu})^*\, P^\nu_{I_\nu,I_\nu}\, C^\nu_{I_\nu,I} \,, \tag{6.28}$$

Once the polarizability of the heterostructure, Eq. (6.17), has been constructed, it enters either the calculation of the dynamically screened Coulomb potential of G_0W_0 or the statically screened Coulomb potential in the BSE module.

6.4 Example of selected materials

To evaluate the accuracy of our implementation we compare our results with the standard G_0W_0 and BSE calculations, *i.e.*, using the full calculation of the polarizability. We show the quasi-particle (QP) band structure and the dielectric function of WSe_2 bilayer and pyridine@MoS_2 obtained by calculating the polarizability with the EAS method. We choose these systems due to the weak hybridization and predominant vdW interactions [54].

The top left panel of Fig. 6.2 shows the schematic representation of how to compute the additive screening for the example of the WSe_2 bilayer. Since both layers and thus the double layer contain one unit cell, we only probe the additive step in this case. We consider the AB stacking [183] and the interlayer distance of 3.21 Å, as obtained by optimizing the geometry using the PBE functional and the TS vdW correction[120, 121]. The sampling of the Brillouin zone (BZ) is performed with a homogeneous 12×12×1 Monkhorst-Pack **k**-point grid for both the individual components and the heterostructure. We use 200 empty states for the calculation of the polarizability in both systems, which ensures that the band edges are overall sufficiently converged. We consider a Coulomb truncation along the out-of-plane direction, as used in Ref. [135].

The top right panel of Fig. 6.2 shows the QP band structure of the bilayer on top of PBE calculations as the DFT starting point. We observe very good agreement between the EAS approximation and the full calculation. The indirect fundamental gap, found between Γ and T, a point between toward Γ and K, $E_g(\Gamma T)$ has a value of 2.39 eV and 2.41 eV for the EAS and full calculation, respectively. The direct gap at K, $E_g(KK)$, is 2.84 eV and 2.79 eV for EAS and full calculation, respectively. The bottom panels show the imaginary and real parts of the dielectric function based on the QP band structure. Comparing the results between the EAS approximation and the full BSE calculation, again very good agreement is obtained. The optical gaps are 2.63 eV and 2.64 eV, respectively.

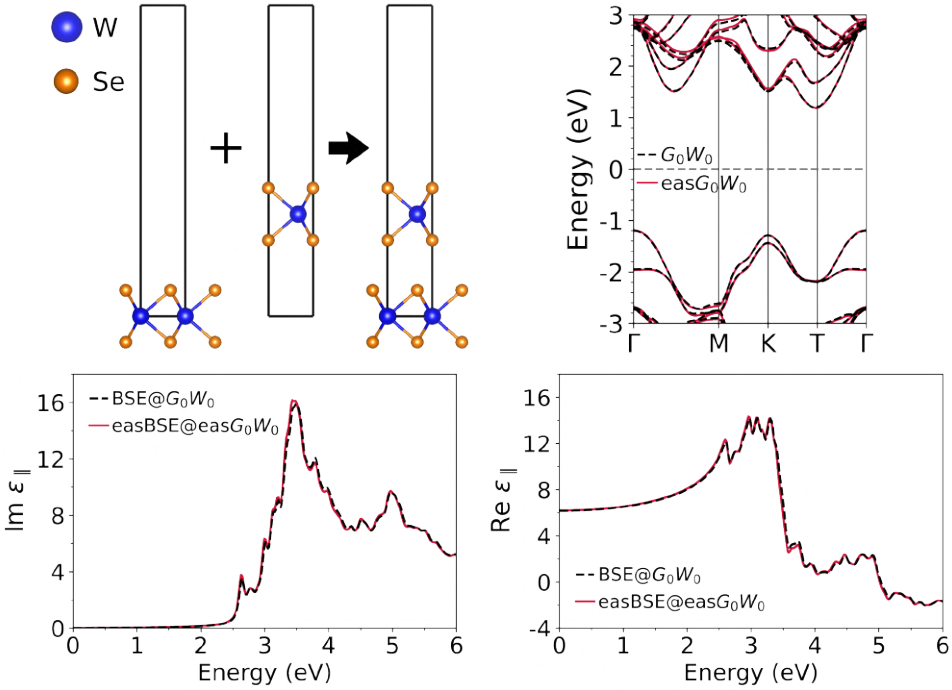

Figure 6.2: Top left: schematic representation of how to compute the additive screening, for the example of the WSe_2 bilayer. Top right: QP band structure calculated with the *expansion & addition* method (blue) compared to the full calculation (red). Bottom: Imaginary part (left) and real part (right) of the in-plane component of the dielectric function obtained by the EAS approach (blue) and the full calculation (black).

The top left panel of Fig. 6.3 shows the schematic representation of the EAS calculation for pyridine@MoS_2, a prototypical hybrid material. In this example, we put our full implementation to the test by performing an expansion of the polarizability calculated for the MoS_2 monolayer to a 3×3×1 supercell. Due to the sensitivity of our methodology to atomic positions, the unit cell of MoS_2 is expanded to form a commensurate supercell, with atomic positions kept fixed at ideal lattice sites. The monolayer of pyridine is then placed at an interlayer distance of 3.19 Å as obtained in Ref. [54] using the TS vdW correction. The BZ of the supercell is sampled with a 3×3×1 **k**-grid. As in the previous example, the calculation of the polarizability of the heterostructure is performed by using 200 empty states, while the polarizability of the unit cell is computed using a 9×9×1 **k**-grid and 100 empty bands.

The top right panel of Fig. 6.3 shows the QP band structure calculated with the EAS method (red) and the full calculation (black). As in the case of the WSe_2 bilayer, we find very good agreement between the EAS method and the full implementation. The

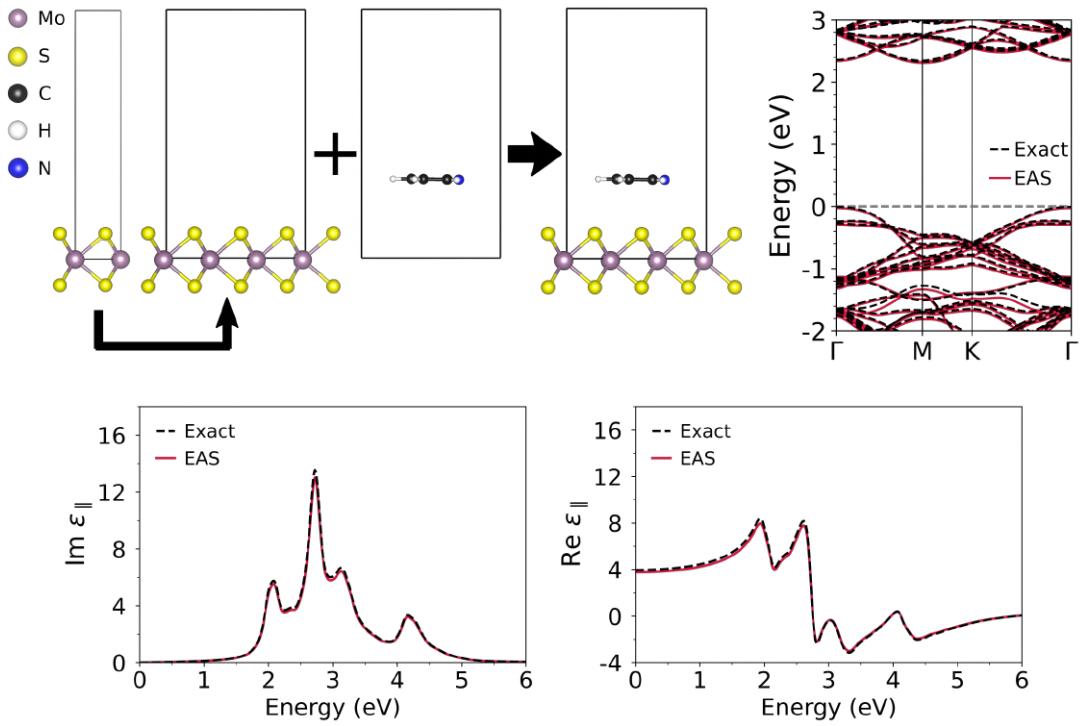

Figure 6.3: Top left: schematic representation of how to compute the EAS method for the example of pyridine@MoS_2. Top right: QP band structure calculated with the *expansion & addition* method (red) compared to the full calculation (black). Bottom: Imaginary part (left) and real part (right) of the in-plane component of the dielectric function obtained by the EAS approach (red) and the full calculation (black).

fundamental gap of pyridine@MoS_2 at the Γ-point due to the folding of the K-point are 2.32 eV and 2.36 eV, respectively. The bottom panel of Fig. 6.3 shows the imaginary and real parts of the dielectric function calculated with both the EAS method (red) and the full calculation (black). The optical properties are calculated on top of the QP band structure and result in an optical gap of 2.00 eV and 2.02 eV, respectively.

There are two possible outcomes: if the result confirms the hypothesis, then you've made a measurement. If the result is contrary to the hypothesis, then you've made a discovery.

Enrico Fermi

7 Conclusions and outlook

In this thesis, we employed many-body perturbation theory (MBPT) to study the electronic and optical properties of three representative hybrid inorganic organic systems (HIOS), namely, pyrene@MoS_2, pyridine@MoS_2 and PTCDA@WSe_2.

We first reported on the effect of geometry optimization on the electronic properties of the MoS_2 monolayer (Section 2.1.2). Our findings indicate that the HSE and PBE+TS functionals give the best agreement with the experimental geometry. However, the QP band gap, calculated using the G_0W_0 approximation, is in better agreement with the experimental gap than those obtained with DFT. In order to account for electron-phonon interaction (EPI), we computed the quasiparticle (QP) energies by explicitly including the electron-phonon self-energy. This approach captured the renormalization of the band structure due to zero-point vibrations and temperature. The corresponding zero-point renormalization (ZPR) of the band gap was also evaluated (see Section 2.1.4). Finally, the imaginary part of the dielectric function was obtained by solving the BSE. The electronic and optical properties of WSe_2 were calculated using the same framework (see Section 2.2).

We discussed the structural properties of our HIOS by performing a geometry optimization, revealing that vdW and dipole interactions dominate in these systems, leading to physisorption. The energy level alignment was studied by means of DFT, and afterwards by computing the QP eigenvalues with the G_0W_0 approximation. We found

that the type-II level alignment predicted by both PBE and HSE is incorrect. After the inclusion of self-energy corrections does the alignment change to type I. This finding was observed for our three prototypical HIOS. The polarization-induced effects were systematically calculated for each heterostructure. Among the examined systems, the most pronounced effects were found for pyridine@MoS_2, which we attribute to the presence of a permanent molecular dipole and a stronger hybridization between the molecular orbitals and the substrate electronic states, in comparison to the other systems.

The electron-phonon spectral function was computed and analyzed for pyrene@MoS_2 and pyridine@MoS_2, revealing the emergence of satellites attributable to the molecular vibrational modes. In the case of pyrene@MoS_2, the energy difference between the satellite peak and the HOMO peak corresponds to the energy of a C-H stretch mode. In pyridine@MoS_2, we discussed two satellites observed in the spectral function. The energy difference between the first satellite peak and the QP peak corresponds to the out-of-plane ring bend mode, while the out-of-plane C-H vibrational modes are responsible for the second satellite.

The optical properties of our HIOS were studied by solving the BSE. In the case of pyrene@MoS_2 and PTCDA@WSe_2, charge-transfer excitons were found in the visible region, while in the case of pyridine@MoS_2, hybrid-like excitons were obtained. Overall, our findings indicated that hybrid systems consisting of low-dimensional semiconductors and organic π-conjugate molecules exhibit a rich variety of excitons. These findings suggest that such hybrid systems offer a promising environment for the exploration of many-body interactions and exciton physics.

The molecules examined in this thesis can be regarded as a reference for other organic molecules. For instance, the type-II level alignment obtained with PBE is also anticipated for other conjugated molecules, such as oligoacenes, provided that the interlayer distance is sufficiently large to adequately preserve the band structure of the pristine constituents. A comprehensive examination of the conditions necessitates a thorough consideration of the molecular properties, including but not limited to aromaticity, permanent dipole, ionization potential, work function, density, and geometry of the corresponding monolayers.

Finally, we extended a recently developed method for calculating the polarizability of weakly bound systems within planewave basis sets to the case of an all-electron basis set. Our implementation of the *expansion & addition screening* (EAS) method obtains the QP band structure of weakly bound heterostructures with high accuracy, as illustrated by the examples of the WSe_2 bilayer and the hybrid material pyridine@MoS_2. Going beyond previous work, we have successfully applied these method also within the BSE formalism, which we have demonstrated by computing the optical spectra.

As part of the outlook of this thesis we clarify the following question: why can't we just apply the best possible methodology to hybrid materials? The reason is the unfortunate scaling of many-body methodology that limits us to a system size of about ≈100 atoms for most codes implementing MBPT, in particular all-electron codes. Typically, the G_0W_0 approximation is the method of choice, but the starting-point dependence reduces the quality of the results. A self-consistent GW variant would provide a better description of the electronic properties, unfortunately, such calculations are currently computationally not feasible for large unit cells. Concerning charge-neutral spectroscopy, BSE is a valid state-of-the-art approach for static optical and core-level excitations, being feasible for moderately large system sizes.

Another important aspect is the urgent need for benchmarks that systematically assess the impact of all methodological choices, including approximations, starting points, numerical implementations, and computational parameters. This is particularly relevant for complex systems such as HIOS. For instance, a proper evaluation of both the electron-electron and electron-phonon self energies with respect to the number of bands and the sampling of the BZ would be necessary. Conducting benchmarking studies that evaluate these contributions on equal footing is essential. The availability of such data would facilitate the assessment of the true result for a given level of theory and the determination of the necessary elements for a reliable solution to a specific problem. However, it must be acknowledged that for complex systems such as HIOS, achieving full numerical convergence can be exceedingly challenging. Consequently, the computational parameters cannot be as strictly controlled as in conventional benchmark systems such as diamond or SiC. In these systems, convergence can typically be achieved under more standardized settings.

A
Organic molecules

In this Appendix, we focus on the molecular component of the heterostructure, namely, pyrene ($C_{16}H_{10}$), pyridine (C_4H_4N) and PTCDA ($C_{24}H_8O_6$). These molecules are considered organic and π-conjugated. We emphasized that we have studied them with **`exciting`**, which considers periodic boundary conditions.

A.1 Pyrene

Pyrene contains 16 carbon and 10 hydrogen atoms, its geometry resembles the fusion of four benzene rings. However, the carbon atoms in pyrene form a continuous and extended conjugated system that results in the shared edges of adjacent rings, forming a larger conjugated aromatic system. A more accurate way to describe this molecule is that it is a polycyclic aromatic hydrocarbon (PAH). Pyrene, a π-conjugated molecule without a permanent dipole, exhibits interesting photophysical properties, such as prominent fluorescence bands, as measured by optical spectroscopy [85, 184]. Figure A.1 shows the structure as well as the electron density of the KS HOMO and LUMO. The HOMO is a π-orbital, where the carbons on the diagonal of the molecule do not have electronic density. The LUMO is an antibonding π-orbital, where the carbons on the diagonal of the molecule also do not have electronic density. The HOMO-LUMO gap obtained with PBE corresponds to approximately 2.5 eV [54], while the G_0W_0 approximation increases the gap to 5.2 eV. In comparison, the Hartree-Fock approach reports a gap of 8.65 eV [184].

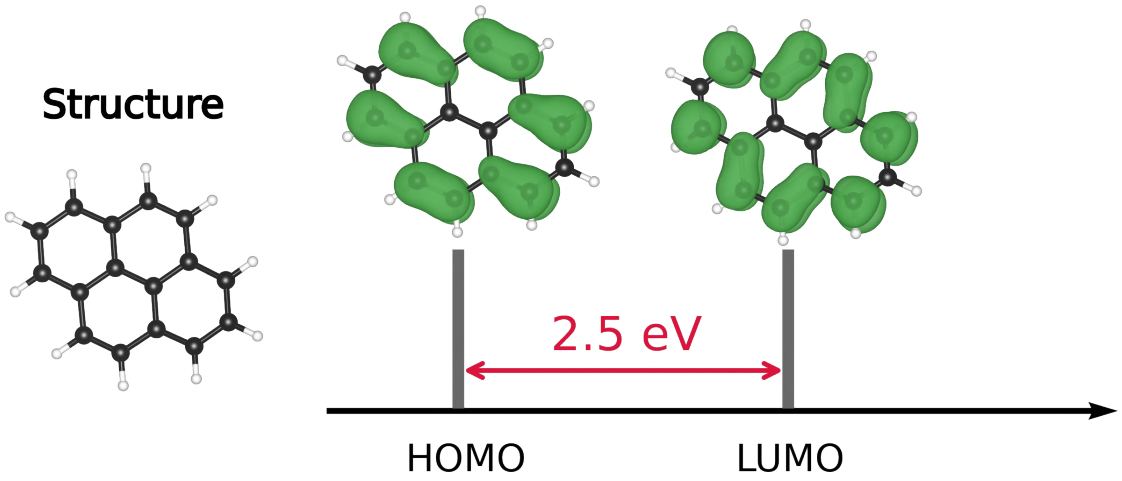

Figure A.1: Left: Structure of pyrene. Right: PBE HOMO-LUMO gap and their orbital representation in real space.

Pyrene has 78 modes, but due to translational and rotational symmetries, 6 modes are zero (or numerically close to zero), meaning that it has 72 normal modes. In Table A.1, we show the vibrational energies of pyrene computed in this thesis, and the values obtained in Ref. [185]. Overall, the vibrational energies are in good agreement, and the small differences could be related to the different methodologies used. We follow the classification of the vibrations proposed by Baba *et al* [185], there are 8 vibration types, C-H bend (in-plane and out-of-plane), C-H stretch, C-C stretch, ring deform (in-plane and out-of-plane), ring breathing, out-of-plane ring torsion, out-of-plane ring wagging and butterfly. The modes with largest vibrational energy correspond to C-H stretch.

Table A.1: Vibrational energies of pyrene calculated with **exciting** and compared with theoretical and experimental results from Ref. [185], where the energies were obtained using *ab initio* calculations and fluorescence excitation spectroscopy.

Number	Vibration type	This work [meV]	Theory [meV]	Exp. [meV]
1	Butterfly	13.94	11.904	–
2	oop ring deform	23.43	18.476	–
3	oop ring deform	32.82	25.916	–
4	oop ring torsion	33.71	30.13	–
5	oop ring wagging	35.55	31.99	–
6	Ring deform	38.60	43.89	–
7	oop ring deform	42.27	48.98	–
8	Ring deform	49.26	50.34	49.84
9	Ring deform	49.56	56.54	55.92
10	oop ring deform	52.58	61.13	–
11	oop ring deform	55.30	62.00	–
12	Ring deform	58.18	62.00	–
13	Ring deform	58.51	62.12	62.00
14	oop ring deform	59.65	65.72	–
15	Ring deform	60.35	67.82	–
16	oop ring deform	67.16	70.80	–
17	Ring breathing	67.33	72.78	73.53
18	oop C-H bend	74.19	83.70	–
19	Ring deform	78.55	86.05	–
20	oop ring deform	81.96	88.04	–
21	Ring deform	83.37	91.63	91.14
22	oop C-H bend	90.16	92.50	–
23	oop C-H bend	91.53	94.116	–

Number	Vibration type	This work [meV]	Theory [meV]	Exp. [meV]
24	oop C-H bend	91.90	99.57	–
25	Ring deform	96.90	99.69	99.82
26	oop C-H + C-C bend	102.06	99.94	–
27	Ring deform	106.37	102.05	–
28	oop C-H bend	109.56	104.65	–
29	oop C-H bend	113.70	110.48	–
30	oop C-H bend	115.25	112.22	–
31	oop C-H bend	119.66	119.41	–
32	C-H bend + ring deform	121.13	119.90	–
33	oop C-H bend	123.36	120.03	–
34	oop C-H bend	126.81	120.15	–
35	oop C-H bend	131.29	121.272	–
36	Ring deform	131.90	124.12	–
37	C-H bend + ring deform	136.49	133.42	132.92
38	Ring deform	137.53	136.27	–
39	C-H bend + ring deform	141.41	137.88	137.76
40	C-H bend	145.18	142.60	–
41	C-H bend	147.84	142.84	141.35
42	C-H bend	149.02	146.69	150.28
43	C-H bend + ring deform	149.24	147.43	–
44	C-H bend + ring deform	159.77	150.66	–
45	C-H bend + ring deform	161.48	154.38	153.51
46	C-H bend + ring deform	161.67	154.62	153.51
47	C-H bend + ring deform	167.67	155.12	–
48	C-H bend + C-C stretch	169.29	164.30	–

Number	Vibration type	This work [meV]	Theory [meV]	Exp. [meV]
49	Ring deform	174.68	165.29	164.42
50	C-H bend + ring deform	174.94	171.24	170.12
51	C-C stretch	175.56	174.34	174.84
52	C-C stretch	176.34	175.46	–
53	C-H bend + C-C stretch	197.24	178.31	–
54	C-H bend + ring deform	198.03	178.43	–
55	C-H bend + C-C stretch	200.87	181.41	–
56	C-H bend + C-C stretch	201.68	185.13	–
57	C-H bend + C-C stretch	204.46	187.61	187.61
58	C-H bend + C-C stretch	205.64	194.92	–
59	C-C stretch	208.92	198.77	194.80
60	C-C stretch	209.45	199.88	–
61	C-H bend + C-C stretch	209.80	201.00	–
62	C-C stretch	210.25	204.10	201.37
63	C-H stretch	347.64	386.13	–
64	C-H stretch	348.66	386.26	–
65	C-H stretch	349.80	386.63	–
66	C-H stretch	351.16	386.63	–
67	C-H stretch	353.59	387.50	–
68	C-H stretch	354.22	387.62	–
69	C-H stretch	354.80	388.61	–
70	C-H stretch	355.86	388.61	–
71	C-H stretch	356.83	389.60	–
72	C-H stretch	358.95	389.73	–

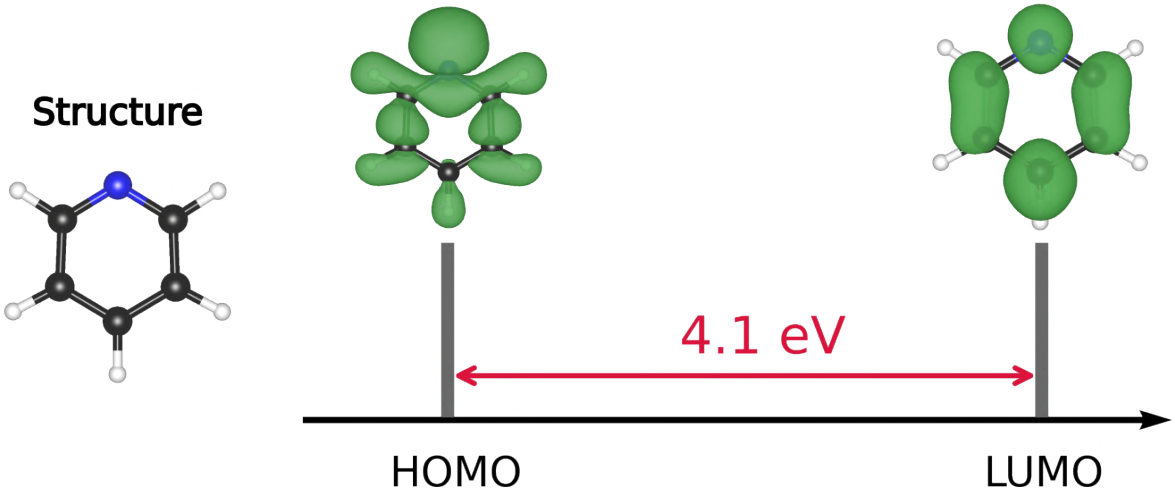

Figure A.2: Left: Structure of pyridine. Right: PBE HOMO-LUMO gap and the orbital representation in real space.

A.2 Pyridine

Pyridine is a π-conjugated molecule with a permanent dipole, its geometry resembles the benzene ring, however, one of the C-H groups has been replaced with a nitrogen atom. This molecule is regarded as a basic building block of polycyclic aromatic hydrocarbons, π-conjugated oligomers, and many organic semiconductors and dyes [86]. Moreover, pyridine is an electron donor, explained due to the lone pair of electrons in the nitrogen atom. Figure A.2 shows the structure as well as the electron density of the KS HOMO and LUMO. The HOMO of pyridine corresponds to a n-orbital, where the p-orbital of nitrogen is present. The HOMO-LUMO gap obtained with PBE amounts to 4.1 eV, while the G_0W_0 approximation increases the gap to 8.3 eV [54].

Pyridine has 33 modes, due to translational and rotational symmetries 6 modes are zero, meaning that it has 27 normal modes. In Table A.2, we show the vibrational energies of pyridine computed in this thesis, and the values reported in Ref. [186]. Similar to the case of pyrene, the differences in the vibrational energies could be related to the different methodologies applied. Overall, our results seem to be underestimating the energies. In Fig. A.3, we show the classification of the vibrations, where the types are: out-of-plane ring bend, out-of-plane C-H bend, C-H pendulum, ring breathing, and C-H stretch.

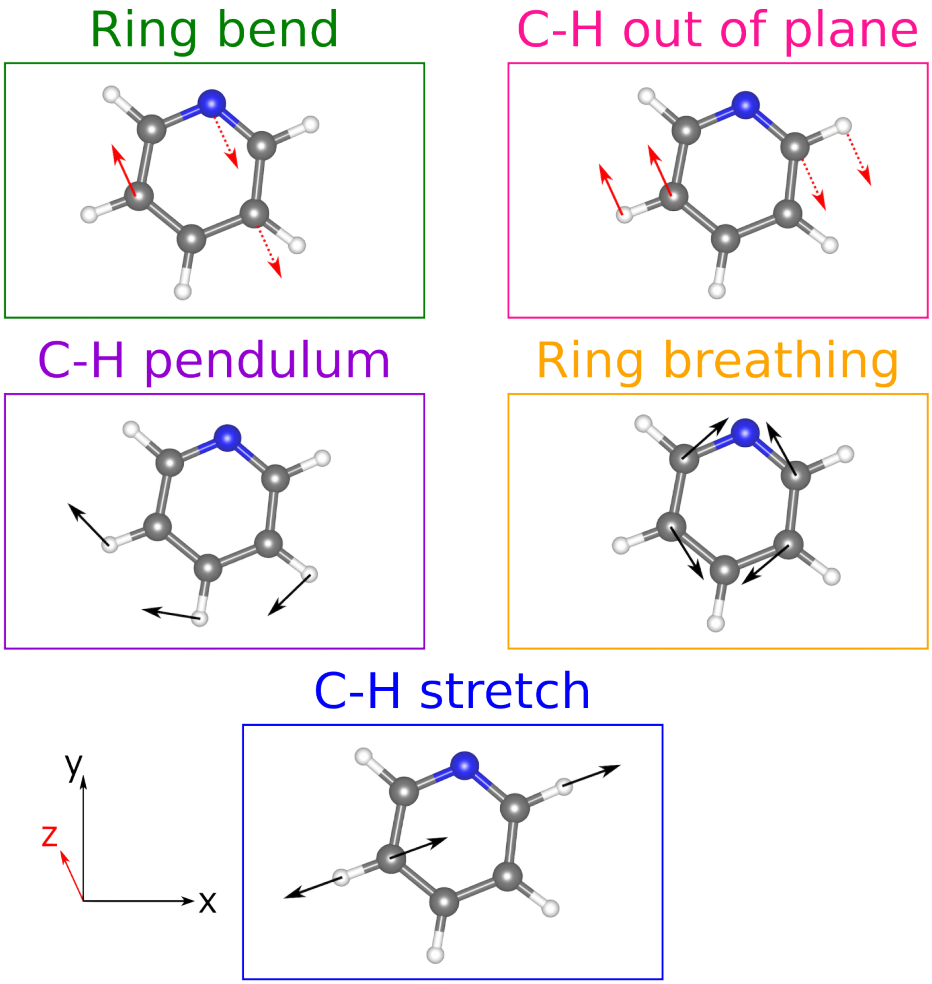

Figure A.3: The vibration types of pyridine are classified according to the energy, from smaller to larger, starting with oop ring bend, oop C-H bend, C-H pendulum, ring breathing and C-H stretch.

Table A.2: Vibrational energies of pyridine calculated with **exciting** and compared with theoretical values from Ref. [186].

Number	Vibration type	This work [meV]	Theory [meV]
1	oop ring bend	16.03	56.544
2	oop ring bend	34.99	60.264
3	oop ring bend	63.70	84.94
4	oop ring bend	85.31	92.38
5	oop ring bend	95.09	101.30
6	oop C-H	98.50	107.50
7	oop C-H	108.67	127.72
8	oop C-H	111.53	135.65
9	oop C-H	121.07	137.26
10	oop C-H	129.00	141.85
11	C-H pendulum	133.03	145.20
12	C-H pendulum	133.22	145.82
13	C-H pendulum	135.25	148.18
14	C-H pendulum	136.28	148.55
15	C-H pendulum	164.30	154.13
16	Ring breathing	167.09	165.78
17	Ring breathing	175.17	168.39
18	Ring breathing	181.30	189.59
19	Ring breathing	188.57	200.75
20	Ring breathing	197.44	205.96
21	C-H stretch	213.30	219.60
22	C-H stretch	227.51	220.84
23	C-H stretch	236.81	414.16
24	C-H stretch	360.20	416.51
25	C-H stretch	365.61	417.26
26	C-H stretch	381.04	419.12
27	C-H stretch	386.05	420.23

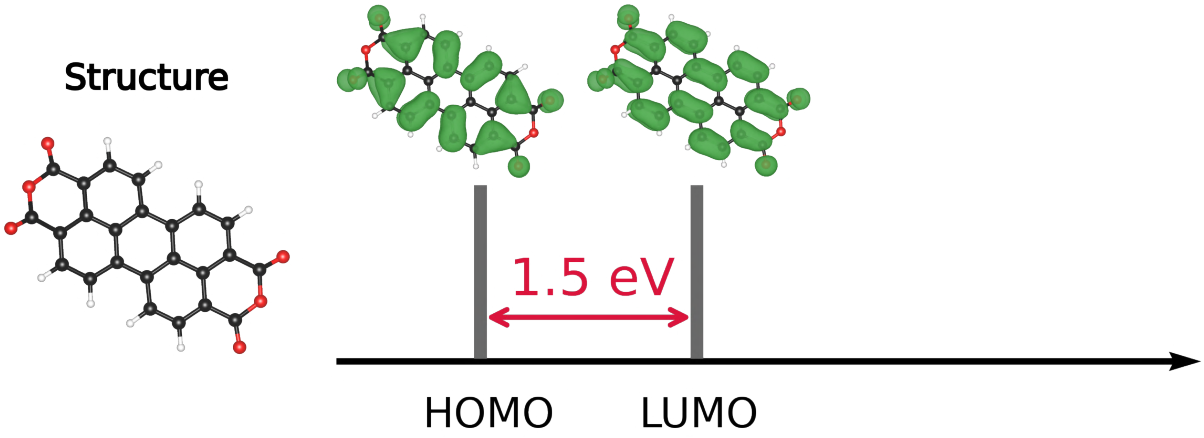

Figure A.4: Left: Structure of PTCDA. Right: PBE HOMO-LUMO gap and the orbital representation in real space.

A.3 PTCDA

PTCDA is a key model system for the fabrication of flat molecular layers of organic semiconductors adsorbed on pristine surfaces [187] and for the characterization of optical excitations [188]. It is composed of 24 carbon, 8 hydrogen, and 6 oxygen atoms. This molecule has a permanent dipole [43, 63], because the carbonyl groups (C-O) in the anhydrides are highly polar. The strong electron acceptor property is due to the electron-withdrawing nature of the anhydride groups, which can stabilize negative charge [189]. Figure A.4 shows the structure as well as the electron density of the KS HOMO and LUMO. The HOMO of PTCDA is primarily composed of π-electrons, delocalized across the molecule's perylene core, and is formed by the overlap of p-orbitals from the carbon atoms. The LUMO is also a π^* orbital, meaning it is an anti-bonding orbital. This molecular orbital can accept electrons during excitation (*e.g.*, upon absorption of light). Due to the presence of lone pairs of electrons on the oxygen atoms, the energy of the LUMO is lower. The HOMO-LUMO gap obtained with PBE corresponds to approximately 1.5 eV [7, 169], while the G_0W_0 approximation increases the gap to 4.4 eV [44].

B
Computational details

All structure optimizations are performed using the all-electron code FHI-aims [164] by minimizing the amplitude of the interatomic forces below a threshold value of 10^{-3} eV Å^{-1}. For all species a *tight* basis is used. Moreover, TIER2 basis is used for the species of the molecules, while TIER1 and TIER1+dg for the transition metals (Mo,W) and chalcogenides (S,Se), respectively. The subsequent ground-state, G_0W_0, phonons, electron-phonon, band unfolding and BSE calculations are performed using the all electron full-potential code **exciting** [93]. Atomic structures and isosurfaces are visualized using the VESTA software [190].

B.1 Numerical parameters of MoS_2, pyrene@MoS_2, and pyridine@MoS_2

GS properties are calculated using DFT [56, 96] with the GGA in the PBE parametrization [99] for the exchange-correlation functional. The sampling of the Brillouin zone (BZ) is carried out with a homogeneous 15×15×1 Monkhorst-Pack **k**-point grid for the pristine MoS_2 and a 3×3×1 **k**-grid for the supercells. To account for vdW forces between substrate and molecules and intermolecular interactions, we adopt the TS method [120, 121]. The muffin-tin (MT) spheres in the inorganic component are chosen to have equal radii of 2.2 bohr. For the molecules, the corresponding radii are 0.8 bohr for hydrogen (H) and 1.2 bohr for carbon (C) and nitrogen (N). We use a basis-set cutoff of G_{max}=4.375 bohr^{-1}.

QP energies are computed within the G_0W_0 approximation [58, 78, 104] by solving

the QP equation (see Eq. (1.23)). 600 and 200 empty states are included to compute the frequency-dependent dielectric screening within the random-phase approximation in pristine MoS_2, and the hybrid systems, respectively. A 2D truncation of the Coulomb potential in the out-of-plane direction z is employed [191]. Band structure and DOS are computed on dense meshes by using interpolation with maximally-localized Wannier functions [192, 193]. For the solution of the BSE [60, 111, 194] on top of the QP band structure, the screened Coulomb potential is computed using 100 empty bands. In the construction and diagonalization of the BSE Hamiltonian, 16 occupied and 14 unoccupied bands are included, and a 12×12×1 shifted k-point mesh is adopted for the hybrid systems. In the case of pristine MoS_2, we use 5 occupied, 7 unoccupied bands and a **k**-mesh of 18×18×1. These parameters ensure well-converged spectra within the energy window up to 6 eV. A Lorentzian broadening of 100 meV is applied to the spectra to mimic lifetime effects. Spin-orbit coupling is not considered.

The band unfolding is calculated by symmetry mapping of the Bloch-vector-dependent quantities defined in the supercell into the unit-cell calculations. Here, the wavefunctions are constructed in a uniform real space grid of 120×120×120 and used to calculate the spectral function.

The dynamical matrices and potential response are calculated with a coarse **q**-point grid of 6×6×1 for the pristine MoS_2 and **Γ**-point only for the hybrid systems. The electron-phonon matrix elements are then interpolated to a fine grid of 33×33×1 in the case of the pristine MoS_2 and to a 12×12×1 grid for the interface. The electron-phonon self-energy is computed using a frequency grid of 1000 point.

B.1.1 Convergence of MoS_2 monolayer

In the top panel of Fig. B.1, the dependence of the KS band gap, computed with the functional PBE, on the **k**-grid is shown. For the number of points, $N_{\mathbf{k}}$, in in-plane direction of the hexagonal 2D BZ, multiples of 3 are chosen such to include the high-symmetry point **K**. A 6×6×1 **k**-grid, *i.e.*, $N_{\mathbf{k}} = 6$, is sufficient to obtain a value converged within 0.01 eV. The bottom panel shows the dependence of the gap on the basis-set size in terms of the parameter $R_{MT}G_{max}$.

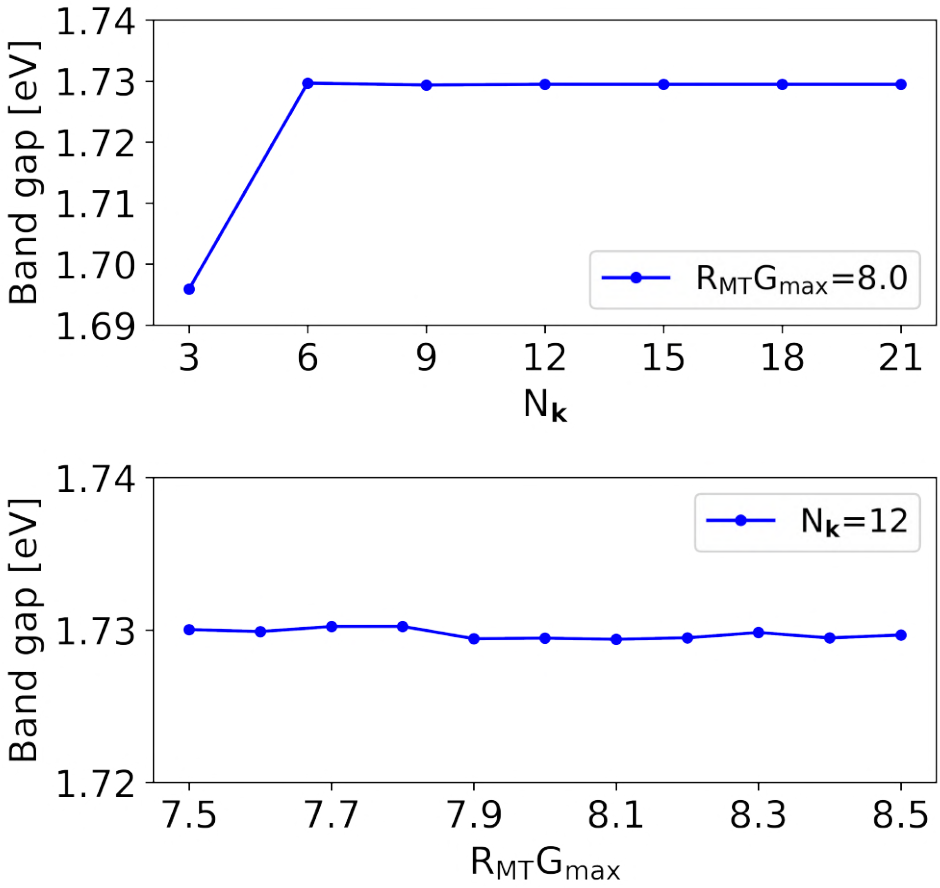

Figure B.1: KS-PBE band gap of the MoS_2 monolayer at the high-symmetry point **K** calculated for different **k**-grids (top) and parameters $R_{MT}G_{max}$ (bottom).

Figure B.2 depicts the convergence of the QP band gap, computed with the G_0W_0 approximation. In the top panel, its dependence on the number of empty states is plotted. For pristine MoS_2, it is known [33–35] that a large number of empty bands is required to ensure a direct band gap at **K**. Indeed, using less than 400 empty states results in an indirect gap. We proceed with a value of 600 for which we show in the bottom panel the dependence of the QP band gap on the **k**-grid. The bottom panel of Fig. B.2 presents the in-plane component of the imaginary part of the dielectric constant for different **k**-grids. These calculations are performed by solving BSE on top of the QP band structure.

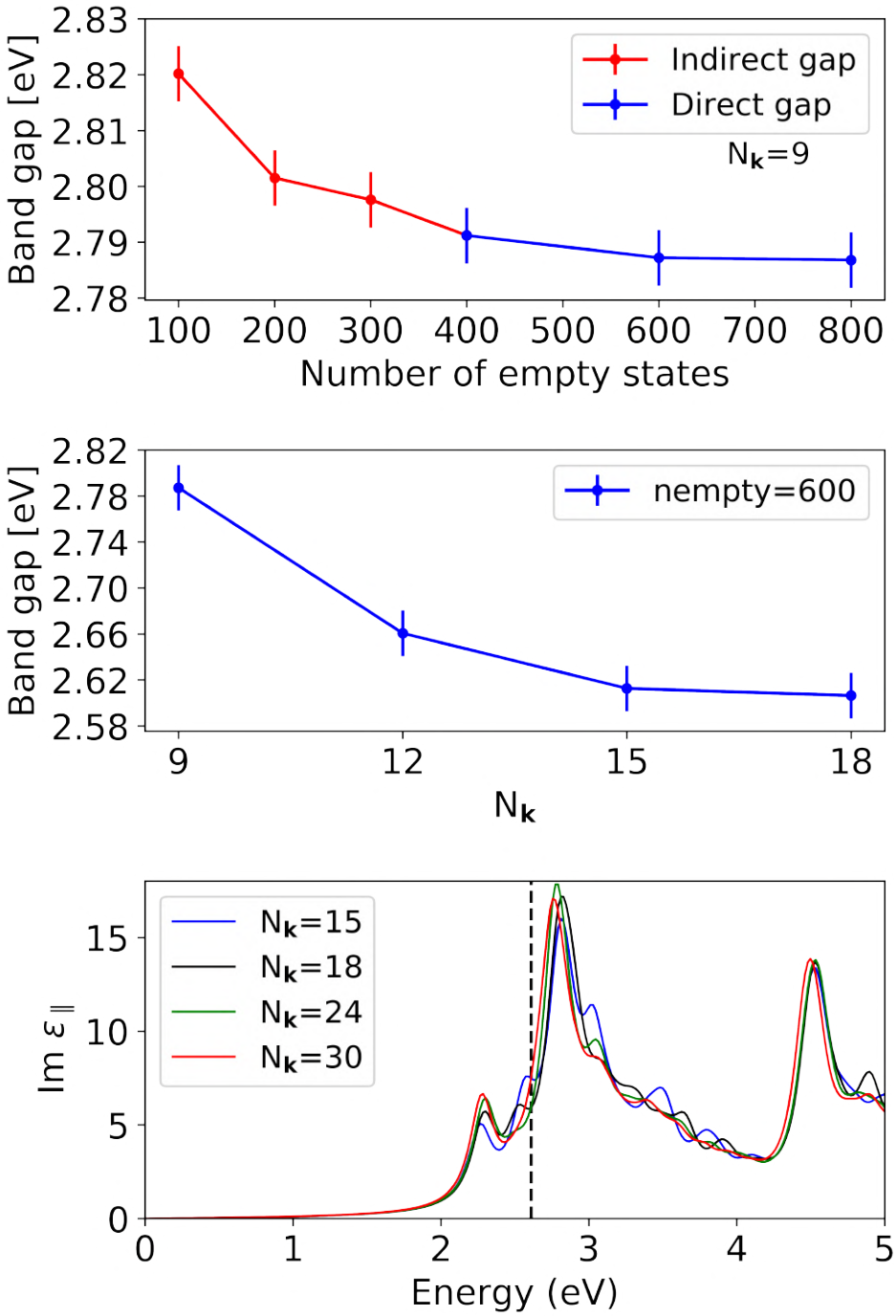

Figure B.2: Top: QP band gap of MoS_2 monolayer calculated as a function of empty states. The region where the gap is indirect ($\mathbf{K} \rightarrow \mathbf{Q}$), is indicated by the red line. $\mathbf{Q}$ is the point of the conduction-band minimum in bulk MoS_2. Employing 400 empty states or more a direct band gap at $\mathbf{K}$ is obtained. Middle panel: QP band gap of pristine MoS_2 ($\mathbf{K} \rightarrow \mathbf{K}$) calculated for different $\mathbf{k}$-grids. Bottom: Convergence of the imaginary part of the dielectric function with respect to $\mathbf{k}$-grid.

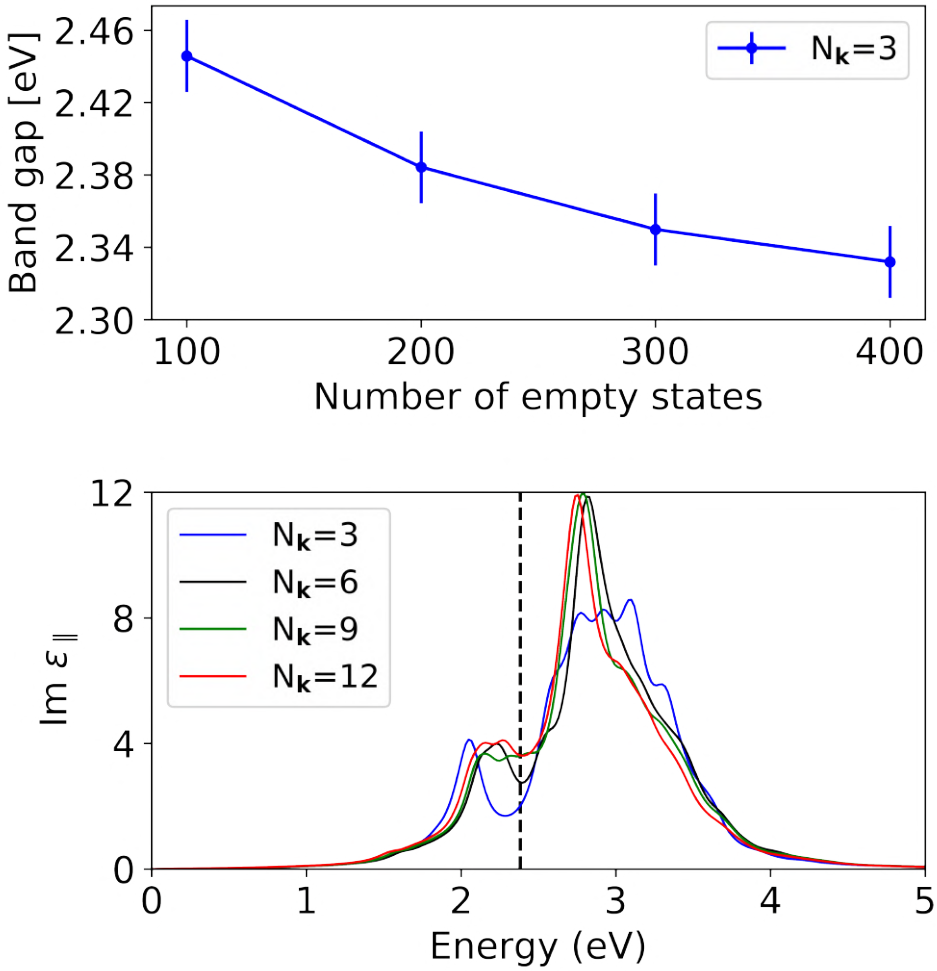

Figure B.3: The top panel shows the dependence of the fundamental QP band gap of pyrene@MoS_2 on the number of empty states included in the G_0W_0 calculations. The bottom panel depicts the imaginary part of the dielectric function computed for different **k**-grids.

B.1.2 Convergence of pyrene@MoS_2

For pyrene ($C_{16}H_{10}$) on top of the 3×3×1 MoS_2 supercell, PBE calculations are performed considering two different **k**-grids. The KS-PBE band gap changes by only 0.5 meV, *i.e.*, from 1.3041 eV to 1.3041 eV, upon going from a 3×3×1 to a 6×6×1 mesh. Due to the symmetry of the supercell, the direct band gap is folded to the **Γ** point of the BZ. Its dependence on the number of empty states is shown in the top panel of Fig. B.3. The bottom panel shows the in-plane component of the imaginary part of the dielectric function, obtained by the BSE, for different **k**-grids.

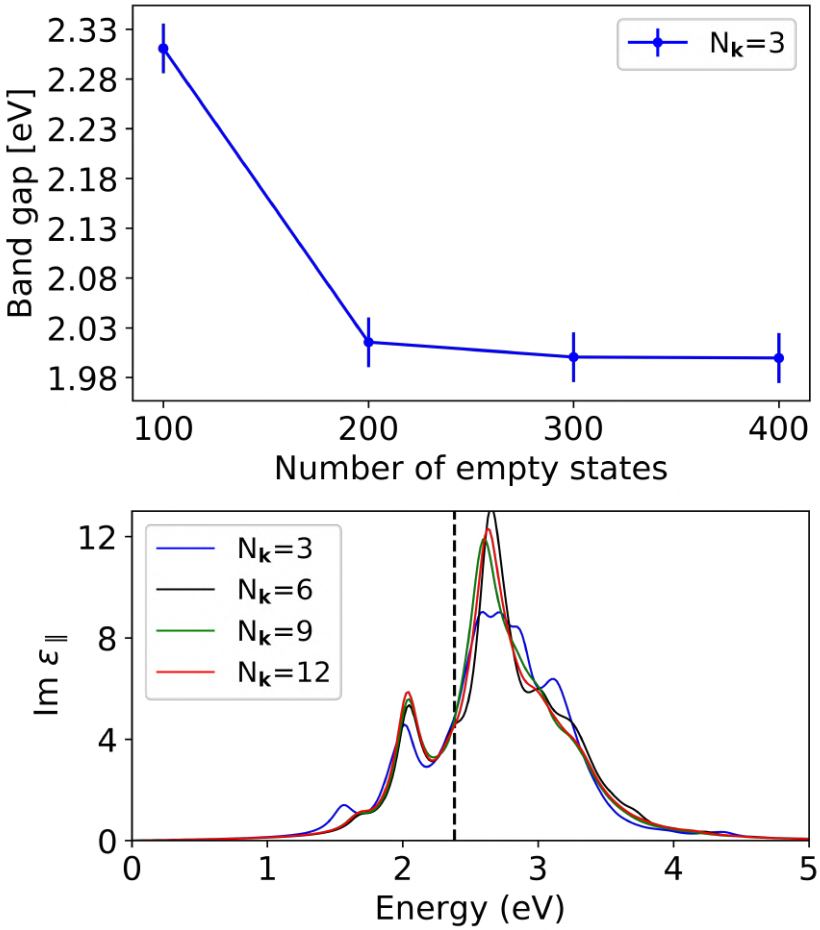

Figure B.4: The top panel shows the dependence of the fundamental QP band gap of pyridine@MoS_2 on the number of empty states included in the G_0W_0 calculations. The bottom panel depicts the imaginary part of the dielectric function computed for different **k**-grids.

B.1.3 Convergence of pyridine@MoS_2

For pyridine (C_5H_5N) on top of the 3×3×1 MoS_2 supercell, PBE calculations are performed considering two different **k**-grids. The KS band gap obtained by a 3×3×1 and a 6×6×1, mesh is 1.7048 and 1.7018, respectively. Due to symmetry of the supercell, the direct band gap is folded to the **Γ** point of the BZ. Its dependence on the number of empty states is shown in the top panel of Fig. B.4. The bottom panel depicts the in-plane component of the imaginary part of the dielectric function, obtained by the BSE, for different **k**-grids.

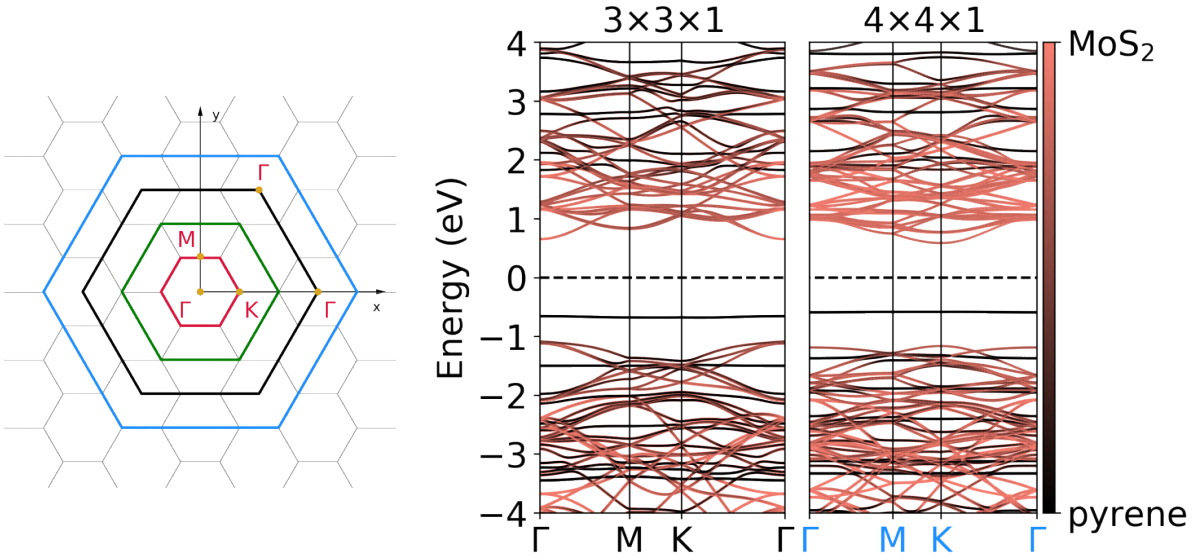

Figure B.5: Left: Brillouin zone folding in hexagonal crystals. The red hexagon represents the first BZ of a $m \times m$ supercell of the hexagonal crystal. The green, black and blue hexagons correspond to the first Brillouin zone of the unit cell of different m. In the case of green, it would mean a supercell of $m = 3n-1$, black, $m = 3n$, and blue, $m = 3n+1$, with n as an integer. The BZ of 2×2×1, 3×3×1, and 4×4×1 supercells correspond to a unit cell's BZ of green, black and blue, respectively. The figure has been adapted from Ref.[195]. Right: KS-PBE band structure of pyrene@MoS_2 for 2 supercell sizes. The bands are color coded corresponding to the inorganic (red) and organic (black) component. The color of the x-axis labels is corresponding to the BZ.

B.1.4 Impact of supercell size

Different supercells of the pristine MoS_2 monolayer are considered in order to investigate the level alignment. The left panel of Fig. B.5 shows the BZ and high-symmetry points of a 2×2×1, a 3×3×1,and a 4×4×1 supercell with green, black, and blue color, respectively. The KS-PBE band structure of pyrene@MoS_2 are shown in the right panel of Fig. B.5 for the 3×3×1 and 4×4×1 supercells. In the latter, the direct band gap is at the **K** point of the corresponding BZ (blue point in Fig. B.5). The variation in the HOMO energy is negligible when the supercell is increased. Also the fundamental band gap of the MoS_2 component is hardly affected and amounts to 1.7 eV. Consequently, for both supercells, PBE yields a type-II level alignment.

In Fig. B.6, the KS band structure of pyridine@MoS_2 is displayed for different supercells. The level alignment changes from type I to type II when the cell size is increased from 2×2×1 to 3×3×1. Like in pyrene@MoS_2, the fundamental band gap of the substrate remains unaffected. The molecular levels exhibit only minimal differences going

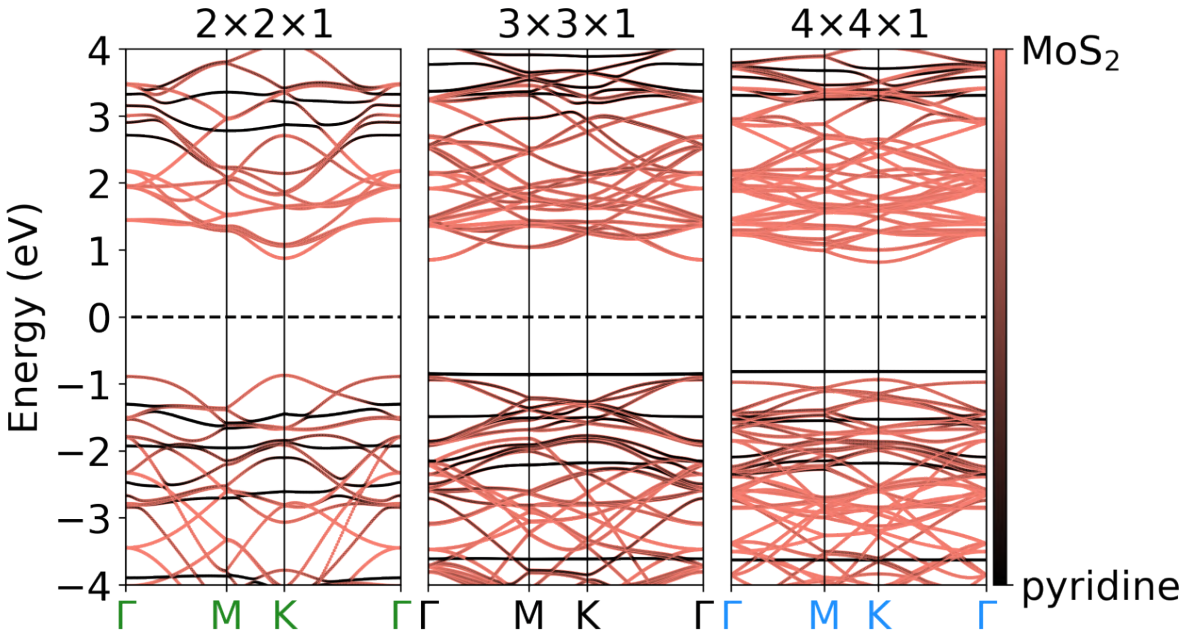

Figure B.6: KS band structure of pyridine@MoS_2 for different supercell sizes. The bands are color coded to highlight their atomic character. The color of the x-axis labels is corresponding to the BZ of Fig. B.5

from the 3×3×1 to the 4×4×1 case. As the situation is the same for the pyrene case, the 3×3×1 supercell was selected to study the optical properties of both heterostructures.

B.2 Numerical parameters of PTCDA@WSe_2

The MT spheres of the inorganic component are chosen to have equal radii of 2.2 bohr. For PTCDA, the radii are 0.9 bohr for hydrogen (H), 1.1 bohr for carbon (C), and 1.2 for oxygen (O). Following the definition in Eq. (5.1), we approximate this integral by a discrete sum over a finite number of fixed electron coordinates. For each electron position, the hole probability is computed on an evenly spaced, dense grid of 100×100×100 sampling points, covering a supercell of 9×9×1 supercells of the pristine WSe_2 unit cell. For the charge-transfer exciton, we sampled 60 positions on the PTCDA molecule (0.5 $Å^{-1}$ below and above the carbon and oxygen atoms) since its electronic contribution is almost entirely comprised of the LUMO. Similarly, we calculated the electron-hole correlation function of the WSe_2-exciton, sampling 16 positions close to the W atoms where we expect a high probability of finding the electron. The remaining parameters that are not explicitly defined here are assumed to be the same as those for pyrene@MoS_2.

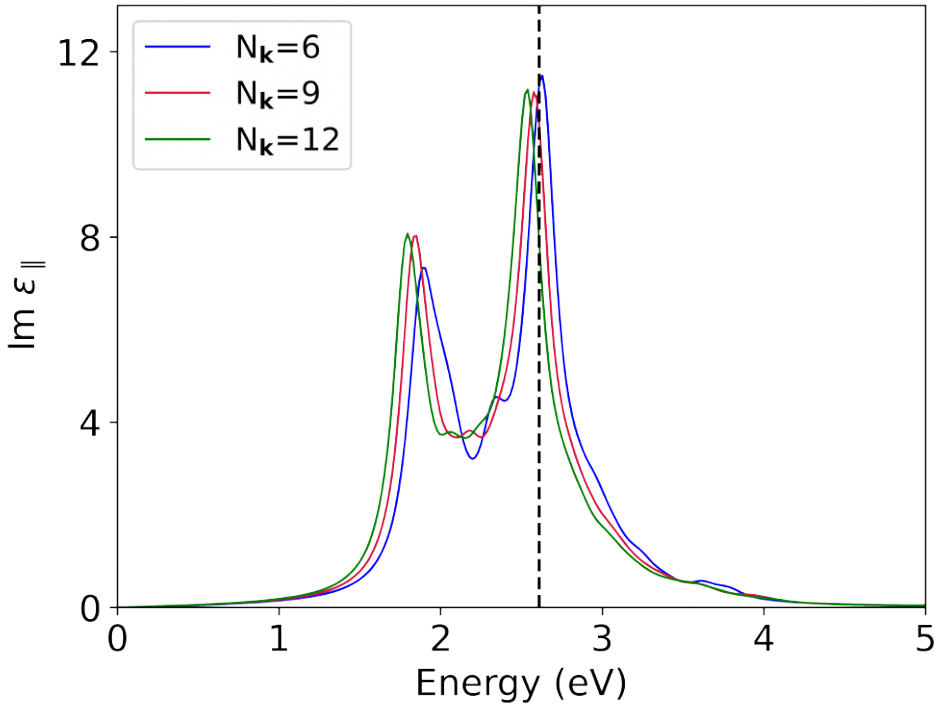

Figure B.7: Imaginary part of the dielectric function computed for different **k**-grids.

B.2.1 Convergence of PTCDA@WSe_2

For PTCDA on top of the 4×4×1 WSe_2 supercell, PBE calculations are performed considering two different **k**-grids. The KS band gap obtained by a 3×3×1 and a 6×6×1 mesh, is 1.220 and 1.221, respectively. The QP bands are computed using three different values for the number of empty bands, *i.e.*, 100, 200, and 300, obtaining a gap of 2.404, 2.235, and 2.204, respectively. Fig. B.7 depicts the in-plane component of the imaginary part of the dielectric function, obtained by BSE, for different **k**-grids.

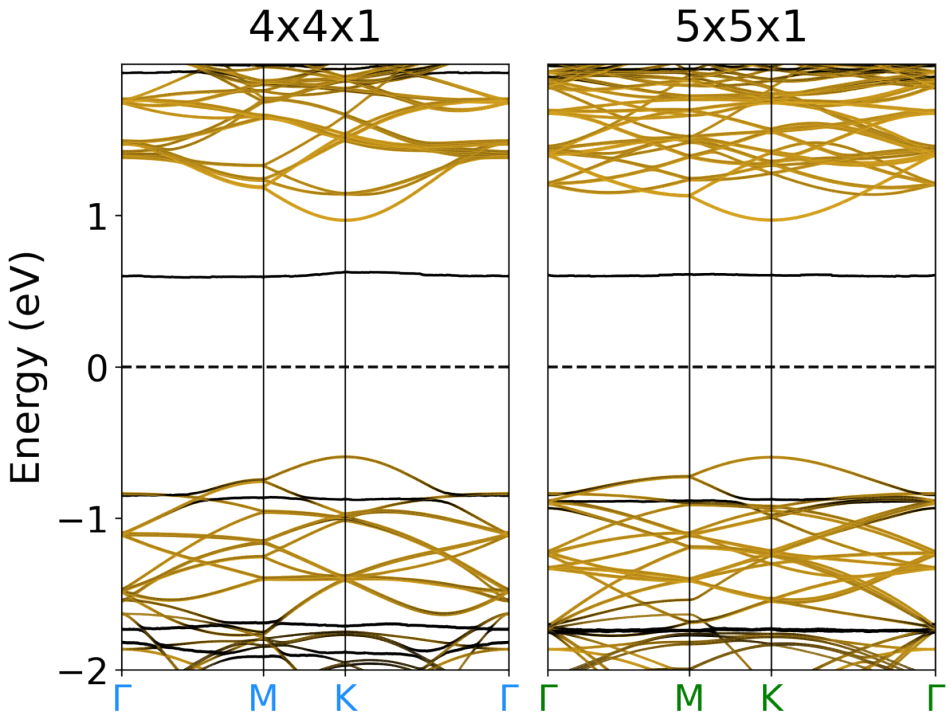

Figure B.8: KS band structure of PTCDA@WSe_2 for different supercell sizes. The bands are color coded to highlight their atomic character. The color of the x-axis labels is corresponding to the BZ of Fig. B.5. In the case of the 5×5×1 supercell is equivalent to the 2×2×1 case.

B.2.2 Impact of supercell size

In order to investigate the impact of the geometry and the level alignment, we consider two supercell sizes of PTCDA@WSe_2. The KS-PBE band structure is shown in Fig. B.8, the direct band gap is at the **K** point in both dispersions. The variation in the LUMO energy is negligible when the supercell is increased. Additionally the fundamental band gap of the WSe_2 component is hardly affected. In both cases, PBE yields a type-II level alignment.

C

Interpolation of the el-ph matrix elements

In this Appendix, we briefly summarize the Wannier-Fourier interpolation performed for the electron-phonon matrix elements. To properly evaluate the electron-phonon self-energy, as described in Eq. (1.44), the interpolation of the electron-phonon matrix elements is a must. The development of Wannier functions into the **exciting** code by Tillack *et al.*, [192, 193, 196] made accessible the exploitation of the spatial location in the Wannier representation to perform such interpolation into fine grids, *i.e.*, a large number of **k**- and **q**-points.

C.1 Wannier-Fourier interpolation of the matrix elements

In the construction of the electron-phonon matrix elements, first the electronic eigenstates and eigenvalues are computed by either DFT or the *GW* approximation. Then, the dynamical matrices and the potential response are obtained by either the supercell or density-functional perturbation theory (DFPT), leading to the calculation of the phonon eigenvector and frequencies. The calculation of the dynamical matrices is the most expensive part in the workflow, typically only the irreducible wedge of the BZ (IBZ) is calculated. However, we emphasized that working exclusively with the IBZ requires the rotation of the potential response due to crystal symmetries. For example, in diamond, the potential response is calculated for only one **X** point, to access the other two equivalent **X** points, the potential response must be rotated using the symmetries of the crystal.

In the case of (L)APW basis, the rotation must be applied to both the muffin-tin (MT) and the interstitial (I) part of the potential. A general expression of this rotation is the following, as shown in Ref. [74],

$$\partial V_{\mathcal{S}\mathbf{q}}(\mathbf{r}) = \partial V_{\mathbf{q}}(\{\mathcal{S}\mathbf{q}\}^{-1}\mathbf{r})\,. \tag{C.1}$$

After the potential response is accessible for the full BZ, the matrix elements are first calculated in the Bloch representation, subsequently they are transformed into the Wannier representation, as follows:

$$g_{mn\nu}(\mathbf{R}_\mathrm{e},\mathbf{R}_\mathrm{p}) = \frac{1}{N_\mathrm{e}N_\mathrm{p}}\sum_{\mathbf{k},\mathbf{q}}\left(\frac{1}{2M_\alpha\omega_{\mathbf{q}\nu}}\right)^{1/2} \mathrm{e}^{-\mathrm{i}(\mathbf{k}\cdot\mathbf{R}_\mathrm{e}+\mathbf{q}\cdot\mathbf{R}_\mathrm{p})} \times U^\dagger_{\mathbf{k}+\mathbf{q}}\, g_{mn\nu}(\mathbf{k},\mathbf{q})\, U_\mathbf{k}\, \mathbf{e}^{-1}_{\alpha\kappa\nu}(\mathbf{q}) \tag{C.2}$$

where N_e and N_p are the number of unit cells in the periodic supercell considered for the electronic and lattice dynamics, respectively. $U_\mathbf{k}$ and $U^\dagger_{\mathbf{k}+\mathbf{q}}$ are the unitary mixing matrices calculated after the generation of the Wannier functions, which are the essential ingredients for the transformation. Finally, $\mathbf{e}_{\alpha\kappa\nu}(\mathbf{q})$ and $\omega_{\mathbf{q}\nu}$ are the phonon eigenvector and phonon frequency, respectively.

In the case of polar materials, the long-range part of the electron-phonon matrix elements (see Eq.(1.40)) is subtracted before the interpolation to real space. This is a necessary step, otherwise, these quantities would not be localized and the interpolation would not be accurate. Once the matrix elements are transform from the real space to the fine grid (reciprocal space), the long-range term is added. The transformation of the Wannier representation to the Bloch representation is done as follows,

$$g_{mn\nu}(\mathbf{k},\mathbf{q}) = \sum_{\mathbf{R}_\mathrm{e},\mathbf{R}_\mathrm{p}}\left(\frac{1}{2M_\alpha\omega_{\mathbf{q}\nu}}\right)^{1/2} \mathrm{e}^{\mathrm{i}(\mathbf{k}\cdot\mathbf{R}_\mathrm{e}+\mathbf{q}\cdot\mathbf{R}_\mathrm{p})}\, U_{\mathbf{k}+\mathbf{q}}\, g_{mn\nu}(\mathbf{R}_\mathrm{e},\mathbf{R}_\mathrm{p})\, U^\dagger_\mathbf{k}\, \mathbf{e}_{\alpha\kappa,\nu}(\mathbf{q}) \tag{C.3}$$

As discussed by Giustino *et al.*, [74], the band and branch indices do not have any special meaning in the Wannier representation, in fact, the interpolation can be achieved by using the matrix elements in the atom and axis space, *i.e.*, α and κ, instead of the mode ν and $\mathbf{q}$-point space. The latter would just require to multiply the matrix elements in the fine grid times the phonon eigenvector (and prefactor). As final remarks, we discuss the gauge issue that might be encountered in this type of calculations. When the Wannier functions are generated and later on used to interpolate the matrix elements, the same set of electronic eigenvalues and eigenfunctions must be used. In the case of the

exciting code, this is not a problem, since the diagonalization of the Hamiltonian and the dynamical matrices are done in the same footing, even the QP eigenvalues can be use to construct both the Wannier functions and the electron-phonon matrix elements.

C.2 Electron-phonon matrix elements of selected materials

In order to validate the implementation of the interpolation of the matrix elements, we show three examples, first the case of diamond, second the case of SiC, which allows us to evaluate the procedure for the long-range part, and third for MoS_2 monolayer. As a reference we calculate the matrix elements with other code, which has direct access to the matrix elements without the need of interpolation. To account for degenerate electronic and phononic states, the matrix elements are averaged as follows,

$$|\overline{g_{mn\nu}}(\mathbf{k},\mathbf{q})| = \left(\frac{1}{MN\mathcal{N}}\right)\sum_{m}\sum_{n}\sum_{\nu}|g_{mn\nu}(\mathbf{k},\mathbf{q})|^2 \tag{C.4}$$

where M, N and $\mathcal{N}$ are the number of degenerates states for the initial and final electronic bands, and for the phonon modes, respectively.

C.2.1 Diamond

Figure C.1 (left) shows the electron and phonon dispersions for diamond. In the calculation of the matrix elements, the initial state is fixed at the VBM at the Γ-point (green dot). The final state corresponds to the valence band with highest energy over the path $\mathbf{L}\rightarrow\ \mathbf{\Gamma}\ \rightarrow\mathbf{X}\rightarrow\mathbf{W}\rightarrow\mathbf{K}\rightarrow\ \mathbf{\Gamma}$ (highlighted in blue in the electron dispersion). The phonon band consider corresponds to the branch with highest energy (highlighted in blue in the phonon dispersion). The right panel of Fig. C.1 shows the comparison of the averaged matrix elements calculated with **exciting** and other code. Overall, the averaged values are in good agreement.

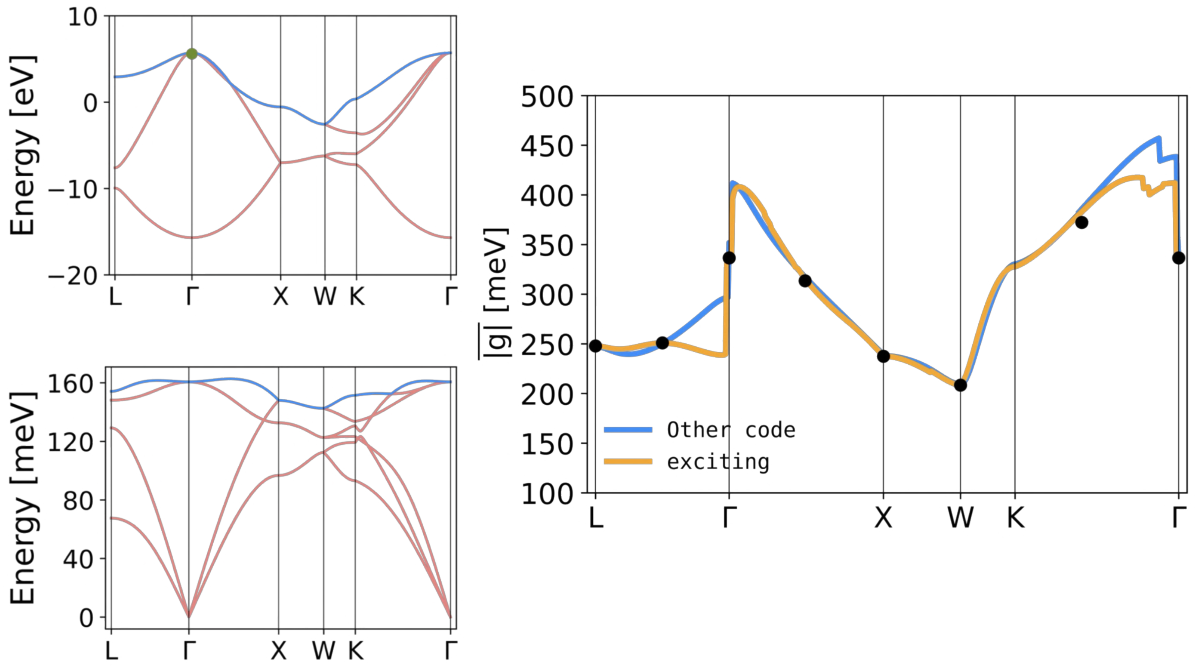

Figure C.1: Left: Electron and phonon dispersion for diamond. The matrix elements are calculated for the electronic and phononic branch highlighted in blue. The initial electronic state is represented by the green dot. Right: Averaged electron-phonon matrix elements calculated with **`exciting`** and other code. In the case of **`exciting`** the Wannier-Fourier interpolation is used. The black dots correspond to the matrix elements calculated in the coarse grid used in the interpolation.

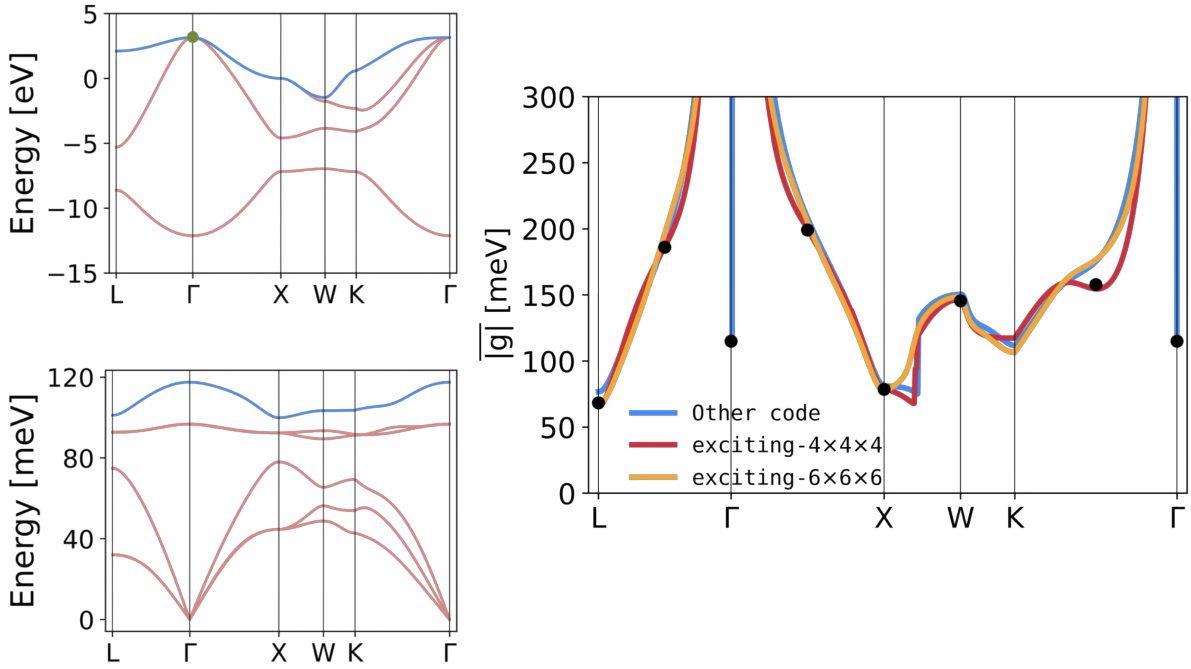

Figure C.2: Left: Electron and phonon dispersion for SiC. The matrix elements are calculated for the electronic and phononic branch highlighted in blue. The initial electronic state is represented by the green dot. Right: Averaged electron-phonon matrix elements calculated with **exciting** and other code. In the case of **exciting** the Wannier-Fourier interpolation is used. The black dots correspond to the matrix elements calculated in the coarse grid used in the interpolation.

C.2.2 SiC

We now compare the averaged matrix elements for the case of SiC, since this material is polar, the long-range part of the matrix elements is non-negligible. We validate our interpolation procedure by comparing the exact calculation for a phonon mode where the long-range is important. Figure C.2 (left panel) shows the electron and phonon dispersions. The latter is calculated considering the LO/TO splitting. The initial electronic state corresponds to the VBM at the $\mathbf{\Gamma}$ point (green dot), while the bands in blue are selected to calculated the averaged electron-phonon matrix elements (right panel). As expected, approaching the Γ-point the values diverge.

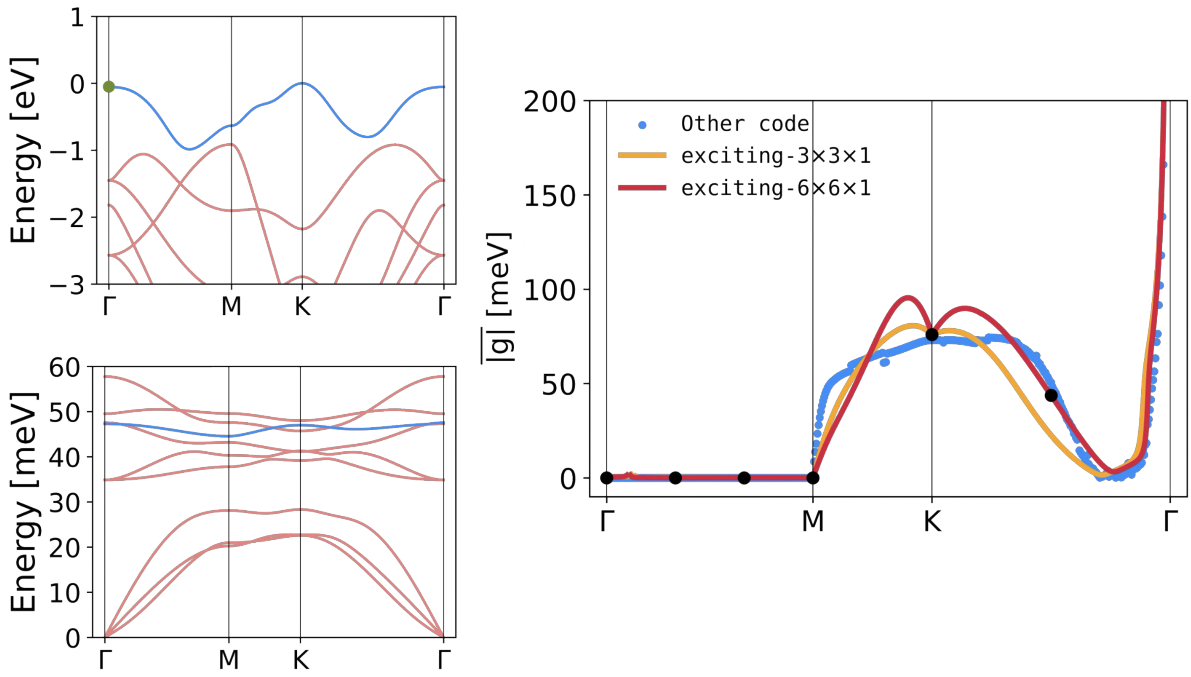

Figure C.3: Left: Electron and phonon dispersion for monolayer MoS_2. The matrix elements are calculated for the electronic and phononic branch highlighted in blue. The initial electronic state is represented by the green dot. Right: Averaged electron-phonon matrix elements calculated with **exciting** and other code. In the case of **exciting** the Wannier-Fourier interpolation is used. The black dots correspond to the matrix elements calculated in the coarse grid used in the interpolation.

C.2.3 MoS_2 monolayer

As a final example, we compare the averaged matrix elements of MoS_2 monolayer between **exciting** and our reference code. This material is not as polar as SiC, and the LO/TO splitting is not as pronounced. However, the E mode does play a role in the EPI of the system [127]. Figure C.3 (left panel) shows the electron and phonon dispersions for monolayer MoS_2. The matrix elements are calculated in the path $\mathbf{\Gamma} \rightarrow \mathbf{M} \rightarrow \mathbf{K} \rightarrow \mathbf{\Gamma}$. The averaged matrix elements (right panel Fig. C.3) shows the expected divergence in the direction of $\mathbf{K} \rightarrow \mathbf{\Gamma}$.

D

Many-body perturbation theory

In this Appendix we give a quick review of the Hedin's equation, which represent a systematic way to approximate the self-energy Σ and the Bethe-Salpeter equation (BSE) that describe two-particle excitations.

D.1 Hedin's equations

We show the closed set of equations, commonly referred to as Hedin's equations [104],

$$\Sigma(1,2) = \mathrm{i}\int \mathrm{d}(34)\, G(1,3)\,\Gamma(3,2,4)\,W(4,1^+)\,, \tag{D.1}$$

$$G(1,2) = G_0(1,2) + \int \mathrm{d}(34)\, G_0(1,3)\,\Sigma(3,4)\,G(4,2)\,, \tag{D.2}$$

$$\Gamma(1,2,3) = \delta(1,2)\,\delta(1,3) + \int \mathrm{d}(4567)\,\frac{\delta\Sigma(1,2)}{\delta G(4,5)}\,G(4,6)\,G(7,5)\,\Gamma(6,7,3)\,, \tag{D.3}$$

$$W(1,2) = v(1,2) + \int \mathrm{d}(34)\, v(1,3)\,P(3,4)\,W(4,2)\,, \tag{D.4}$$

$$P(1,2) = -\mathrm{i}\int \mathrm{d}(34)\, G(1,3)\,G(4,1^+)\,\Gamma(3,4,2)\,, \tag{D.5}$$

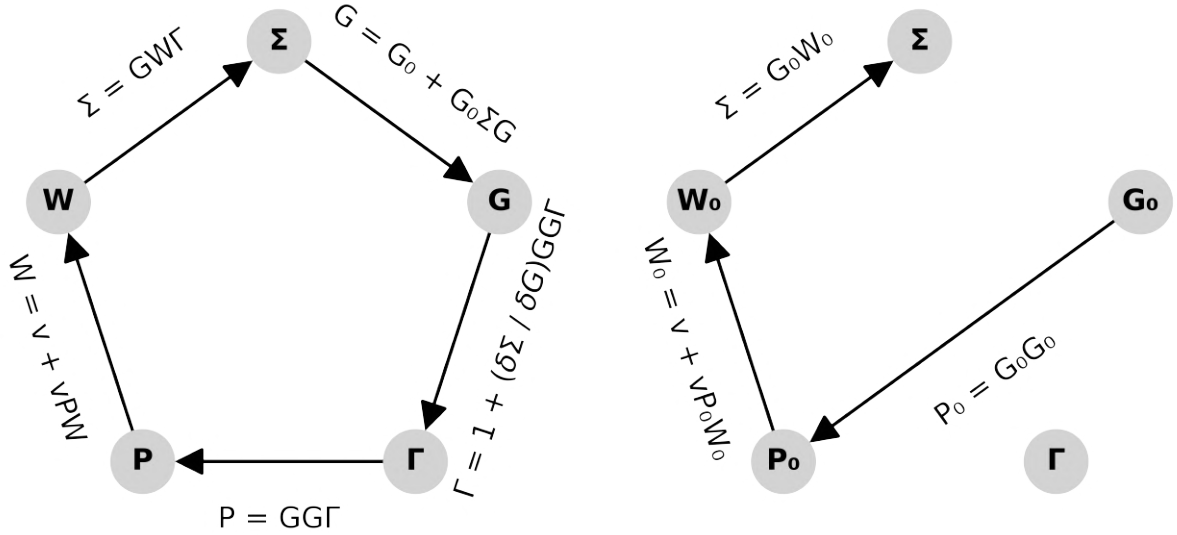

Figure D.1: Left: Pentangon scheme of the iterative solution of Hedin's equations. Right: In the G_0W_0 approximation, the iterative solution is reduced to one-round or one-shot calculation, with the following steps: $G_0 \to P_0 \to \epsilon \to W_0 \to \Sigma$. The vertex Γ is set to a product of delta functions.

where G is the single-particle Green's function, G_0 the independent-particle Green's function, P the irreducible polarizabilty, and W the screened Coulomb interaction. The notation "1^+" indicates that the corresponding time t_1 is infinitesimally later than the one of the combined index without the superscript.

To solve Hedin's equation, an iterative procedure is shown in the left panel of Fig. D.1. A fully iterative, self-consistent solution of Hedin's equation is not possible due to the complexity of the equations. In practice, we mention two main attempts to solve Hedin's equations. The simplest approach is to do a *one shot*, starting with $\Sigma = 0$ and stopping when $\Sigma = G_0W_0$ is computed. The latter is also known as the G_0W_0 approximation and is described in more detail in the Section 1.3.2. A more sophisticated approach would be a quasiparticle self-consistent *GW* (QSGW) [197, 198], where the iterative optimization of v_{xc} leads to the interacting G. In other words, each step of the cycle updates G_0, eventually converging to the solution closest to G. However, both the G_0W_0 and QSGW approaches ignore the vertex corrections by reducing the vertex function Γ to delta functions, *i.e.*,

$$\Gamma(1, 2, 3) = \delta(1, 2)\, \delta(1, 3)\,. \tag{D.6}$$

In general, neglecting the vertex correction is typically referred to as the *GW* approximation (GWA).

D.2 The Bethe-Salpeter equation

The state-of the-art for calculating optical properties is the Bethe-Salpeter equation (BSE) [61]. Processes involving two-particle excitations are written in terms of the two-particle Green's function, thus introducing a 4-point polarizability L

$$L(1,2,3,4) = L^0(1,2,3,4) - G(1,2,3,4)\,, \tag{D.7}$$

where L^0 is the independent-electron-hole polarizability

$$L^0(1,2,3,4) = -\mathrm{i}\,G(1,3)\,G(4,2)\,, \tag{D.8}$$

which describes the propagation of an electron and a hole separately. A more complete expression is as follows,

$$\begin{aligned} L(1,2,3,4) &= L^0(1,2,3,4) \\ &\quad + L^0(1,2,5,6)\left[v(5,7)\,\delta(5,6)\,\delta(7,8) + \mathrm{i}\,\frac{\delta\Sigma(5,6)}{\delta G(7,8)}\right] L(7,8,3,4) \end{aligned} \tag{D.9}$$

that can be rewritten as

$$L = L^0 + L^0\left(v + \mathrm{i}\,\frac{\delta\Sigma}{\delta G}\right) L\,. \tag{D.10}$$

The parenthesis in Eq. (D.10) is typically referred to as the kernel

$$\Xi = v + \mathrm{i}\,\frac{\delta\Sigma}{\delta G}\,, \tag{D.11}$$

which can be reduced by making use of the GW approximation, *i.e.*, the self-energy is approximated as the product of the Green's function and the screened Coulomb interaction, $\Sigma \approx \mathrm{i}GW$. The derivative is then simplified by

$$\frac{\delta(GW)}{\delta G} = W + G\,\frac{\delta W}{\delta G} \approx W\,, \tag{D.12}$$

where we have neglected the variation of the screening due to the excitation. A second approximation concerns the screened Coulomb interaction, W, where the *static limit* is used, meaning that we only calculate W at $\omega = 0$ [60, 199, 200].

List of publications

I. Gonzalez Oliva, F. Caruso, P. Pavone, and C. Draxl, "Hybrid excitations at the interface between a MoS_2 monolayer and organic molecules: A first-principle study". Phys. Rev. Mater. **6**, 054004-1 (2022).
DOI: https://doi.org/10.1103/PhysRevMaterials.6.054004

I. Gonzalez Oliva, B. Mauer, B. Alex, S. Tillack, M. Schebek, and C. Draxl, "Hybrid materials: Still challenging for *ab initio* theory?". Phys. Status Solidi A **221**, 2300170 (2023).
DOI: https://doi.org/10.1002/pssa.202300170

R. Rodriguez Pela, C. Vona, S. Lubeck, B. Alex, **I. Gonzalez Oliva**, and C. Draxl, "Critical assessment of G_0W_0 calculations for 2D materials: the example of monolayer MoS_2", npj Comput. Mater. **10**, 77 (2024).
DOI: https://doi.org/10.1038/s41524-024-01253-2

W. Bennecke, **I. Gonzalez Oliva**, J. P. Bange, P. Werner, D. Schmitt, M. Merboldt, A. Seiler, K. Watanabe, T. Taniguchi, D. Steil, R. Thomas Weitz, P. Puschnig, C. Draxl, G. S. Matthijs Jansen, M. Reutzel, and S. Mathias, "Hybrid Frenkel-Wannier excitons facilitate ultrafast energy transfer at a 2D-organic interface", *submitted*.
arXiv: https://arxiv.org/pdf/2411.14993.

Y. Jin, **I. Gonzalez Oliva**, H. Orio, G. Miao, M. Ünzelmann, J. Cojal González, A. Jocic, Y. Wang, X. Zhang, J. P. Rabe, K. Rossnagel, M. Kivala, C. Draxl, F. Reinert, and C.A. Palma, "Zero-energy band observation in an interfacial chalcogen-organic network", *submitted*.
arXiv: https://arxiv.org/pdf/2506.10555

M. Schebek, **I. Gonzalez Oliva**, and C. Draxl, "Efficient *GW* and BSE calculations of heterostructures within an all-electron framework", *in preparation*.

I. Gonzalez Oliva, S.Tillack, F.Caruso, P.Pavone, and C. Draxl, "Electron-phonon interactions at the interface between a MoS_2 monolayer and organic molecules", *in preparation.*

Acknowledgments

First and foremost, I would like to thank Prof. Dr. Dr. h.c. Claudia Draxl for giving me the opportunity to do this project. Initially, by supporting my application to the Deutsche Akademischer Austauschdienst (DAAD) and later on, for all the nice discussions and lessons that we had. Thank you to my co-supervisors Prof. Dr. Fabio Caruso and PD Dr. Pasquale Pavone for patiently respond all my doubts and teaching me about the theory and code. I would also like to thank Prof. Dr. Carlos Rudamas at Universidad de El Salvador, who was part of the reasons to pursue this path in academia and science.

Many thanks to Dr. Wahib Aggoune, who was my office mate during the first half of my PhD, with him I learned everything about **exciting** as a user. Our talks were not only about science, but in any topic, and I can honestly say that I am more knowledgeable thanks to him. Many thanks to (soon to be Dr.) Sebastian Tillack, who is an expert in **exciting**, the LAPW+lo basis, and the main developer of the electron-phonon code. Thank you, Sebastian, for your feedback and advices. During our time sharing an office, I managed to find motivation due to the fact that he was always available for discussions. In this regard, many thanks to (soon to be Dr.) Maximilian Schebek for dedicating time to finish the expansion addition project. He initially made most of the derivations presented in this work and was a vital part of the implementation and development of the code. I am very grateful for the nice discussions that Max and I had related to physics and beyond.

Many thanks to DAAD for financing the project entitled: Electron-phonon coupling and optical properties of hybrid inorganic organic systems (HIOS) for four years. Financial support from the Deutsche Forschungsgemeinschaft (DFG, German Research Foundation) via 182087777/SFB 951 (project B11) and the European Union's Horizon 2020 research and innovation program under the agreement No. 951786 (NOMAD CoE) is also acknowledged. To the SOL group at the Humboldt-Universität zu Berlin, a big thank you for your support.

I would like to thank my family for their support, Xenia, Griseida, Alfonso, Rosa, Marta and Ana Maria, without them nothing would be possible. Thank you to my

friends, Amanda, Alexander, Andrea, Leonardo, Sandra, and Karla for always listening and always finding words of motivation. Thank you to my friend Dr. Ana Maria for dedicating time to discuss and explore interesting ideas of condensed-matter physics. Thank you to my second family, Carla and Andrea, for always receiving me with open arms. Finally, I would like to thank my wife, Alexandra, for supporting me through good times and bad times. I acknowledge all your efforts and love.

References

[1] R. Otero, A. L. Vázquez de Parga, and J. M. Gallego, "Electronic, structural and chemical effects of charge-transfer at organic/inorganic interfaces," Surf. Sci. Rep. **72**, 105–145 (2017).

[2] Suyog Padgaonkar, Samuel H. Amsterdam, Hadallia Bergeron, Katherine Su, Tobin J. Marks, Mark C. Hersam, and Emily A. Weiss, "Molecular-orientation-dependent interfacial charge transfer in phthalocyanine/mos2 mixed-dimensional heterojunctions," J. Phys. Chem. C **123**, 13337–13343 (2019).

[3] Samuel H. Amsterdam, Teodor K. Stanev, Qunfei Zhou, Alexander J.-T. Lou, Hadallia Bergeron, Pierre Darancet, Mark C. Hersam, Nathaniel P. Stern, and Tobin J. Marks, "Electronic coupling in metallophthalocyanine–transition metal dichalcogenide mixed-dimensional heterojunctions," ACS Nano **13**, 4183–4190 (2019).

[4] Soohyung Park, Thorsten Schultz, Xiaomin Xu, Berthold Wegner, Areej Aljarb, Ali Han, Lain-Jong Li, Vincent C. Tung, Patrick Amsalem, and Norbert Koch, "Demonstration of the key substrate-dependent charge transfer mechanisms between monolayer mos2 and molecular dopants," Commun. Phys. **2**, 109 (2019).

[5] Madison C. Schwinn, Shahnawaz R. Rather, Changmin Lee, Matthew P. Bland, Thomas W. Song, Vinod K. Sangwan, Mark C. Hersam, and Lin X. Chen, "Charge transfer dynamics and interlayer exciton formation in MoS2/VOPc mixed dimensional heterojunction," J. Chem. Phys. **157**, 184701 (2022).

[6] Stephane Parola, Beatriz Julián-López, Luís D. Carlos, and Clément Sanchez, "Optical properties of hybrid organic-inorganic materials and their applications," Adv. Funct. Mater. **26**, 6506–6544 (2016).

[7] Soohyung Park, Niklas Mutz, Sergey A. Kovalenko, Thorsten Schultz, Dongguen Shin, Areej Aljarb, Lain Jong Li, Vincent Tung, Patrick Amsalem, Emil J.W. List-Kratochvil, Julia Stähler, Xiaomin Xu, Sylke Blumstengel, and Norbert Koch, "Type-I Energy Level Alignment at the PTCDA—Monolayer MoS2 Interface Promotes Resonance Energy Transfer and Luminescence Enhancement," Adv. Sci. **8**, 2100215 (2021).

[8] Gouri Chakraborty, In-Hyeok Park, Raghavender Medishetty, and Jagadese J. Vittal, "Two-dimensional metal-organic framework materials: Synthesis, structures, properties and applications," Chem. Rev. **121**, 3751–3891 (2021).

[9] R. Schlesinger, F. Bianchi, S. Blumstengel, C. Christodoulou, R. Ovsyannikov, B. Kobin, K. Moudgil, S. Barlow, S. Hecht, S. R. Marder, F. Henneberger, and N. Koch, "Efficient light emission from inorganic and organic semiconductor hybrid structures by energy-level tuning," Nat. Commun. **6**, 6754 (2015).

[10] Jakub Hagara, Nada Mrkyvkova, Peter Nádaždy, Martin Hodas, Michal Bodík, Matej Jergel, Eva Majková, Kamil Tokár, Peter Hutár, Michaela Sojková, Andrei Chumakov, Oleg Konovalov, Pallavi Pandit, Stephan Roth, Alexander Hinderhofer, Martin Hulman, Peter Siffalovic, and Frank Schreiber, "Reorientation of π-conjugated molecules on few-layer MoS2 films," Phys. Chem. Chem. Phys. **22**, 3097–3104 (2020).

[11] Benjamin Lowe, Bernard Field, Jack Hellerstedt, Julian Ceddia, Henry L. Nourse, Ben J. Powell, Nikhil V. Medhekar, and Agustin Schiffrin, "Local gate control of mott metal-insulator transition in a 2d metal-organic framework," Nat. Commun. **15**, 3559 (2024).

[12] Dhaneesh Kumar, Jack Hellerstedt, Bernard Field, Benjamin Lowe, Yuefeng Yin, Nikhil V. Medhekar, and Agustin Schiffrin, "Manifestation of strongly correlated electrons in a 2d kagome metal–organic framework," Adv. Funct. Mater. .

[13] Daniel Baranowski, Marco Thaler, Dominik Brandstetter, Andreas Windischbacher, Iulia Cojocariu, Simone Mearini, Valeria Chesnyak, Luca Schio, Luca Floreano, Carolina Gutiérrez Bolaños, Peter Puschnig, Laerte L. Patera, Vitaliy Feyer, and Claus M. Schneider, "Emergence of band structure in a two-dimensional metal–organic framework upon hierarchical self-assembly," ACS Nano **18**, 19618–19627 (2024).

[14] X.-Y. Zhu, "Electronic structure and electron dynamics at molecule–metal interfaces: implications for molecule-based electronics," Surf. Sci. Rep. **56**, 1–83 (2004).

[15] Michael Hollerer, Daniel Lüftner, Philipp Hurdax, Thomas Ules, Serguei Soubatch, Frank Stefan Tautz, Georg Koller, Peter Puschnig, Martin Sterrer, and Michael G. Ramsey, "Charge transfer and orbital level alignment at inorganic/organic interfaces: The role of dielectric interlayers," ACS Nano **11**, 6252–6260 (2017).

[16] Yifeng Chen, Isaac Tamblyn, and Su Ying Quek, "Energy level alignment at hybridized organic–metal interfaces: The role of many-electron effects," J. Phys. Chem. C **121**, 13125–13134 (2017).

[17] Jaehoon Ji and Jong Hyun Choi, "Recent progress in 2d hybrid heterostructures from transition metal dichalcogenides and organic layers: properties and applications in energy and optoelectronics fields," Nanoscale **14**, 10648–10689 (2022).

[18] Yu Jing, Xin Tan, Zhen Zhou, and Panwen Shen, "Tuning electronic and optical properties of MoS2 monolayer via molecular charge transfer," J. Mater. Chem. A **2**, 16892–16897 (2014).

[19] Kangli Wang and Beate Paulus, "Tuning the binding energy of excitons in the MoS2monolayer by molecular functionalization and defective engineering," Phys. Chem. Chem. Phys. **22**, 11936–11942 (2020).

[20] Niklas Mutz, Soohyung Park, Thorsten Schultz, Sergey Sadofev, Simon Dalgleish, Louisa Reissig, Norbert Koch, Emil J.W. List-Kratochvil, and Sylke Blumstengel, "Excited-State Charge Transfer Enabling MoS2/Phthalocyanine Photodetectors with Extended Spectral Sensitivity," J. Phys. Chem. C **124**, 2837–2843 (2020).

[21] Ruben Canton-Vitoria, Yuman Sayed-Ahmad-baraza, Bernard Humbert, Raul Arenal, Christopher P. Ewels, and Nikos Tagmatarchis, "Pyrene coating transition metal disulfides as protection from photooxidation and environmental aging," Nanomaterials **10**, 363 (2020).

[22] Asieh Yousofnejad, Gaël Reecht, Nils Krane, Christian Lotze, and Katharina J. Franke, "Monolayers of MoS2 on Ag(111) as decoupling layers for organic molecules: Resolution of electronic and vibronic states of TCNQ," Beilstein J. Nanotechnol. **11**, 1062–1071 (2020).

[23] Yichen Jin, Ignacio Gonzalez Oliva, Hibiki Orio, Guangyao Miao, Maximilian Ünzelmann, José D. Cojal González, Angelina Jocic, Yan Wang, Xiaoxi Zhang, Jürgen P. Rabe, Kai Rossnagel, Milan Kivala, Claudia Draxl, Friedrich Reinert, and Carlos-Andres Palma, "Zero-energy band observation in an interfacial chalcogen-organic network," (2025), arXiv:2506.10555 [physics.chem-ph] .

[24] Vigneshwaran Shanmugam, Rhoda Afriyie Mensah, Karthik Babu, Sidique Gawusu, Avishek Chanda, Yongming Tu, Rasoul Esmaeely Neisiany, Michael Försth, Gabriel Sas, and Oisik Das, "A review of the synthesis, properties, and applications of 2d materials," Particle & Particle Systems Characterization **39**, 2200031 (2022).

[25] Ganesh R. Bhimanapati, Zhong Lin, Vincent Meunier, Yeonwoong Jung, Judy Cha, Saptarshi Das, Di Xiao, Youngwoo Son, Michael S. Strano, Valentino R. Cooper, Liangbo Liang, Steven G. Louie, Emilie Ringe, Wu Zhou, Steve S. Kim, Rajesh R. Naik, Bobby G. Sumpter, Humberto Terrones, Fengnian Xia, Yeliang Wang, Jun

Zhu, Deji Akinwande, Nasim Alem, Jon A. Schuller, Raymond E. Schaak, Mauricio Terrones, and Joshua A. Robinson, "Recent advances in two-dimensional materials beyond graphene," ACS Nano **9**, 11509–11539 (2015).

[26] Hua Zhang, "Introduction: 2d materials chemistry," Chem. Rev. **118**, 6089–6090 (2018).

[27] Sajedeh Manzeli, Dmitry Ovchinnikov, Diego Pasquier, Oleg V. Yazyev, and Andras Kis, "2D transition metal dichalcogenides," Nat. Rev. Mat. **2**, 17033 (2017).

[28] Ashwin Ramasubramaniam, "Large excitonic effects in monolayers of molybdenum and tungsten dichalcogenides," Phys. Rev. B **86**, 115409 (2012).

[29] Andrea Splendiani, Liang Sun, Yuanbo Zhang, Tianshu Li, Jonghwan Kim, Chi-Yung Chim, Giulia Galli, and Feng Wang, "Emerging Photoluminescence in Monolayer MoS_2," Nano Lett. **10**, 1271–1275 (2010).

[30] Dongxue Chen, Zhen Lian, Xiong Huang, Ying Su, Mina Rashetnia, Li Yan, Mark Blei, Takashi Taniguchi, Kenji Watanabe, Sefaattin Tongay, Zenghui Wang, Chuanwei Zhang, Yong Tao Cui, and Su Fei Shi, "Tuning moiré excitons and correlated electronic states through layer degree of freedom," Nat. Commun. **13**, 4810 (2022).

[31] A Chaves, Javad G Azadani, Hussain Alsalman, DR Da Costa, R Frisenda, AJ Chaves, Seung Hyun Song, Young Duck Kim, Daowei He, Jiadong Zhou, *et al.*, "Bandgap engineering of two-dimensional semiconductor materials," npj 2D Mater. Appl. **4**, 29 (2020).

[32] Alejandro Molina-Sánchez, Davide Sangalli, Kerstin Hummer, Andrea Marini, and Ludger Wirtz, "Effect of spin-orbit interaction on the optical spectra of single-layer, double-layer, and bulk MoS2," Phys. Rev. B **88**, 045412 (2013).

[33] Alejandro Molina-Sánchez, Kerstin Hummer, and Ludger Wirtz, "Vibrational and optical properties of MoS2: From monolayer to bulk," Surf. Sci. Rep. **70**, 554–586 (2015).

[34] Diana Y. Qiu, Felipe H. da Jornada, and Steven G. Louie, "Optical Spectrum of MoS_2: Many-Body Effects and Diversity of Exciton States," Phys. Rev. Lett. **111**, 216805 (2013).

[35] Diana Y. Qiu, Felipe H. da Jornada, and Steven G. Louie, "Screening and many-body effects in two-dimensional crystals: Monolayer MoS_2," Phys. Rev. B **93**, 235435 (2016).

[36] Fabio Caruso, " Nonequilibrium Lattice Dynamics in Monolayer MoS 2 ," J. Phys. Chem. Lett. **12**, 1734–1740 (2021).

[37] Xiao Liu, Jie Gu, Kan Ding, Dejiu Fan, Xiaoer Hu, Yu Wen Tseng, Yi Hsien Lee, Vinod Menon, and Stephen R. Forrest, "Photoresponse of an Organic Semiconductor/Two-Dimensional Transition Metal Dichalcogenide Heterojunction," Nano Lett. **17**, 3176–3181 (2017).

[38] Yu Huang, Fuwei Zhuge, Junxian Hou, Liang Lv, Peng Luo, Nan Zhou, Lin Gan, and Tianyou Zhai, "Van der Waals Coupled Organic Molecules with Monolayer MoS2 for Fast Response Photodetectors with Gate-Tunable Responsivity," ACS Nano **12**, 4062–4073 (2018).

[39] Soohyung Park, Haiyuan Wang, Thorsten Schultz, Dongguen Shin, Ruslan Ovsyannikov, Marios Zacharias, Dmitrii Maksimov, Matthias Meissner, Yuri Hasegawa, Takuma Yamaguchi, Satoshi Kera, Areej Aljarb, Mariam Hakami, Lain Jong Li, Vincent Tung, Patrick Amsalem, Mariana Rossi, and Norbert Koch, "Temperature-dependent electronic ground-state charge transfer in van der waals heterostructures," Adv. Mater. **33**, 2100215 (2021).

[40] Samuel Brem, Christopher Linderälv, Paul Erhart, and Ermin Malic, "Tunable phases of moiré excitons in van der waals heterostructures," Nano Lett. **20**, 8534–8540 (2020).

[41] Tika R. Kafle, Bhupal Kattel, Samuel D. Lane, Ti Wang, Hui Zhao, and Wai Lun Chan, "Charge transfer exciton and spin flipping at organic-transition-metal dichalcogenide interfaces," ACS Nano **11**, 10184–10192 (2017).

[42] Tika R. Kafle, Bhupal Kattel, Peng Yao, Peymon Zereshki, Hui Zhao, and Wai Lun Chan, "Effect of the interfacial energy landscape on photoinduced charge generation at the znpc/mos2 interface," J. Am. Chem. Soc. **141**, 11328–11336 (2019).

[43] Jie Gu, Xiao Liu, Erh-chen Lin, Yi-Hsien Lee, Stephen R. Forrest, and Vinod M. Menon, "Dipole-aligned energy transfer between excitons in two-dimensional transition metal dichalcogenide and organic semiconductor," ACS Photonics **5**, 100–104 (2018).

[44] Wiebke Bennecke, Ignacio Gonzalez Oliva, Jan Philipp Bange, Paul Werner, David Schmitt, Marco Merboldt, Anna M. Seiler, Kenji Watanabe, Takashi Taniguchi, Daniel Steil, R. Thomas Weitz, Peter Puschnig, Claudia Draxl, G. S. Matthijs Jansen, Marcel Reutzel, and Stefan Mathias, "Hybrid frenkel-wannier excitons facilitate ultrafast energy transfer at a 2d-organic interface," (2024), arXiv:2411.14993 [cond-mat.mes-hall] .

[45] Claudia Draxl, Dmitrii Nabok, and Karsten Hannewald, "Organic/inorganic hybrid materials: Challenges for ab initio methodology," Acc. Chem. Res. **47**, 3225–3232 (2014).

[46] Oliver T. Hofmann, Egbert Zojer, Lukas Hörmann, Andreas Jeindl, and Reinhard J. Maurer, "First-principles calculations of hybrid inorganic-organic interfaces: From state-of-the-art to best practice," Phys. Chem. Chem. Phys. **23**, 8132–8180 (2021).

[47] Ignacio Gonzalez Oliva, Benedikt Maurer, Ben Alex, Sebastian Tillack, Maximilian Schebek, and Claudia Draxl, "Hybrid materials: Still challenging for ab initio theory?" Phys. Status Solidi A **221**, 2300170 (2023).

[48] Fengyuan Xuan, Yifeng Chen, and Su Ying Quek, "Quasiparticle levels at large interface systems from many-body perturbation theory: The xaf-gw method," J. Chem. Theory. Comput. **15**, 3824–3835 (2019).

[49] Zhen Fei Liu, Felipe H. Da Jornada, Steven G. Louie, and Jeffrey B. Neaton, "Accelerating GW-Based Energy Level Alignment Calculations for Molecule-Metal Interfaces Using a Substrate Screening Approach," J. Chem. Theory. Comput. **15**, 4218–4227 (2019).

[50] Shiyuan Gao, Li Yang, and Catalin D. Spataru, "Interlayer coupling and gate-tunable excitons in transition metal dichalcogenide heterostructures," Nano Lett. **17**, 7809–7813 (2017).

[51] M. Palummo, A. N. D'Auria, J. C. Grossman, and G. Cicero, "Tailoring the optical properties of MoS2 and WS2 single layers via organic functionalization," J. Phys. Condens. Matter. **31**, 235701 (2019).

[52] Kangli Wang and Beate Paulus, "Toward a comprehensive understanding of oxygen on mos2: From reaction to optical properties," J. Phys. Chem. C **125**, 19544–19550 (2021).

[53] Olugbenga Adeniran and Zhen Fei Liu, "Quasiparticle electronic structure of phthalocyanine:tmd interfaces from first-principles gw," J. Chem. Phys. **155**, 214702 (2021).

[54] Ignacio Gonzalez Oliva, Fabio Caruso, Pasquale Pavone, and Claudia Draxl, "Hybrid excitations at the interface between a mos_2 monolayer and organic molecules: A first-principles study," Phys. Rev. Mater. **6**, 054004–1 (2022).

[55] Joseph Frimpong and Zhen Fei Liu, "Generalized substrate screening gw for covalently bonded interfaces," J. Phys. Chem. Lett. **15**, 2133–2141 (2024).

[56] Walter Kohn and L. J. Sham, "Self-consistent equations including exchange and correlation effects," Phys. Rev. **140**, A1133 (1965).

[57] Richard M. Martin, *Electronic Structure: Basic Theory and Practical Methods* (Cambridge University Press, 2004).

[58] Mark S. Hybertsen and Steven G. Louie, "Electron correlation in semiconductors and insulators: Band gaps and quasiparticle energies," Phys. Rev. B **34**, 5390–5413 (1986).

[59] G. Strinati, "Application of the Green's functions method to the study of the optical properties of semiconductors," La Rivista Del Nuovo Cimento Series 3 **11**, 1–86 (1988).

[60] Giovanni Onida, Lucia Reining, and Angel Rubio, "Electronic excitations: density-functional versus many-body Green's-function approaches," Rev. Mod. Phys. **74**, 601–659 (2002).

[61] Richard M. Martin, Lucia Reining, and David M. Ceperley, *Interacting Electrons: Theory and Computational Approaches* (Cambridge University Press, 2016).

[62] J. B. Neaton, Mark S. Hybertsen, and Steven G. Louie, "Renormalization of molecular electronic levels at metal-molecule interfaces," Phys. Rev. Lett. **97**, 216405 (2006).

[63] L. Romaner, D. Nabok, P. Puschnig, E. Zojer, and C. Ambrosch-Draxl, "Theoretical study of ptcda adsorbed on the coinage metal surfaces, ag(111), au(111) and cu(111)," New. J. Phys. **11**, 053010 (2009).

[64] Peter Puschnig, Peiman Amiri, and Claudia Draxl, "Band renormalization of a polymer physisorbed on graphene investigated by many-body perturbation theory," Phys. Rev. B **86**, 085107 (2012).

[65] Yu Jie Zheng, Yu Li Huang, Yifeng Chen, Weijie Zhao, Goki Eda, Catalin D. Spataru, Wenjing Zhang, Yung Huang Chang, Lain Jong Li, Dongzhi Chi, Su Ying Quek, and Andrew Thye Shen Wee, "Heterointerface screening effects between organic monolayers and monolayer transition metal dichalcogenides," ACS Nano **10**, 2476–2484 (2016).

[66] Wahib Aggoune, *Optical excitations of selected van der Waals heterostructures investigated by many-body perturbation theory*, Ph.D. thesis, Université A. Mira-Bejaia (2018).

[67] Wahib Aggoune, Caterina Cocchi, Dmitrii Nabok, Karim Rezouali, Mohamed Akli Belkhir, and Claudia Draxl, "Structural, electronic, and optical properties of periodic graphene/h-BN van der Waals heterostructures," Phys. Rev. Mater. **4**, 84001 (2020).

[68] Olga Turkina, Dmitrii Nabok, Andris Gulans, Caterina Cocchi, and Claudia Draxl, "Electronic and Optical Excitations at the Pyridine/ZnO(101¯0) Hybrid Interface," Adv. Theory Simul. **2**, 1800108 (2019).

[69] Lukas Gierster, Olga Turkina, Jan-Christoph Deinert, Sesha Vempati, Elsie Baeta, Yves Garmshausen, Stefan Hecht, Claudia Draxl, and Julia Stähler, "Right on time: Ultrafast charge separation before hybrid exciton formation," Adv. Sci. **11**, 2403765 (2024).

[70] Lukas Eschmann, Jan Neuendorf, and Michael Rohlfing, "Impact of electron-phonon interaction on metal-organic interface states," Phys. Rev. B **104**, L241102 (2021).

[71] Lukas Eschmann, Jan Neuendorf, and Michael Rohlfing, "Graphene and ntcda adsorbed on ag(111): Temperature-dependent binding distance and phonon coupling to the interface state," Phys. Rev. B **104**, 245403 (2021).

[72] M. Cardona, "Renormalization of the optical response of semiconductors by electron–phonon interaction," Phys. Status Solidi A **188**, 1209–1232 (2001).

[73] Peter Y. Yu and Manuel Cardona, *Fundamentals of Semiconductors* (Springer Berlin, Heidelberg, 2010).

[74] Feliciano Giustino, Marvin Cohen, and Steven Louie, "Electron-phonon interaction using wannier functions," Phys. Rev. B **76**, 165108–1 (2007).

[75] Feliciano Giustino, *Materials Modelling Using Density Functional Theory: Properties and Predictions* (Oxford University Press, 2014).

[76] Carla Verdi and Feliciano Giustino, "Fröhlich electron-phonon vertex from first principles," Phys. Rev. Lett. **115**, 176401 (2015).

[77] Feliciano Giustino, "Electron-phonon interactions from first principles," Rev. Mod. Phys. **89**, 015003–1 (2017).

[78] Mark S. Hybertsen and Steven G. Louie, "First-principles theory of quasiparticles: Calculation of band gaps in semiconductors and insulators," Phys. Rev. Lett. **55**, 1418–1421 (1985).

[79] Felix Henneke, Lin Lin, Christian Vorwerk, Claudia Draxl, Rupert Klein, and Chao Yang, "Fast optical absorption spectra calculations for periodic solid state systems," Comm. App. Math. Comp. Sci. **15**, 89–113 (2020).

[80] Jianfeng Lu and Lexing Ying, J. Comp. Phys. **302**, 329–335 (2015).

[81] Jianfeng Lu and Lexing Ying, Ann. Math. Sci. Appl. **1**, 321–339 (2016).

[82] Hong Jiang, Ricardo I. Gómez-Abal, Xin-Zheng Li, Christian Meisenbichler, Claudia Ambrosch-Draxl, and Matthias Scheffler, "FHI-gap: A GW code based on the all-electron augmented plane wave method," Comput. Phys. Commun. **184**, 348–366 (2013).

[83] Dmitrii Nabok, Andris Gulans, and Claudia Draxl, "Accurate all-electron G_0W_0 quasiparticle energies employing the full-potential augmented planewave method," Phys. Rev. B **94**, 035118 (2016).

[84] Xinguo Ren, Patrick Rinke, Volker Blum, Jürgen Wieferink, Alexandre Tkatchenko, Andrea Sanfilippo, Karsten Reuter, and Matthias Scheffler, "Resolution-of-identity approach to Hartree-Fock, hybrid density functionals, RPA, MP2 and GW with numeric atom-centered orbital basis functions," New. J. Phys. **14**, 053020 (2012).

[85] Teresa M. Figueira-Duarte and Klaus Müllen, "Pyrene-based materials for organic electronics," Chem. Rev. **111**, 7260–7314 (2011).

[86] Noa Marom, Fabio Caruso, Xinguo Ren, Oliver T. Hofmann, Thomas Körzdörfer, James R. Chelikowsky, Angel Rubio, Matthias Scheffler, and Patrick Rinke, "Benchmark of *GW* methods for azabenzenes," Phys. Rev. B **86**, 245127 (2012).

[87] Oliver T. Hofmann and Patrick Rinke, "Band bending engineering at organic/inorganic interfaces using organic self-assembled monolayers," Adv. Energy Mater. **3**, 1600373 (2017).

[88] Alejandro Núñez-López, Ramón Torres-Cavanillas, Marc Morant-Giner, Natalia Vassilyeva, Richard Mattana, Sergio Tatay, Philippe Ohresser, Edwige Otero, Emiliano Fonda, Michael Paulus, Víctor Rubio-Giménez, Alicia Forment-Aliaga, and Eugenio Coronado, "Hybrid heterostructures of a spin crossover coordination polymer on mos2: Elucidating the role of the 2d substrate," Small **19**, 2304954 (2023).

[89] Che-Hsuan Cheng, Zidong Li, Aaditya Hambarde, and Parag B. Deotare, "Efficient energy transfer across organic–2d inorganic heterointerfaces," ACS Appl. Mater. Interfaces **10**, 39336–39342 (2018).

[90] Sk Md Obaidulla, Mohammad Rezwan Habib, Yahya Khan, Yuhan Kong, Tao Liang, and Mingsheng Xu, "Mos2 and perylene derivative based type-ii heterostructure: Bandgap engineering and giant photoluminescence enhancement," Ad. Mater. Interfaces **7**, 1901197 (2020).

[91] Mohammad Rezwan Habib, Hongfei Li, Yuhan Kong, Tao Liang, Sk Md Obaidulla, Shuang Xie, Shengping Wang, Xiangyang Ma, Huanxing Su, and Mingsheng Xu, "Tunable photoluminescence in a van der waals heterojunction built from a mos2 monolayer and a ptcda organic semiconductor," Nanoscale **10**, 16107–16115 (2018).

[92] John M. Ziman, *Electrons and Phonons: The Theory of Transport Phenomena in Solids* (Oxford University Press, 2001).

[93] Andris Gulans, Stefan Kontur, Christian Meisenbichler, Dmitrii Nabok, Pasquale Pavone, Santiago Rigamonti, Stephan Sagmeister, Ute Werner, and Claudia Draxl, "exciting: a full-potential all-electron package implementing density-functional theory and many-body perturbation theory," J. Phys. Condens. Matter. **26**, 363202 (2014).

[94] Friedhelm Bechstedt, *Many-Body Approach to Electronic Excitations* (Springer Berlin, Heidelberg, 2015).

[95] Max Born and Robert Oppenheimer, "Zur quantentheorie der molekeln," Ann. Phys. **389**, 457–484 (1927).

[96] Pierre Hohenberg and Walter Kohn, "Inhomogeneous electron gas," Phys. Rev. **136**, B864 (1964).

[97] John P. Perdew and Karla Schmidt, "Jacob's ladder of density functional approximations for the exchange-correlation energy," AIP Conference Proceedings **577**, 1–20 (2001).

[98] John P. Perdew, Adrienn Ruzsinszky, Jianmin Tao, Viktor N. Staroverov, Gustavo E. Scuseria, and Gábor I. Csonka, "Prescription for the design and selection of density functional approximations: More constraint satisfaction with fewer fits," J. Chem. Phys. **123**, 062201 (2005).

[99] John P. Perdew, Kieron Burke, and Matthias Ernzerhof, "Generalized gradient approximation made simple," Phys. Rev. Lett. **77**, 3865–3868 (1996).

[100] Yu-ichiro Matsushita, Kazuma Nakamura, and Atsushi Oshiyama, "Comparative study of hybrid functionals applied to structural and electronic properties of semiconductors and insulators," Phys. Rev. B **84**, 075205 (2011).

[101] Cecilia Vona, Dmitrii Nabok, and Claudia Draxl, "Electronic structure of (organic-)inorganic metal halide perovskites: The dilemma of choosing the right functional," Adv. Theory Simul. **5**, 2100496 (2022).

[102] Jochen Heyd, Gustavo E. Scuseria, and Matthias Ernzerhof, "Hybrid functionals based on a screened Coulomb potential," J. Chem. Phys. **118**, 8207–8215 (2003).

[103] Jochen Heyd, Gustavo E. Scuseria, and Matthias Ernzerhof, "Erratum: "Hybrid functionals based on a screened Coulomb potential" [J. Chem. Phys. 118, 8207 (2003)]," J. Chem. Phys. **124**, 219906 (2006).

[104] Lars Hedin, "New method for calculating the one-particle Green's function with application to the electron-gas problem," Phys. Rev. **139**, A796 (1965).

[105] John C. Taylor, "Tamm-dancoff method," Phys. Rev. **95**, 1313–1317 (1954).

[106] Stefano Baroni, Stefano De Gironcoli, Andrea Dal Corso, and Paolo Giannozzi, "Phonons and related crystal properties from density-functional perturbation theory," Rev. Mod. Phys. **73**, 515–562 (2001).

[107] Xavier Gonze and Changyol Lee, "Dynamical matrices, born effective charges, dielectric permittivity tensors, and interatomic force constants from density-functional perturbation theory," Phys. Rev. B **55**, 10355–10368 (1997).

[108] David J. Singh and Lars Nordström, *Planewaves, Pseudopotentials, and the LAPW Method* (Springer New York, NY, 2005).

[109] Andris Gulans, Anton Kozhevnikov, and Claudia Draxl, "Microhartree precision in density functional theory calculations," Phys. Rev. B **97**, 161105 (2018).

[110] Kurt Lejaeghere, Gustav Bihlmayer, Torbjörn Björkman, Peter Blaha, Stefan Blügel, Volker Blum, Damien Caliste, Ivano E. Castelli, Stewart J. Clark, Andrea Dal Corso, Stefano de Gironcoli, Thierry Deutsch, John Kay Dewhurst, Igor Di Marco, Claudia Draxl, Marcin Dułak, Olle Eriksson, José A. Flores-Livas, Kevin F. Garrity, Luigi Genovese, Paolo Giannozzi, Matteo Giantomassi, Stefan Goedecker, Xavier Gonze, Oscar Grånäs, E. K. U. Gross, Andris Gulans, François Gygi, D. R. Hamann, Phil J. Hasnip, N. A. W. Holzwarth, Diana Iuşan, Dominik B. Jochym, François Jollet, Daniel Jones, Georg Kresse, Klaus Koepernik, Emine Küçükbenli, Yaroslav O. Kvashnin, Inka L. M. Locht, Sven Lubeck, Martijn Marsman, Nicola Marzari, Ulrike Nitzsche, Lars Nordström, Taisuke Ozaki, Lorenzo Paulatto, Chris J. Pickard, Ward Poelmans, Matt I. J. Probert, Keith Refson, Manuel Richter, Gian-Marco Rignanese, Santanu Saha, Matthias Scheffler, Martin Schlipf, Karlheinz Schwarz, Sangeeta Sharma, Francesca Tavazza, Patrik Thunström, Alexandre Tkatchenko, Marc Torrent, David Vanderbilt, Michiel

J. van Setten, Veronique Van Speybroeck, John M. Wills, Jonathan R. Yates, Guo-Xu Zhang, and Stefaan Cottenier, "Reproducibility in density functional theory calculations of solids," Science **351**, aad3000 (2016).

[111] Christian Vorwerk, Benjamin Aurich, Caterina Cocchi, and Claudia Draxl, "Bethe–Salpeter equation for absorption and scattering spectroscopy: implementation in the exciting code," Electron. Struct. **1**, 037001 (2019).

[112] E Sjöstedt, L Nordström, and D.J Singh, "An alternative way of linearizing the augmented plane-wave method," Solid State Communications **114**, 15–20 (2000).

[113] Mara-Antonia Voiculescu, *Exploiting Symmetry in the (L)APW+LO Method*, Master's thesis, Humboldt-Universität zu Berlin (2025).

[114] Carlo A. Rozzi, Daniele Varsano, Andrea Marini, Eberhard K. U. Gross, and Angel Rubio, "Exact coulomb cutoff technique for supercell calculations," Phys. Rev. B **73**, 205119 (2006).

[115] Sohrab Ismail-Beigi, "Truncation of periodic image interactions for confined systems," Phys. Rev. B **73**, 233103 (2006).

[116] Filip A. Rasmussen and Kristian S. Thygesen, "Computational 2D Materials Database: Electronic Structure of Transition-Metal Dichalcogenides and Oxides," J. Phys. Chem. C **119**, 13169–13183 (2015).

[117] Filip A Rasmussen, Per S Schmidt, Kirsten T Winther, and Kristian S Thygesen, "Efficient many-body calculations for two-dimensional materials using exact limits for the screened potential: Band gaps of MoS_2, h-BN, and phosphorene," Phys. Rev. B **94**, 155406 (2016).

[118] Sten Haastrup, Mikkel Strange, Mohnish Pandey, Thorsten Deilmann, Per S Schmidt, Nicki F Hinsche, Morten N Gjerding, Daniele Torelli, Peter M Larsen, Anders C Riis-Jensen, Jakob Gath, Karsten W Jacobsen, Jens Jørgen Mortensen, Thomas Olsen, and Kristian S Thygesen, "The computational 2d materials database: high-throughput modeling and discovery of atomically thin crystals," 2D Mater. **5**, 042002 (2018).

[119] Ben Alex, *Efficient Screening in Many-Body Calculations for Low-Dimensional Materials*, Master's thesis, Humboldt-Universität zu Berlin (2024).

[120] Alexandre Tkatchenko and Matthias Scheffler, "Accurate molecular van der Waals interactions from ground-state electron density and free-atom reference data," Phys. Rev. Lett. **102**, 073005 (2009).

[121] Alexandre Tkatchenko, Lorenz Romaner, Oliver T. Hofmann, Egbert Zojer, Claudia Ambrosch-Draxl, and Matthias Scheffler, "Van der waals interactions between organic adsorbates and at organic/inorganic interfaces," MRS Bulletin **35**, 435–442 (2010).

[122] F. L. Hirshfeld, "Bonded-atom fragments for describing molecular charge densities," Theoretica chimica acta **44**, 129–138 (1977).

[123] A.J. Stone, *The Theory of Intermolecular Forces* (Oxford University Press, 1996).

[124] Jongmin Kim, *Ab initio study of work function modification at organic/metal interfaces*, Ph.D. thesis, Humboldt-Universität zu Berlin (2024).

[125] Kin Fai Mak, Changgu Lee, James Hone, Jie Shan, and Tony F. Heinz, "Atomically thin mos2: A new direct-gap semiconductor," Phys. Rev. Lett. **105**, 136805 (2010).

[126] Sanjoy K. Mahatha, Arlette S. Ngankeu, Nicki Frank Hinsche, Ingrid Mertig, Kevin Guilloy, Peter L. Matzen, Marco Bianchi, Charlotte E. Sanders, Jill A. Miwa, Harsh Bana, Elisabetta Travaglia, Paolo Lacovig, Luca Bignardi, Daniel Lizzit, Rosanna Larciprete, Alessandro Baraldi, Silvano Lizzit, and Philip Hofmann, "Electron–phonon coupling in single-layer mos2," Surf. Sci. **681**, 64–69 (2019).

[127] Alejandro Molina-Sánchez, Kerstin Hummer, and Ludger Wirtz, "Vibrational and optical properties of MoS_2: From monolayer to bulk," Surf. Sci. Rep. **70**, 554–586 (2015).

[128] A. Molina-Sánchez and L. Wirtz, "Phonons in single-layer and few-layer mos_2 and ws_2," Phys. Rev. B **84**, 155413 (2011).

[129] Alejandro Molina-Sánchez, Maurizia Palummo, Andrea Marini, and Ludger Wirtz, "Temperature-dependent excitonic effects in the optical properties of single-layer MoS_2," Phys. Rev. B **93**, 155435 (2016), 1604.00943 .

[130] Neha Nayyar, Duy Le, Volodymyr Turkowski, and Talat S. Rahman, "Electron-phonon interaction and ultrafast photoemission from doped monolayer mos2," Phys. Chem. Chem. Phys. **24**, 25298–25306 (2022).

[131] Fabio Caruso, Maximilian Schebek, Yiming Pan, Cecilia Vona, and Claudia Draxl, "Chirality of Valley Excitons in Monolayer Transition-Metal Dichalcogenides," J. Phys. Chem. C **13**, 5894–5899 (2022).

[132] Qing Tang and De-en Jiang, "Stabilization and band-gap tuning of the 1t-mos2 monolayer by covalent functionalization," Chem. Mater. **27**, 3743–3748 (2015).

[133] A. Steinhoff, M. Rösner, F. Jahnke, T. O. Wehling, and C. Gies, "Influence of excited carriers on the optical and electronic properties of mos2," Nano Lett. **14**, 3743–3748 (2014).

[134] Hongliang Shi, Hui Pan, Yong Wei Zhang, and Boris I. Yakobson, "Quasiparticle band structures and optical properties of strained monolayer mos_2 and ws_2," Phys. Rev. B **87**, 155304 (2013).

[135] Ronaldo Rodrigues Pela, Cecilia Vona, Sven Lubeck, Ben Alex, Ignacio Gonzalez Oliva, and Claudia Draxl, "Critical assessment of g0w0 calculations for 2d materials: the example of monolayer mos2," npj Comput. Mater. **10**, 77 (2024).

[136] Nourdine Zibouche, Martin Schlipf, and Feliciano Giustino, "GW band structure of monolayer MoS_2 using the SternheimerGW method and effect of dielectric environment," Phys. Rev. B **103**, 125401 (2021).

[137] Falco Hüser, Thomas Olsen, and Kristian S. Thygesen, "How dielectric screening in two-dimensional crystals affects the convergence of excited-state calculations: Monolayer MoS_2," Phys. Rev. B **88**, 245309 (2013).

[138] Yang-hao Chan, Jonah B. Haber, Mit H. Naik, Jeffrey B. Neaton, Diana Y. Qiu, Felipe H. da Jornada, and Steven G. Louie, "Exciton lifetime and optical line width profile via exciton–phonon interactions: Theory and first-principles calculations for monolayer mos2," Nano Lett. **23**, 3971–3977 (2023).

[139] Michele Pisarra, Cristina Diáz, and Fernando Martín, "Theoretical study of structural and electronic properties of 2H-phase transition metal dichalcogenides," Phys. Rev. B **103**, 195416 (2021).

[140] A. Thilagam, "Exciton formation assisted by longitudinal optical phonons in monolayer transition metal dichalcogenides," J. Appl. Phys. **120**, 124306 (2016).

[141] Marco Bernardi, Maurizia Palummo, and Jeffrey C. Grossman, "Extraordinary sunlight absorption and one nanometer thick photovoltaics using two-dimensional monolayer materials," Nano Lett. **13**, 3664–3670 (2013).

[142] Roland Gillen and Janina Maultzsch, "Light-Matter Interactions in Two-Dimensional Transition Metal Dichalcogenides: Dominant Excitonic Transitions in Mono-and Few-Layer MoX_2 and Band Nesting," IEEE J. Quantum Electron. **23**, 219–230 (2016).

[143] J. P. Echeverry, B. Urbaszek, T. Amand, X. Marie, and I. C. Gerber, "Splitting between bright and dark excitons in transition metal dichalcogenide monolayers," Phys. Rev. B **93**, 121107 (2016).

[144] Per S Schmidt, Christopher E Patrick, and Kristian S Thygesen, "Simple vertex correction improves GW band energies of bulk and two-dimensional crystals," Phys. Rev. B **96**, 205206 (2017).

[145] Houlong L Zhuang and Richard G Hennig, "Computational search for single-layer transition-metal dichalcogenide photocatalysts," J. Phys. Chem. C **117**, 20440–20445 (2013).

[146] Hannu-Pekka Komsa and Arkady V. Krasheninnikov, "Effects of confinement and environment on the electronic structure and exciton binding energy of MoS_2 from first principles," Phys. Rev. B **86**, 241201 (2012).

[147] Yufeng Liang, Shouting Huang, Ryan Soklaski, and Li Yang, "Quasiparticle band-edge energy and band offsets of monolayer of molybdenum and tungsten chalcogenides," Appl. Phys. Lett. **103**, 042106 (2013).

[148] Ryan Soklaski, Yufeng Liang, Changjian Zhang, Haining Wang, Farhan Rana, and Li Yang, "Temperature effect on optical spectra of monolayer molybdenum disulfide," Appl. Phys. Lett. **104**, 193110 (2014).

[149] Morten Niklas Gjerding, Alireza Taghizadeh, Asbjørn Rasmussen, Sajid Ali, Fabian Bertoldo, Thorsten Deilmann, Nikolaj Rørbæk Knøsgaard, Mads Kruse, Ask Hjorth Larsen, Simone Manti, Thomas Garm Pedersen, Urko Petralanda, Thorbjørn Skovhus, Mark Kamper Svendsen, Jens Jørgen Mortensen, Thomas Olsen, and Kristian Sommer Thygesen, "Recent progress of the computational 2d materials database (c2db)," 2D Mater. **8**, 044002 (2021).

[150] Han-gyu Kim and Hyoung Joon Choi, "Thickness dependence of work function, ionization energy, and electron affinity of mo and w dichalcogenides from dft and gw calculations," Phys. Rev. B **103**, 085404 (2021).

[151] C. Ataca and S. Ciraci, "Functionalization of single-layer mos2 honeycomb structures," J. Phys. Chem. C **115**, 13303–13311 (2011).

[152] Tyler J. Smart, Feng Wu, Marco Govoni, and Yuan Ping, "Fundamental principles for calculating charged defect ionization energies in ultrathin two-dimensional materials," Phys. Rev. Mater. **2**, 124002 (2018).

[153] Xiang Jiang, Qijing Zheng, Zhenggang Lan, Wissam A. Saidi, Xinguo Ren, and Jin Zhao, "Real-time *GW*-BSE investigations on spin-valley exciton dynamics in monolayer transition metal dichalcogenide," Sci. Adv. **7**, eabf3759 (2021).

[154] Jun Kang, Sefaattin Tongay, Jian Zhou, Jingbo Li, and Junqiao Wu, "Band offsets and heterostructures of two-dimensional semiconductors," Appl. Phys. Lett. **102**, 012111 (2013).

[155] Jason K. Ellis, Melissa J. Lucero, and Gustavo E. Scuseria, "The indirect to direct band gap transition in multilayered MoS_2 as predicted by screened hybrid density functional theory," Appl. Phys. Lett. **99**, 261908 (2011).

[156] Iris Niehues, Robert Schmidt, Matthias Drüppel, Philipp Marauhn, Dominik Christiansen, Malte Selig, Gunnar Berghäuser, Daniel Wigger, Robert Schneider, Lisa Braasch, Rouven Koch, Andres Castellanos-Gomez, Tilmann Kuhn, Andreas Knorr, Ermin Malic, Michael Rohlfing, Steffen Michaelis de Vasconcellos, and Rudolf Bratschitsch, "Strain control of exciton–phonon coupling in atomically thin semiconductors," Nano Lett. **18**, 1751–1757 (2018).

[157] Mingu Kang, Sung Won Jung, Woo Jong Shin, Yeongsup Sohn, Sae Hee Ryu, Timur K. Kim, Moritz Hoesch, and Keun Su Kim, "Holstein polaron in a valley-degenerate two-dimensional semiconductor," Nat. Mater. **17**, 676–680 (2018).

[158] J. Kopaczek, S. Zelewski, K. Yumigeta, R. Sailus, S. Tongay, and R. Kudrawiec, "Temperature dependence of the indirect gap and the direct optical transitions at the high-symmetry point of the brillouin zone and band nesting in mos2, mose2, mote2, ws2, and wse2crystals," J. Phys. Chem. C **126**, 5665–5674 (2022).

[159] Hyeokjae Kwon, Sourav Garg, Ji Hoon Park, Yeonsu Jeong, Sanghyuck Yu, Seongsin M. Kim, Patrick Kung, and Seongil Im, "Monolayer MoS2 field-effect transistors patterned by photolithography for active matrix pixels in organic light-emitting diodes," npj 2D Mater. Appl. **3**, 9 (2019).

[160] Tristan L. Britt, Qiuyang Li, Laurent P. René De Cotret, Nicholas Olsen, Martin Otto, Syed Ali Hassan, Marios Zacharias, Fabio Caruso, Xiaoyang Zhu, and Bradley J. Siwick, "Direct view of phonon dynamics in atomically thin mos2," Nano Lett. **22**, 4718–4724 (2022).

[161] T. Korn, S. Heydrich, M. Hirmer, J. Schmutzler, and C. Schller, "Low-temperature photocarrier dynamics in monolayer mos2," Appl. Phys. Lett. **99**, 102109 (2011).

[162] B. Radisavljevic, A. Radenovic, J. Brivio, V. Giacometti, and A. Kis, "Single-layer MoS_2 transistors," Nature Nanotechnol. **6**, 147–150 (2011).

[163] Th. Böker, R. Severin, A. Müller, C. Janowitz, R. Manzke, D. Voß, P. Krüger, A. Mazur, and J. Pollmann, "Band structure of MoS_2, $MoSe_2$, and α-$MoTe_2$: Angle-resolved photoelectron spectroscopy and ab initio calculations," Phys. Rev. B **64**, 235305 (2001).

[164] Volker Blum, Ralf Gehrke, Felix Hanke, Paula Havu, Ville Havu, Xinguo Ren, Karsten Reuter, and Matthias Scheffler, "Ab initio molecular simulations with numeric atom-centered orbitals," Comput. Phys. Commun. **180**, 2175–2196 (2009).

[165] A. R. Klots, A. K. M. Newaz, Bin Wang, D. Prasai, H. Krzyzanowska, Junhao Lin, D. Caudel, N. J. Ghimire, J. Yan, B. L. Ivanov, K. A. Velizhanin, A. Burger, D. G. Mandrus, N. H. Tolk, S. T. Pantelides, and K. I. Bolotin, "Probing excitonic states in suspended two-dimensional semiconductors by photocurrent spectroscopy," Sci. Rep. **4**, 6608 (2014).

[166] Margherita Marsili, Alejandro Molina-Sánchez, Maurizia Palummo, Davide Sangalli, and Andrea Marini, "Spinorial formulation of the GW -BSE equations and spin properties of excitons in two-dimensional transition metal dichalcogenides," Phys. Rev. B **103**, 155152 (2021).

[167] Changpeng Lin, Samuel Poncé, and Nicola Marzari, "General invariance and equilibrium conditions for lattice dynamics in 1d, 2d, and 3d materials," npj Comput. Mater. **8**, 236 (2022).

[168] Marios Zacharias and Feliciano Giustino, "Theory of the special displacement method for electronic structure calculations at finite temperature," Phys. Rev. Res. **2**, 013357 (2020).

[169] Yanping Guo, Linlu Wu, Jinghao Deng, Linwei Zhou, Wei Jiang, Shuangzan Lu, Da Huo, Jiamin Ji, Yusong Bai, Xiaoyu Lin, Shunping Zhang, Hongxing Xu, Wei Ji, and Chendong Zhang, "Band alignment and interlayer hybridization in monolayer organic/wse2 heterojunction," Nano Res. **15**, 1276–1281 (2022).

[170] A. M. Valencia and M. J. Caldas, "Single vacancy defect in graphene: Insights into its magnetic properties from theoretical modeling," Phys. Rev. B **96**, 125431 (2017).

[171] Dmitrii Nabok, Benjamin Höffling, and Claudia Draxl, "Energy-Level Alignment at Organic/Inorganic Interfaces from First Principles: Example of Poly(paraphenylene)/Rock-Salt ZnO(100)," Chem. Mater. **31**, 7143–7150 (2019).

[172] Kristian S. Thygesen and Angel Rubio, "Renormalization of molecular quasiparticle levels at metal-molecule interfaces: Trends across binding regimes," Phys. Rev. Lett. **102**, 046802 (2009).

[173] Fabio Caruso, Matthias Dauth, Michiel J. Van Setten, and Patrick Rinke, "Benchmark of GW Approaches for the GW100 Test Set," J. Chem. Theory. Comput. **12**, 5076–5087 (2016).

[174] Matthias Dauth, Fabio Caruso, Stephan Kümmel, and Patrick Rinke, "Piecewise linearity in the GW approximation for accurate quasiparticle energy predictions," Phys. Rev. B **93**, 121115(R) (2016).

[175] Noa Marom, "Accurate description of the electronic structure of organic semiconductors by GW methods," J. Phys. Condens. Matter. **29**, 103003 (2017).

[176] Ignacio Gonzalez Oliva, Benedikt Maurer, Ben Alex, Sebastian Tillack, Maximilian Schebek, and Claudia Draxl, "Hybrid materials: Still challenging for ab initio theory?" Phys. Status Solidi (A) **221**, 2300170 (2024).

[177] Wahib Aggoune, Caterina Cocchi, Dmitrii Nabok, Karim Rezouali, Mohamed Akli Belkhir, and Claudia Draxl, "Dimensionality of excitons in stacked van der waals materials: The example of hexagonal boron nitride," Phys. Rev. B **97**, 241114 (2018).

[178] Fabio Caruso, Carla Verdi, Samuel Poncé, and Feliciano Giustino, "Electron-plasmon and electron-phonon satellites in the angle-resolved photoelectron spectra of n-doped anatase tio_2," Phys. Rev. B **97**, 165113 (2018).

[179] Sahar Sharifzadeh, Pierre Darancet, Leeor Kronik, and Jeffrey B. Neaton, "Low-energy charge-transfer excitons in organic solids from first-principles: The case of pentacene," J. Phys. Chem. Lett. **4**, 2197–2201 (2013).

[180] David Schmitt, Jan Philipp Bange, Wiebke Bennecke, AbdulAziz AlMutairi, Giuseppe Meneghini, Kenji Watanabe, Takashi Taniguchi, Daniel Steil, D. Russell Luke, R. Thomas Weitz, Sabine Steil, G. S. Matthijs Jansen, Samuel Brem, Ermin Malic, Stephan Hofmann, Marcel Reutzel, and Stefan Mathias, "Formation of moiréinterlayer excitons in space and time," Nature **608**, 499–503 (2022).

[181] Jan Philipp Bange, David Schmitt, Wiebke Bennecke, Giuseppe Meneghini, AbdulAziz AlMutairi, Kenji Watanabe, Takashi Taniguchi, Daniel Steil, Sabine Steil, R. Thomas Weitz, G. S. Matthijs Jansen, Stephan Hofmann, Samuel Brem, Ermin Malic, Marcel Reutzel, and Stefan Mathias, "Probing electron-hole coulomb correlations in the exciton landscape of a twisted semiconductor heterostructure," Sci. Adv. **10**, eadi1323 (2024).

[182] Giuseppe Meneghini, Samuel Brem, and Ermin Malic, "Ultrafast phonon-driven charge transfer in van der waals heterostructures," Nat. Sci. **2**, e20220014 (2022).

[183] Jiangang He, Kerstin Hummer, and Cesare Franchini, "Stacking effects on the electronic and optical properties of bilayer transition metal dichalcogenides mos_2, $mose_2$, ws_2, and wse_2," Phys. Rev. B **89**, 075409 (2014).

[184] Soichi Shirai and Shinji Inagaki, "Ab initio study on the excited states of pyrene and its derivatives using multi-reference perturbation theory methods," RSC Advances **10**, 12988–12998 (2020).

[185] Masaaki Baba, Motohisa Saitoh, Yasuyuki Kowaka, Kunio Taguma, Kazuto Yoshida, Yosuke Semba, Shunji Kasahara, Takaya Yamanaka, Yasuhiro Ohshima, Yen-Chu Hsu, and Sheng Hsien Lin, "Vibrational and rotational structure and excited-state dynamics of pyrene," J. Chem. Phys. **131**, 224318 (2009).

[186] Kenneth B. Wiberg, Valeria A. Walters, Koon N. Wong, and Steven D. Colson, "Azines: vibrational force field and intensities for pyridine," J. Phys. C **88**, 6067–6075 (1984).

[187] F.S. Tautz, "Structure and bonding of large aromatic molecules on noble metal surfaces: The example of ptcda," Prog. Surf. Sci. **82**, 479–520 (2007).

[188] Holger Proehl, Thomas Dienel, Robert Nitsche, and Torsten Fritz, "Formation of solid-state excitons in ultrathin crystalline films of ptcda: From single molecules to molecular stacks," Phys. Rev. Lett. **93**, 097403 (2004).

[189] Heng-guo Wang, Shuang Yuan, Zhenjun Si, and Xin-bo Zhang, "Multi-ring aromatic carbonyl compounds enabling high capacity and stable performance of sodium-organic batteries," Energy Environ. Sci. **8**, 3160–3165 (2015).

[190] Koichi Momma and Fujio Izumi, "VESTA 3 for three-dimensional visualization of crystal, volumetric and morphology data," J. Appl. Cryst. **44**, 1272–1276 (2011).

[191] Qiang Fu, Dmitrii Nabok, and Claudia Draxl, "Energy-level alignment at the interface of graphene fluoride and boron nitride monolayers: an investigation by many-body perturbation theory," J. Phys. Chem. C **120**, 11671–11678 (2016).

[192] Sebastian Tillack, *Implementation and Application of Maximally Localized Wannier Functions within the (L)APW+lo Method*, Master's thesis, Humboldt-Universität zu Berlin (2018).

[193] Sebastian Tillack, Andris Gulans, and Claudia Draxl, "Maximally localized Wannier functions within the (L)APW+LO method," Phys. Rev. B **101**, 235102 (2020).

[194] Michael Rohlfing and Steven G Louie, "Electron-hole excitations and optical spectra from first principles," Phys. Rev. B **62**, 4927 (2000).

[195] Faluke Aikebaier, Anna Pertsova, and Carlo M. Canali, "Effects of short-range electron-electron interactions in doped graphene," Phys. Rev. B **92**, 155420 (2015).

[196] Sebastian Tillack and Claudia Draxl, "Automatic generation of maximally localized wannier functions via optimized projection functions and self-projections," (2025), arXiv:2502.03213 [cond-mat.mtrl-sci] .

[197] Nora Salas-Illanes, *Electronic structure of selected materials by means of the QSGW method within the LAPW+LO framework*, Ph.D. thesis, Humboldt-Universität zu Berlin (2019).

[198] Nora Salas-Illanes, Dmitrii Nabok, and Claudia Draxl, "Electronic structure of representative band-gap materials by all-electron quasiparticle self-consistent *gw* calculations," Phys. Rev. B **106**, 045143 (2022).

[199] Francesco Sottile, *Response functions of semiconductors and insulators: from the Bethe-Salpeter equation to time-dependent density functional theory*, Ph.D. thesis, Ecole Polytechnique (2003).

[200] Christian Vorwerk, *Theoretical Spectroscopy of* Ga_2O_3, Ph.D. thesis, Humboldt-Universität zu Berlin (2020)